Pablo Orus Calvet

Nanofabrication of metallic and superconducting tungsten-carbon nanostructures using focused ion beams.

Director/es

CÓRDOBA CASTILLO, ROSA
DE TERESA NOGUERAS, JOSÉ Mª

ISSN 2254-7606

Prensas de la Universidad
Universidad Zaragoza

Servicio de Publicaciones

ISSN 2254-7606

Universidad
Zaragoza
1542

Tesis Doctoral

NANOFABRICATION OF METALLIC AND SUPERCONDUCTING TUNGSTEN-CARBON NANOSTRUCTURES USING FOCUSED ION BEAMS.

Autor

Pablo Orus Calvet

Director/es

CÓRDOBA CASTILLO, ROSA
DE TERESA NOGUERAS, JOSÉ Mª

UNIVERSIDAD DE ZARAGOZA
Escuela de Doctorado

2021

Universidad Zaragoza

Doctoral Thesis

Nanofabrication of metallic and superconducting tungsten-carbon nanostructures using focused ion beams

---

Author:
Pablo Orús Calvet

Supervisors:
Dr. Rosa Córdoba Castillo
Prof. José María De Teresa Nogueras

Nanofabrication and Advanced Microscopies (NANOMIDAS) research group
Instituto de Nanociencia y Materiales de Aragón (CSIC-Universidad de Zaragoza)
Condensed Matter Physics Department

December 6, 2020

Facultad de Ciencias
Universidad Zaragoza

INMA
INSTITUTO DE NANOCIENCIA
Y MATERIALES DE ARAGÓN

LMA
LABORATORIO
DE MICROSCOPIAS
AVANZADAS

UNIVERSITY OF ZARAGOZA

Abstract

Nanofabrication of metallic and superconducting tungsten-carbon nanostructures using focused ion beams

by Pablo ORÚS CALVET

The usage of focused beams of ions (FIBs) to induce the deposition of different materials represents an incredibly powerful tool for the design and patterning of functional nanostructures. Specifically, by scanning a Ga^+ or He^+ FIB over the surface of a sample over which a gaseous precursor material has previously been delivered, decomposition reactions are induced on the precursor, which result in its partial deposition on the substrate, patterned following the path traced by the FIB. This technique is named focused ion beam induced deposition (FIBID).

Ga^+ FIBID of the $W(CO)_6$ precursor results in the growth of a material containing W and C, which is superconducting below 4.5 K. In combination with the patterning flexibility of FIBID, it thus represents a fascinating scenario for the investigation of several phenomena related to superconductivity.

Specifically, Ga^+ FIBID W-C nanowires are shown to sustain non-local long-range vortex transport: by injecting a current at one end of a nanowire subjected to an externally applied magnetic field, a Lorentz force is exerted on present vortices, which in turn push their neighbors and eventually reach the other end of the nanowire, yielding finite resistances in areas depleted of current. In addition, gate-voltage modulation of the critical current of Ga^+ FIBID nanowires, akin to a field-effect transistor geometry, is reported for this material for the first time.

The speed of FIBID can be drastically increased when the procedure is performed below the condensation temperature of the precursor material, which aggregates forming a thick layer available for the FIB to decompose. This approach, named Cryo-FIBID, is shown to yield a W-containing material with metallic behavior. The deposition growth rate is found to increase by up to three orders of magnitude, and the resulting deposits can be used as auxiliary contacts for electrical measurements.

Last, the patterning resolution of FIBID is significantly enhanced when using He^+ ions. Deposition of in-plane nanostructures using the $W(CO)_6$ precursor allows for patterning down to 10 nm in lateral size, with the deposits exhibiting type-II superconductivity below 2.5-4 K. The nanostructures are also found to sustain long-range non-local vortex motion.

Acknowledgements

During the last three years, I would have achieved little of what I present here had it not been for a great deal of people that have constantly supported me.

First, I would like to thank my two supervisors, Rosa and José María, for accepting me into the position, and for teaching and guiding me into working as a scientist, and for the complete support they have provided me during these years. Second, I would like to thank Isabel and Laura, from the Laboratory of Advanced Microscopies, whose expertise with the FIB/SEM instruments and willingness to teach and share it with me has been invaluable. These four people truly are the cornerstones of this thesis, and without them, it would not be a reality at all.

I also acknowledge Rubén, for backing me up with most cleanroom related procedures, ultrasonic wire bonding, and particularly for his involvement with the fabrication of gold-coated substrates; Teo and Mariano, for their help with the cryogenic deposition; Rodrigo and Alfonso, for their support with all TEM experiments; Ana, for her assistance with the low-temperature measurements in the low-temperature magneto-transport experiments; and Cristina, for her tremendously helpful support in bureaucratic and paperwork matters.

This work has been profoundly enriched through fruitful collaborations with inspiring scientists from other research lines and groups. I express my gratitude to Željko and Milorad for their warm welcome in the (then) snowbound Antwerp back in December 2017, and for their contributions to the numerical simulations of vortex motion; to Gregor, for his kind reception in the (also) snowbound Dresden in January 2019 and in the warmer August 2019, and for is expertise with the experiments concerning growth using He^+ focused ion beams; to Amelia and David, for their passionate and demanding efforts in their scanning tunneling microscopy experiments in our definitely-superconducting thin films; and to Lorenzo and Martino for kindly having me in a laboratory visit in Basel in October 2018. In addition, I would also like to explicitly thank Rafa and Leyre for sharing their artistic skills in the form of some figures and pictures that have been included in this thesis.

Somewhat less academic in nature and perhaps more personal, I wish to thank the following people, who have stood by my side in these three years. Bea, whom I met no later than five years ago and who was the first person to introduce me hands-on to nanoscience, for the kindness and selfless support she has provided to me during this whole half a decade; Alberto, for sharing with me the weight of indulging in the latest KS craze; Isma, for all the good-hearted yet somewhat heated arguments; Luis "C.", for all the jokes and great times shared during those early months, of which I have a truly fond memory; Luis, for the welcoming support provided in my brief internship in GPNT; Javi, for his constant stream of help with the instruments and his reassuring company; Mario, for her remarkable and encouraging efforts in making

the world more knowledgeable of some harsh realities that we are unfortunately unaware of; and last but not least, I wholeheartedly wish to thank Pilar, mostly for all the in-depth GoT and TWD discussions, but also for inspiringly standing like a beacon in the night for us all, promptly and genuinely ready to show us the way in whatever issue we may come up with at the time, either academic, scientific, bureaucratic, or grammatical in nature.

I would find it very hard to think of a better person to get stuck at an airport with after an exhausting conference week abroad other than Rubén, whom I wish to thank for all these years of shared highs and lows, with the former clearly outnumbering the latter. I also acknowledge Barri, truly a guy to look up to, for all the invaluable life insight and all the light and heavy talks I've had the joy of having with him; Alba, for all the LOLs and good times shared starting from her now-not-so-very recent arrival to the group and those to come; Leyre, for her warm-hearted company, her countless favors, and for helping me improve and become a healthier and happier person overall, including breaking my personal 5K mark; Adán, for all the good coffee breaks and miles run; Caro, for brightening and spicing our days up with her inspiring discourse; Rafa, for all the dark humor provided and the dark plastic injected; Simon, for the profound Spanish language discussions, the baking, and for being my running coach; Carlos, for all the shadows pursued and meaningful conversations had; David, for his professionalism and altruistic motivation in helping others, first-hand experienced by myself multiple times; and Bea and Cinzia, for all the laughs shared, and because *se non è vero, è ben trovato*.

I am also deeply grateful for having had the chance of traveling thousands of kilometers and in the most excellent company of Pedro and Amelia, whom I am lucky enough to grow close to since incidentally meeting them back in 2016. From a modest ice skating rink to the top of a sunset-lit NYC skyscraper, I am enormously happy for having shared all these countless memorable moments with you and I sincerely hope there are way more ahead in the years to come.

I also wish to thank Adrián y Andrea for all the shared climbing efforts, both up a boulder wall and down into the wyrd; Jorge, Marta, Javier, and Miguel, our very own and beloved fellowship; Pau, for his unconditional support, even if we don't get to see each other as much as we'd like; Sara, for her kind support and with whom I have shared a peculiar path, starting in a maths building and somehow ending up in a particle collider; Julia, for her inexhaustible good will and all the good times shared these years; Jorge, for all the stories weaved and for all of those that are to come; and Andrea, Pablo, Miguel, Javi, and Vanesa, with whom we are now nearing a ten-year friendship, for all the caféks and marañitas, and for the overall excellent quality time shared. Lastly, and most importantly, I wish to thank my parents and my brother, who have unconditionally supported me for as long as I have existed, and which, in the end, represent the driving force for everything that I do.

Contents

List of Figures

Chapter 1

Introduction

1.1 Nanoscience and nanotechnology

The prefix *nano-* (from Ancient Greek, *νάνος*, meaning "dwarf") is used in the International System of units to denote a factor of 10^{-9}. The most relevant unit for this work that uses this prefix is the *nanometer* (nm), which equals $10^{-9} = 0.000000001$ meters, or one millionth of a millimeter. The whole nine orders of magnitude that separate the nanoscale from the daily life scale are no trivial matter. While these numbers are somewhat difficult to gauge for the human mind, an intuitive example is that the difference in scale between a meter and a nanometer is roughly the same as that between the diameter of the Earth (around 12.7 million meters) and the size of a bee (a few centimeters). The effective size of an atom depends on the species and conditions, but is taken to fall within the 10^{-10} m range (10^{-10} m $= 1$ Å, Angstrom) - one nanometer can be thought of as only *ten* nicely stacked atoms (or even less when taking interatomic bonding distances into account).

Nanoscience and *nanotechnology* are umbrella terms that encompass the fields of study and application of fundamental and applied sciences that take place in the *nanoscale*, *i.e.*, those in which the system of study has at least one characteristic dimension of the order of nanometers, in most cases between 0.1 and 100 nm.

This field of study is particularly interesting for mainly two reasons. The first is that at the nanoscale, matter behaves in ways that are fundamentally different to those in the macroscale. While this aspect may come out as counter-intuitive to some, physical effects whose extent and/or magnitude depend on the scale are not something arcane - most people walk in a straight line without slightly correcting their heading to account for the Coriolis force that is pushing them to the side; nor anybody feels the gravitational pull exerted by a friend who is passing by. Yet these interactions do exist and take relevance in much larger systems, such as wind circulation in the atmosphere and planetary motions - their magnitude is simply not relevant at "smaller" scales (Figure 1.1a).

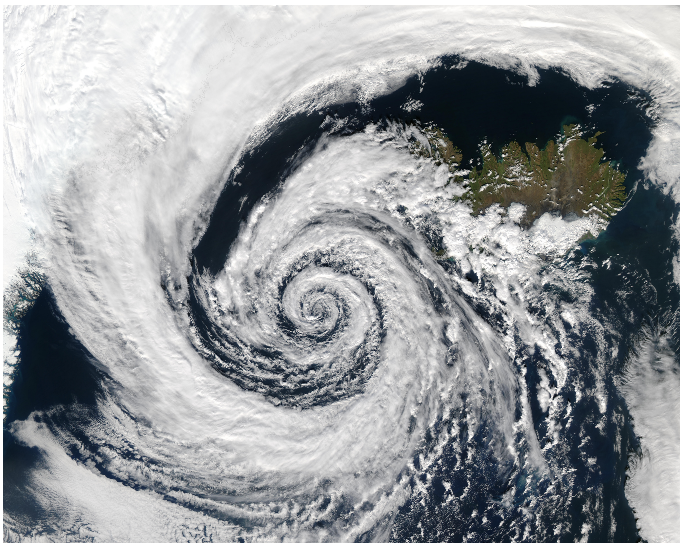

(A) A region of low atmospheric pressure over Iceland. As the pressure difference forces air masses towards the center of the region, they are deflected to the side due to the action of the Coriolis force, creating a swirling pattern. The magnitude of the same force acting over a person enjoying a stroll in the park is completely negligible.
Photography: NASA/GSFC, MODIS Rapid Response Team, Jacques Descloitres.

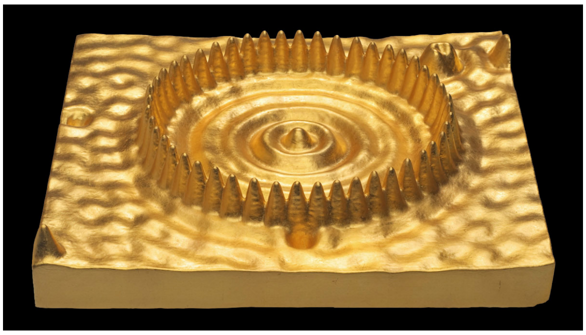

(B) *The Well*, a gilded wood sculpture representing an intriguing phenomenon known as a *quantum mirage*. Constructed from empirical data retrieved by scanning tunneling microscopy, the spots correspond to ferromagnetic Fe atoms over a Cu substrate [1] placed in a "quantum corral" disposition. The ferromagnetic atoms in the ring create an interference wave pattern on the electron distribution in the copper within, with a clearly visible maximum on the center, where no actual particle is located.
Photography: Julian Voss-Andreae, CC BY-SA 3.0.

FIGURE 1.1: Examples of scale-dependent phenomena.

Something similar happens in the nanoscale - physical mechanisms that are not relevant in a scale of meters take significance when considered in the nanometer range, and vice versa. As a toy example, one could not pour water out of a hypothetical nanometer-sized cup by turning it upside down, as surface forces would be much stronger than gravity in the nanoscale. *Quantum effects* take relevance and can be directly observed and measured in the nanoscale (Figure 1.1b).

The second reason for the present hype of nanoscience is practical in nature - it has not been until relatively recently that the nanoscale has become within reach. The newly developed microscopy and nanofabrication techniques that allow for imaging and handling at this scale were simply not available before the 20th Century.

These two reasons converge and make of nanoscience a field that is both *novel*, and *unexplored*. A myriad of possibilities opens up, with unbeaten paths leading to applications and theory in very different fields of study, including physics, chemistry, biology, geology, engineering, medicine, computing, and more. The term *nanoscience* is more commonly used to refer to basic research dedicated to investigate fundamental properties of matter, while *nanotechnology* is usually reserved to targeted applications of the former. In some contexts, they are used somewhat interchangeably, though.

As presented, nanotechnology is enormously vast, encompassing a large amount of scientific disciples and applications. The present thesis is centered on the study of a particular nanofabrication technique, to be presented in the following section; and on the investigation of a specific material that is fabricated using said technique. Namely, that material exhibits a fascinating physical property known as *superconductivity*, which shall be discussed in section 1.3. Superconducting materials, already quite interesting by themselves in the macro-scale, hold great potential when scaled down to nanometric dimensions, particularly in the field of electronics.

1.2 Nanofabrication with focused ion beams

An *ion* is an atom that, as a consequence of gaining or losing electrons, has a nonzero net electrical charge. Ionized matter, which is both naturally found and artificially extracted, is non-inert, reacting with other matter it interacts with due to its electrical charge. As such, ions are capable of altering the properties or state of matter, and can thus be exploited as interesting tools that can be exploited for different purposes, from medical procedures to particle detectors.

Ions can also be used to manufacture nanostructures in different ways. The one approach used in the context of the present work is that which handles them in the form of a *beam*, which can be thought of as a stream of accelerated ions. By making use of dedicated equipment, a beam of ions can be made converge into a single point, *e.g.*, it can be *focused*, with a finite size of a few nanometers or below, depending on the used species. This construct is given the self-descriptive name *Focused Ion Beam* (FIB), and represents an extremely powerful tool in the framework of nanotechnology (Figure 1.2) [2–10].

1.2.1 Historical development

The development of FIB technology is relatively recent, tracing back to no more than fifty years ago. As it will be discussed in section 2.1.1, one fundamental constituent of any FIB column is its *source*, *i.e.*, the component on which the ions are extracted

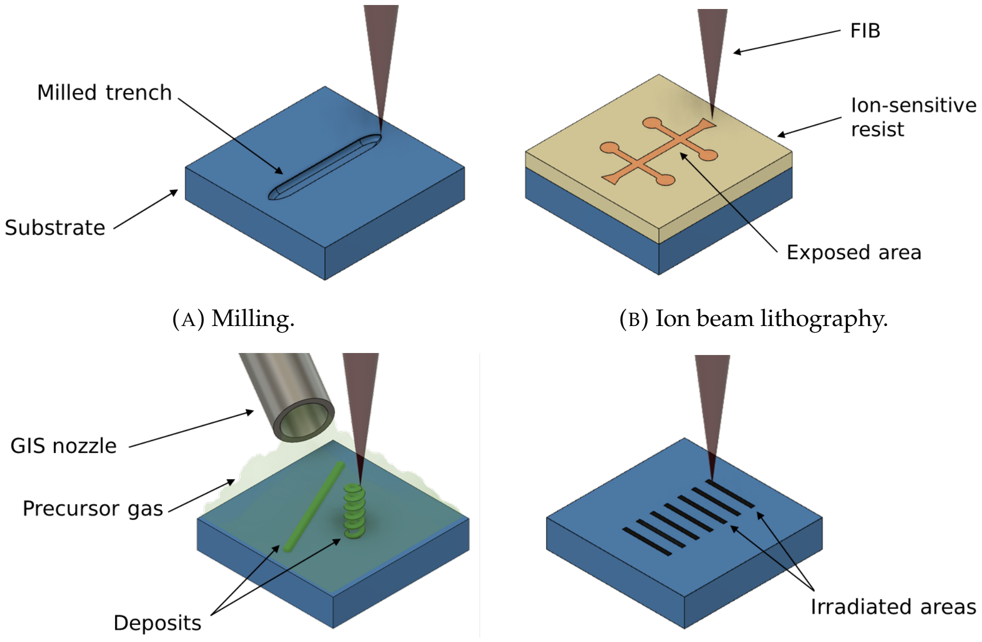

(A) Milling.

(B) Ion beam lithography.

(C) Focused Ion Beam Induced Deposition.

(D) Ion-induced material modification.

FIGURE 1.2: Examples of FIB processing applications.
Image credit: Rafael Marqués.

from a source material [4]. As such, the evolution of FIB technology is intrinsically tied to that of ion sources [8].

One of the first reported phenomena that are directly related to the physical principles on which some ion sources operate dates back to the 17th century and comes from magnetism pioneer William Gilbert, who reported that when an electrically charged piece of amber was placed near a water droplet, it would pull some near it, forming a cone. [11] This tendency of liquids to acquire a conical shape when subject to an electric field, which would later be named *Taylor cone* [12], is exploited in some ion sources to obtain an ion source effective size much smaller than the physical device on which the liquid is placed.

Important steps in ion source development were carried out in the 1970s, with Seliger and Orloff being two of the most prominent names on the matter - the first reported in 1974 the usage of a 3.5 μm-wide He^+ beam for material modification [13] (enormous, by today's standards of a "focused" beam); while in 1975 and 1978 Orloff reported the controlled ionization of H_2 [14] and Ar [15] to generate more focused beams (0.1 μm in size).

Ion sources based on the ionization of a liquid source material were first developed in the 1970s. Initially destined to be used for thrust in space applications [16], the technology rapidly evolved to become what are nowadays known as *Liquid Metal Ion Sources* (LMISs) [8]. In 1979, Seliger *et. al* reported the usage of an improved 57 kV Ga$^+$ source to mill trenches on an Au film [17], representing the first usage of a such a beam for the purposes of nanopatterning.

The investigation to obtain ion beams from source materials in gaseous form was being carried out in parallel. A significant milestone was the development of a somewhat rudimentary (for today's standards) instrument named *Field Ion Microscope* in 1955 by Müller *et al.* [18] - a glass-blown recipient filled with gaseous He and containing a fine tungsten tip and a fluorescent screen. By counter-biasing the tip to the screen, the gas was ionized at the tip and accelerated towards the screen, where the emission pattern of the needle would be imprinted. This experiment represents the first time in the history of humankind that a proper "image" of individual atoms (those constituting the apex of the tip) was recorded. Competing with the sturdy and commercially widespread LMISs, sources based on field-ionization of a gas were developed in the 1990s and 2000s, culminating in the atomic-trimer based *Gas Field Ion Source* (GFIS), presented by Ward *et al.* in 2006 [19].

At the present day, both types of sources can be found in commercial equipment. LMISs are more common than GFISs since they are, in general, more affordable and easy to deal with than GFISs, as well as more suited for general purpose. In conventional optimal conditions, the probe size roughly equals 5 nm for Ga$^+$ FIBs, and 0.3 nm for He$^+$ FIBs [20, 21]. FIB processing has become a fundamental pillar in the field of nanomanufacturing, either used as a nanofabrication technique by itself (as in the case of this thesis), as a supplementary tool (very commonly, in the preparation of samples for transmission electron microscopy), or imaging purposes [4, 8, 22].

1.2.2 Principles of focused ion beam processing

Two basic principles govern the core of FIB processing mechanisms: *(a)* ions can be extracted from a source and then accelerated down a column, so they gain a significant amount of energy, and *(b)* this energetic beam of particles can be delivered at a very small area, *i.e.*, at the point where the beam is focused on. By precisely steering the beam over a sample, the energy transfer can be exploited for different purposes, which all depend on how the energy of the ions is transferred to the sample and on the responses it induces (Figure 1.3). In this section, the more common mechanisms that take place in FIB processing are reviewed.

The two types of interactions that are relevant for the purposes of FIB processing correspond to a conservative energy transfer from the ions to the sample, either *nuclear* or *electronic* in nature. Nuclear interactions arise from the elastic collisions between the incident ions and the atoms in the sample; while electronic energy transfer takes place as a consequence of the electromagnetic interaction between the positively-charged incoming ions, and the electrons of the atoms in the sample [4].

The physical extent up to which these reactions are relevant within the sample depends on the material it is made of, on the energy of the beam, and on the ionic

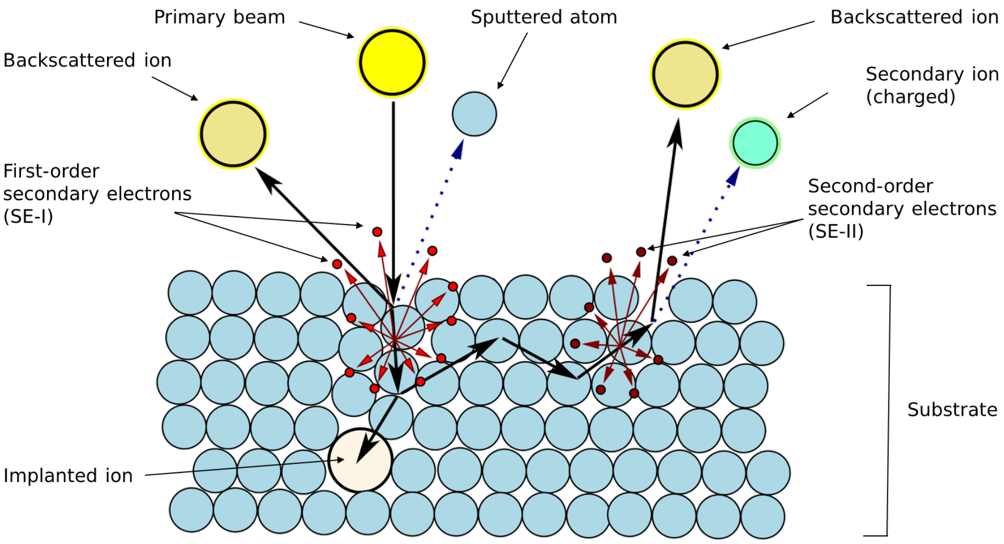

FIGURE 1.3: Ion-solid interactions.

species used. Parametrized as the average distance that an ion can travel before losing all of its energy, this length is referred to as *ion range*, and it is used to define a tear-shaped volume from the impinging point known as *interaction volume* (Figure 1.4), of paramount importance in FIB processing. Adjusting the experiment conditions to obtain an adequate interaction volume is key to achieve successful FIB processing. For example, the apex of the interaction volume is way sharper when using He^+ ions than when using Ga^+ ions due to the lighter mass of the former, which results in enhanced lateral patterning resolution.

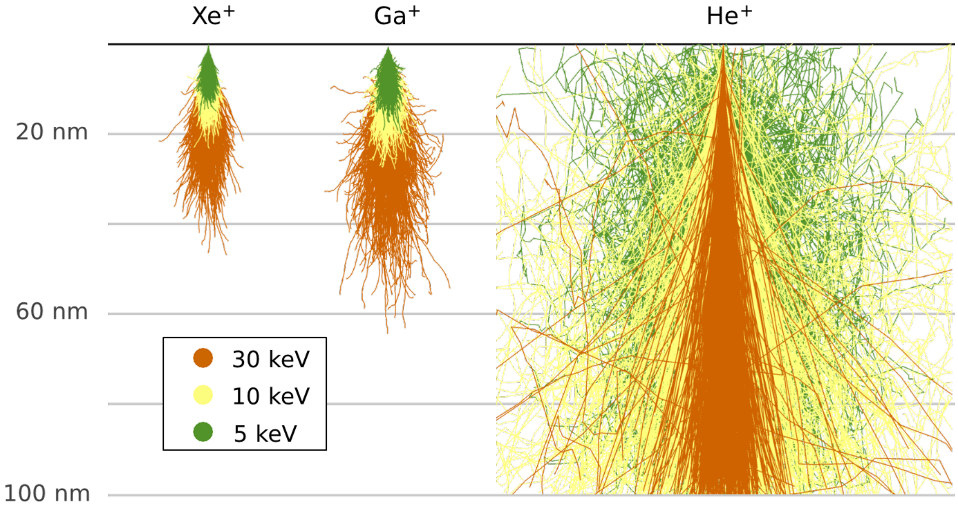

FIGURE 1.4: Ion trajectories in a Si substrate using three different energies and three typically-used ion species. The numerical simulation software SRIM [23] has been used to obtain these figures.

Nuclear interactions induce ion energy loss via elastic collisions of the impinging particle with the atoms of the sample. The initial collision forces an atom out of its equilibrium position, which itself induces a secondary displacement on a neighboring one. The perturbation that propagates deep in the bulk of the sample is typically modelled as a series of successive binary collisions, named *collision cascade*. These displacements result in amorphization of the sample material, an effect that must always be taken into account when dealing with FIB processing.

Collision cascades result in the net emission of different particles from the substrate. When momentum is transferred back to the surface of the sample, if the energy provided overcomes the binding energy of the surface atom, it gets ejected away from the substrate. This effect, named *sputtering*, can be exploited as one of the patterning capabilities of a FIB, for it can be used to precisely mill trenches, holes, and other features on samples. It can also prove a drawback in some situations, since irradiating fragile samples with a FIB will damage and sputter some material away, depending on the experiment conditions. Sputtered atoms are neutral and can either be redeposited near the area of emission, or pumped away by the vacuum system of the instrument. In some cases, the ejected particles undergo ionization as they are ejected, gaining net electrical charge - they are referred to as *secondary ions* (SIs), to distinguish them from the primary radiation coming from the beam. SIs are used as a compositional fingerprint in a FIB-based spectroscopy technique named *Secondary Ion Mass Spectrometry*, or SIMS [24].

The incoming ions themselves can either be ejected back from the sample after one or multiple collisions before losing all of their energy, in a process known as *backscattering*; or remain in the bulk of the sample after losing all of their energy therein. This mechanism, known as *ion implantation*, of particular relevance in Ga^+ FIB processing, results in permanent modification of the composition of the sample, which will include traces of Ga after ion exposure; and similarly to material amorphization, must be taken into account when considering the process.

If the energy of the incoming ions exceeds the ionization potential of the atoms in the sample, electronic excitations are induced on the sample, which result on the emission of different particles. *Secondary electrons* (SEs) are electrons emitted as products of the ionization of the sample atoms induced by the FIB. Depending on the region where they appear, SEs are referred to as of *first order* (generated at the area of irradiation with the beam), and of *second order* (generated away from the FIB, as scattered ions induce new excitations in a different region).

SEs are the leading actors of the play in scanning electron microscopy (SEM) and in deposition induced by a FIB, for they carry information on the topography of the surface near which they were emitted, and are capable of inducing decomposition reactions on precursor molecules adsorbed on the surface of the sample (more on that later, in section 2.1.2).

In FIB processing mechanisms, these interactions are utilized for good or ill in different contexts (Figure 1.2). The present thesis deals with the utilization of a FIB to induce growth of nanostructures from a precursor material, which will be the focus of section 2.1 in the following chapter.

1.3 Superconductivity

Along with deposition using FIBs, the second point of interest in this thesis is the study of a fascinating physical effect known as *superconductivity*. A formal description of this phenomenon is outside the scope of the present work and can be found elsewhere [25]. Instead, a summary of the main phenomenological aspects of superconductivity relevant to the present work is provided here.

1.3.1 Basic phenomenology

Superconductivity is an electronic state of matter characteristic of some materials, mostly metallic in nature, which has as its most prominent feature a complete absence of electrical resistance below a certain temperature. It was discovered in 1911 by Dutch physicist Kamerlingh Onnes, whom, after developing a procedure to liquefy helium, probed several electrical characteristics of metals at low temperature. Onnes detected that below 4.2 K, the resistance of a piece of solid mercury dropped down to zero [26].

The most characteristic parameter of a superconducting material is its *critical temperature*, T_c, which corresponds to the temperature below which the resistance of the material drops to zero. Values of T_c in superconducting materials are in the range of what is intuitively defined as "low" - the discovery of the phenomenon was, in fact, bound to the development of the previously-unavailable helium liquefaction, which would thereafter be used as a cooling agent. The fact that superconducting behavior falls in the low temperature range severely hampers the otherwise extremely attractive potential of superconducting materials. However, during the last century strong efforts have been directed towards the search for new materials with continuously increasing values of T_c, up to the point to which as of the present day, a whole range of the so-called *high-temperature superconductors* exists, with some materials exhibiting T_c above 100 K [27], and others reaching the superconducting state even at room temperature (although only at very high pressures) [28].

Temperature is not the only parameter that bounds the superconducting state. Superconductivity is best thought of as a volume in a three-dimensional phase diagram of temperature T, externally applied magnetic field B, and driving current density J (Figure 1.5). Analogously to the temperature, each of these two other parameters also has a characteristic critical value for each material, B_c and J_c - increasing them above their critical value drives the material to the non-superconducting state, henceforth referred to as the *normal* state. Normally, T_c is given at $B = 0$ and $J = 0$,

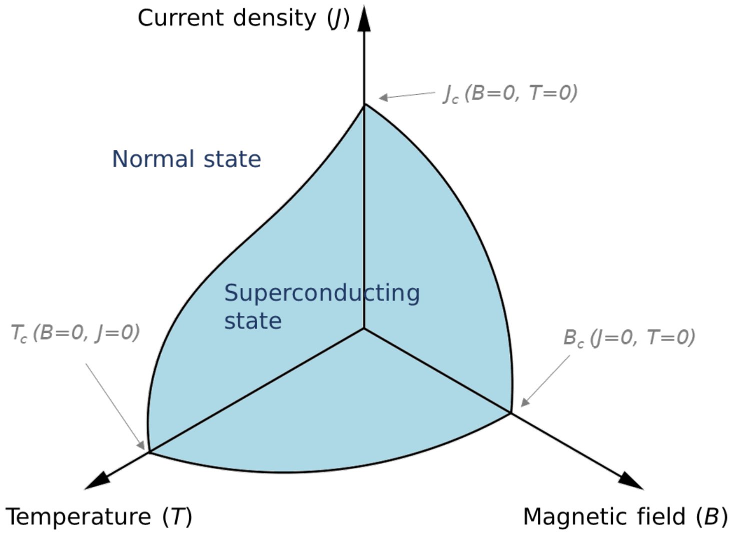

FIGURE 1.5: Phase diagram of superconductivity.

while B_c and J_c are typically presented as a function of T. The higher the experiment temperature (*i.e.*, the "closer" the material is to the transition to the normal state), the lower the values of B_c and J_c.

In this work, to experimentally determine the values of the critical parameters, the following convention will be used: T_c is defined as the value of T at which the resistance of the material, R, reaches half the value it had in the normal state, R_N: $R(T = T_c) = 0.5R_N$. The material under study is always in the normal state at 10 K, which is used as a reference value for R_N: $R(T = 10K) = R_N$. In addition, in some cases the width of the transition is also given in the form $T_C + \Delta T$, with ΔT being half the amplitude of the transition, measured from T_c. On the other hand, B_c and J_c are defined as the value taken by the parameter when the resistance of the material reaches 90% of its normal value: $B_c(T) \equiv B(T, R = 0.9R_N)$, and $J_c(T) \equiv J(T, R = 0.9R_N)$.

The perfect conductivity characteristic to the superconducting state also comes with a caveat - *perfect diamagnetism*. In a general sense, a magnetic field externally applied to a diamagnetic material induces screening currents on it that generate a second magnetic field with opposite direction to the inducing one, effectively expelling the magnetic flux lines from within the material. Conventional diamagnetic materials are capable to sustain this state up to a certain value of magnetic field, but with perfect conductivity, the screening (super)currents are virtually unbound within the superconducting state, and as a consequence, magnetic flux lines do not penetrate in superconducting materials. This phenomenon is known as *Meissner effect* [29].

One early phenomenological theory used to describe the Meissner effect was that of the London brothers, or *London theory*, presented in 1935 [30]. It is inferred from the equations of this model that the magnetic flux is not fully expelled on the superficial layers where the supercurrents flow, where it presents an exponential decay from the surface towards the bulk with a characteristic decay length named *London penetration length*, λ_L.

1.3.2 The BCS theory

An explanation of superconductivity from a microscopic point of view is provided by the *BCS theory*, which gets its name from Bardeen, Cooper, and Schriefer, who published it in 1957 [31]. A very brief comment on its basics is presented here.

The BCS theory accounts for the phenomenon of superconductivity by defining a new type of charge carrier in the superconducting state: *Cooper pairs*. A Cooper pair is a bosonic entity constituted by two correlated electrons with opposite momenta and spin. In a metallic-like structure, the conduction electrons interact with the positively-charged ion cores in the crystal, with their displacements from their equilibrium positions corresponding to the characteristic lattice vibrations (referred to as *phonons*). Broadly speaking, the electron-phonon interaction results in an effective attraction between the two electrons, which then qualify to constitute a Cooper pair. The density of superconducting charge carriers, n_s, is typically used as a quantifying parameter to determine the state of the material, being superconducting for $n_s = 1$, and normal for $n_s = 0$.

The relatively weak binding energy of a Cooper pair only makes its existence stable below the critical temperature of the material. One of the "signature" parameters of superconductivity from both a theoretical and experimental point of view is the existence of the *superconducting gap*, Δ. In terms of T_c, the BCS theory predicts for its value to follow

$$\Delta = 1.76 k_B T_c, \tag{1.1}$$

where k_B is the Boltzmann constant. The dimensionless numerical prefactor is in agreement with experimental results [25].

The value of the superconducting gap is an indicative of the energy that corresponds to the binding of a Cooper pair. It represents a state-devoid region in the density of states of a superconducting material, appearing as a consequence of all electrons in the material condensing into Cooper pairs instead of appearing as individual electrons with energies below Δ. This gap can be experimentally probed by tunneling microscopy, as described in 2.4.1.

For the superconducting state to exhibit the electronic scattering mechanisms that result in the conventional energy-losses in electronic transport at room temperature, Cooper pairs would need to be broken, which is energetically unfavorable. As such, the material exhibits perfect conductivity below T_c. The superconducting gap lessens with increasing temperature, completely vanishing when the material is in the normal state.

1.3.3 The Ginzburg-Landau theory

The most extended and accepted theory that accounts for the majority of the phenomenology in the macroscopic scale is the *Ginzburg-Landau theory*, developed by the titular physicists in 1950 [32]. In this theory, the superconducting state is described by a spatial-dependent wavefunction, or *order parameter*, ψ,

$$\psi(\boldsymbol{r}) = |\psi(\boldsymbol{r})|e^{i\varphi}, \tag{1.2}$$

where $\boldsymbol{r}$ is the position within the material,and φ is a *superconducting phase*. Its module is defined so that $|\psi(\boldsymbol{r})|^2 = n_s$. The order parameter vanishes when the material is not superconducting ($n_s = 0$), and maintains the same phase φ within the whole superconducting bulk.

Two equations crown this theory, rightfully named the *Ginzburg-Landau* equations. They are obtained by defining a free energy as a function of ψ and of an externally applied magnetic field, and then minimizing it with respect to small variations of both ψ and said field. The formal deduction of these equations can be found elsewhere [25]. For the purposes of the present thesis, it will suffice to say that each of these equations presents with the spatial distribution of ψ and B within the bulk of the superconductor, hinting towards equilibrium states other than the Meissner effect previously discussed.

Specifically, in the variational analysis performed for each of the equations, a characteristic length arises, which describes the decay length of the corresponding parameter (ψ or B) towards energetically unfavorable regions of the material.

Namely, the Ginzburg-Landau length associated to ψ is named *coherence length*, ξ, and describes the scale on which ψ (and thus, n_s) decays away from its equilibrium value. The length that relates to the magnetic field gets the name of *penetration depth*, λ, and accounts for the decay length of a magnetic field penetrating in a superconductor[1] (Figure 1.6). Near T_c, both lengths depend on the temperature in the form

$$\lambda, \xi \propto \frac{1}{\sqrt{T_c - T}}. \tag{1.3}$$

Their (temperature-independent) ratio is paramount in determining the superconducting behavior of the material, so much it even gets its own symbol, κ, and name: the *Ginzburg-Landau parameter*, $\kappa = \lambda/\xi$.

---

[1] It is worth noting that, while significantly related, the London and Ginzburg-Landau penetration depth are different parameters. Namely, at zero temperature, $\lambda_L \sim 1.41\lambda$.

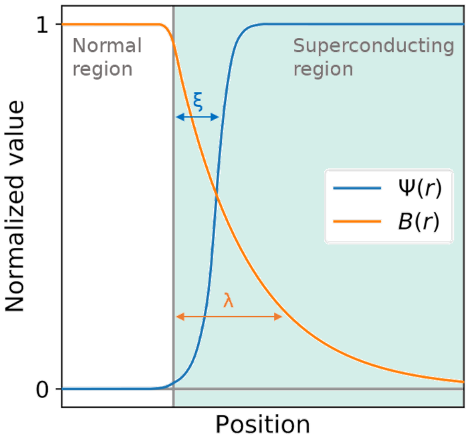

FIGURE 1.6: Change in the order parameter and magnetic field in a normal-superconductor interface, with the associated characteristic decay lengths.

1.3.4 Type-II superconductors

Superconducting materials that strictly follow the description presented in the previous sections, *i.e.*, that exhibit only two possible states (superconducting with Meissner effect, and normal) are named *Type-I superconductors*. This name foreshadows the existence of a different kind of superconducting materials, those named *Type-II superconductors*. The main feature of these materials is that a third phase exists between the Meissner and normal states: the *mixed state*, whose existence was experimentally reported (in the form of anomalies in magnetization studies) for the first time in 1935 by Rjabinin and Shubnikov[2] [33].

Russian physicist A. Abrikosov showed in 1957 that, for superconducting materials with $\kappa > 1/\sqrt{2}$, a periodical solution of the Ginzburg-Landau equations which minimized the energy of the mixed state existed, in the form of a regular, (in most cases) triangular array of flux lines distributed throughout the material[3] [34, 35].

Due to its fundamental relation with the magnetic field, the mixed state is usually visualized in the projection of the phase diagram on the B-T plane (Figure 1.7a). Bound by two critical magnetic fields, named *lower* and *upper* ($B_{c1}(T)$ and $B_{c2}(T)$ respectively), this superconducting phase is characterized by the persistence of the dissipationless regime combined with penetration of magnetic flux.

A magnetic field externally applied to a type-II superconductor is expelled from its bulk if its value is below B_{c1}, and drives the material to the normal state if it is above B_{c2}. If the value of the field at the experiment temperature falls between B_{c1} and

---

[2] Some texts refer to the mixed state as the *Shubnikov phase*.

[3] One of the reasons for the relevance of κ is that its value is assessed to determine the nature of the superconducting material under study: materials with $\kappa > 1/\sqrt{2}$ behave as type-II superconductors, while those with $0 < \kappa < 1/\sqrt{2}$ are classified as type-I.

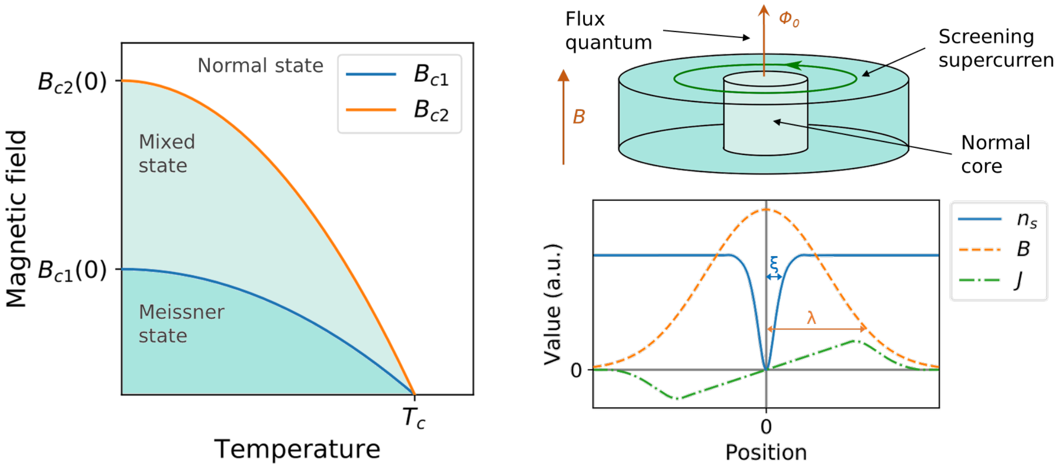

(A) $B - T$-projected phase diagram.

(B) A superconducting vortex.

FIGURE 1.7: Features of type-II superconductors.

B_{c2}, then the flux lines do penetrate the bulk of the material, but, contrary to what happens in the normal state, they do so in a quantized, ordered form.

Magnetic field flux lines penetrate type-II superconducting materials through physical entities named *superconducting vortices* (Figure 1.7b). Considering a film-like superconducting structure of finite thickness and a perpendicularly applied magnetic field, a superconducting vortex[4] is a locally normal tubular region, screened by a circular supercurrent, and threaded by a line of magnetic flux.

The amount of magnetic flux Φ that threads a vortex depends on universal physical constants only, and gets the name of *flux quantum*:

$$\Phi = \frac{h}{2e} = 2.07 \cdot 10^{-15}\,\mathrm{Wb}, \tag{1.4}$$

h being Planck's constant, and e being the electron charge. Therefore, a fundamental property of vortices is that every single one of them encloses the same amount of magnetic flux, independently of the temperature, the field, the material, or any other variables.

The associated energy per unit length of each superconducting vortex is given by

$$\varepsilon_L = \frac{\Phi_0^2}{4\pi\mu_0\lambda^2}\log\left(\frac{\lambda}{\xi}\right), \tag{1.5}$$

where μ_0 is the magnetic permeability of free space.

---

[4] For simplicity, these will occasionally be referred to as simply *vortices* hereafter.

When a type-II superconducting material is exposed to a magnetic field within the boundaries of the mixed state, the magnetic flux is redistributed in individual vortices that thread the material, and that arrange constituting a (usually) triangular array referred to as *Abrikosov lattice* (Figure 1.8). In good agreement with Abrikosov's predictions, the vortex lattice was experimentally imaged in the late 1960s [36–38].

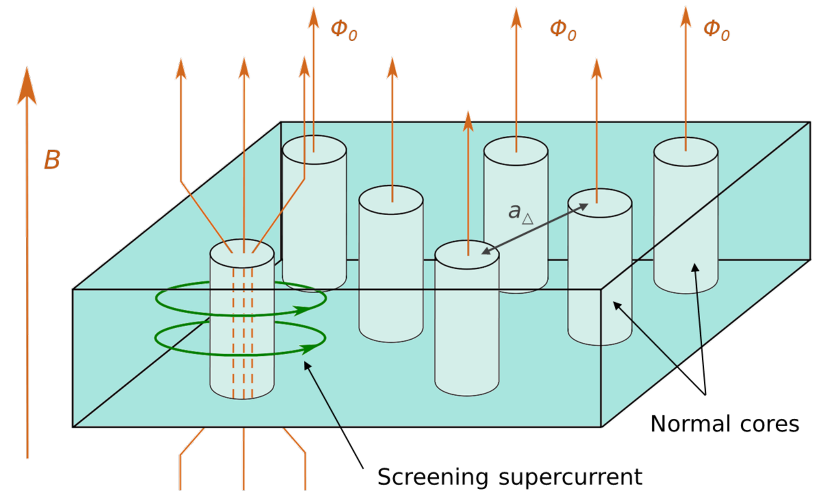

FIGURE 1.8: The Abrikosov lattice.

The higher the field, the higher the vortex density and the more closely packed the lattice will be. The inter-vortex separation depends on the magnetic field only, as per

$$a_\triangle = \left(\frac{4}{3}\right)^{1/4} \sqrt{\frac{\Phi_0}{B}}. \tag{1.6}$$

In the present work, the values of the Ginzburg-Landau lengths in a type-II superconducting material have been estimated using empirical equations that make use of experimentally accessible parameters, rather than from the formal definitions of the Ginzburg-Landau theory. In particular, the coherence length is calculated from

$$\xi^2 = \frac{\Phi}{2\pi B_{c2}}, \tag{1.7}$$

and the penetration depth is estimated from

$$\lambda = 1.05 \cdot 10^{-3} \sqrt{\frac{\rho_{300K}}{T_C}}, \tag{1.8}$$

where the prefactor is expressed in SI units, and ρ_{300K} indicates the resistivity of the material at 300 K [25, 39].

1.3.5 Dynamics of superconducting vortices

For a significant fraction of applied superconductivity engineering, the presence of superconducting vortices represents a minor nuisance at best, and a major inconvenience at worst. Injecting a driving current into a superconducting material in the mixed state (under an applied magnetic field) results in the charge carriers of the current interacting with the circular supercurrents that surround the vortices in the form of electrostatic repulsion. As a consequence, vortices are pushed, and as their normal cores drift along the material, energy is dissipated below T_c, which manifests itself in the form of a nonzero resistance [25, 40].

Such a resistance is accounted for by the voltage associated to the motion of the vortices, which is obtained from Faraday's law,

$$\boldsymbol{E} = -\nabla V = \boldsymbol{B} \times \boldsymbol{v_\Phi}, \tag{1.9}$$

where $\boldsymbol{v_\Phi}$ indicates the velocity of a moving vortex.

Although the extent of this dissipation does not reach the level of that in the normal state, it undoubtedly taints the otherwise pure, perfect conductivity characteristic of the Meissner state. As such, significant effort has been made towards immobilization of vortices in type-II superconducting materials, to enable their utilization as conducting devices under applied magnetic fields without energy losses.

However, the fundamental property of flux quantization that vortices exhibit also makes them attractive for their own purposes. A plausible hypothesis is that due to this very property, vortices could be potentially used as quantized information carriers. Provided their motion was controlled and targeted, a single vortex could be utilized as a single unit of information. A series of vortices precisely delivered to a proper "reading" end could therefore transmit a message of some sort from one physical point of a device to the other. The fundamental aspects of this approach of information transfer are experimentally explored in sections 3.3 and 5.3.

A simple model of vortex dynamics within a superconducting channel defines the effect of the injected driving current in terms of a *Lorentz force* $\boldsymbol{F_L}$, so that the force acting upon one individual vortex is

$$\boldsymbol{F_L} = \boldsymbol{J} \times \boldsymbol{\Phi}, \tag{1.10}$$

where the direction of the quantum flux $\boldsymbol{\Phi}$ matches that of the externally applied field, $\boldsymbol{B}$. Therefore, a vortex under the influence of an injected driving current will tend to move in a direction that is perpendicular to both the direction of the current itself, and the direction of the field.

In the present thesis, only in-plane nanostructures are studied, and the geometry is kept rather simple - the magnetic field is always applied perpendicularly to the substrate, and the driving current is always applied in a direction within the plane of the substrate. Therefore, the direction of the Lorentz force is always expected to fall within the plane of the substrate, and to be perpendicular to the direction of the driving current (Figure 1.9).

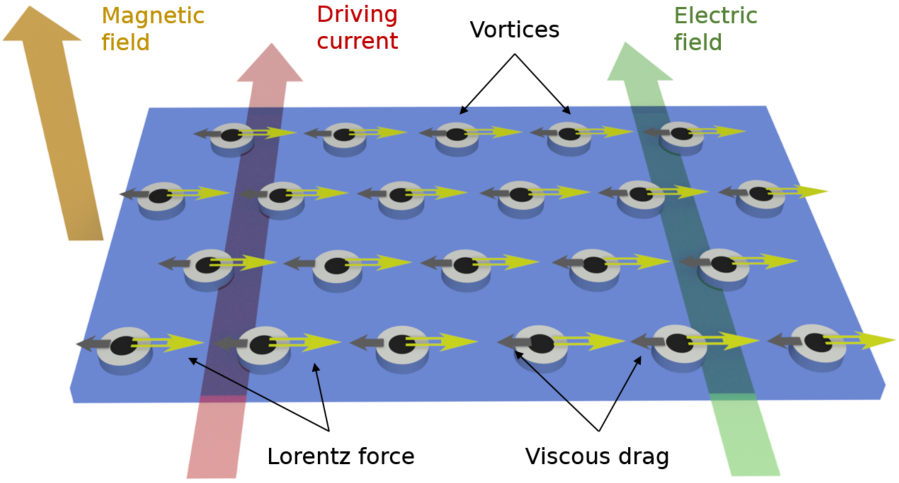

FIGURE 1.9: Forces acting on vortices in a superconducting film under an externally applied magnetic field.

The equation of motion of vortices in a superconducting channel reads

$$\boldsymbol{F_L} - \eta \boldsymbol{v_\Phi} - \boldsymbol{F_P} = 0, \tag{1.11}$$

where $\eta \boldsymbol{v_\Phi}$ accounts for a viscous drag for vortex motion, and $\boldsymbol{F_p}$ is an effective force associated to pinning, both of which are directed in the opposite direction of $\boldsymbol{v_\Phi}$[5] [25, 40–42].The effect of vortex pinning in a superconducting material is typically visualized in terms of a potential landscape that defines energy minima for the vortices - the *pinning sites*. In absence of driving currents, vortices tend to occupy these local energy minima, which can be further enhanced by defects in the material[6]. Potential barriers are always present at the edges of the nanostructure, "repelling" vortices that are directed towards them and significantly hampering vortex entrance and exit in the nanostructure.

After the magnetic field is applied to the superconducting structure, vortices form the lattice by appearing on the lower-energy pinning sites first, and occupying the

---

[5] Some texts also include a third term, the *Magnus force*, pointing in a direction parallel to the driving current, which would make vortices move at an angle with respect to $\boldsymbol{F_L}$. However, in most cases the extent of this force is so small that it can be safely neglected.

[6] A "perfect" Abrikosov lattice extending along large distances in a material is rather unusual. A more frequent finding is that of small sublattices arranged in domains that adapt to topographic features in the material.

rest as the magnetic field is increased and the total number of vortices rises. Vortices are also able to randomly "jump" from one pinning site to a neighboring one. A sufficiently high value of the applied magnetic field results in saturation of the pinning sites, which are no longer capable of confining vortices therein; and leads to loss of lattice rigidity and lattice melting.

When an external current is injected into the superconducting material, the otherwise isotropic potential landscape gets "tilted", gaining a favored direction indicated by the Lorentz force (equation 1.10). As such, vortex motion from one pinning site to another is no longer neutral, and a direction of motion is established. In the equation of motion (equation 1.11), the effect of $\boldsymbol{F_P}$ is akin to static friction. Effectively, as $\boldsymbol{F_L}$ increases in magnitude, so does $\boldsymbol{F_P}$, up to a critical value of $\boldsymbol{F_L}$, where no longer restrains the vortices and the onset of motion occurs. After that point, vortex motion is mostly regulated by the combined action of the Lorentz force and viscous drag only. The magnitude of $\boldsymbol{F_P}$, dependent on the material, determines the maximum field the material can withstand without dissipation.

Vortex transport in superconducting nanostructures has been extensively studied, starting with the "flux transformer" device proposed by Giaver *et al.*, where resistances associated to vortex motion between to electrically insulated superconducting films were detected [43]. One of the most relevant reports for the present context is that of Grigorieva *et al.* [44], on which a particular nanostructure geometry designed to read resistances associated to vortex motion in areas depleted of current was proposed. This general approach is referred to as *non-local vortex transport*, since vortex motion (and the subsequent voltage generation) are induced *non-locally*, *i.e.*, in areas located away from the driving current.

The device is patterned in the form of a superconducting channel through which superconducting vortices are intended to move; and two perpendicular leads placed near the ends of the channel (Figure 1.10). The driving current is injected through one of these transverse leads, perpendicularly to the longitudinal axis of the main channel of the nanostructure, and voltage is measured at the other. Provided that the two leads are sufficiently separated, virtually no current is expected to flow through the second lead, and any finite voltages read in the measurement cannot be accounted for by conventional electrical resistivity. Indeed, in the normal state and in the superconducting phase without any applied magnetic field, the value of the non-local resistance is zero.

However, below T_c, within $B_{c1} < B < B_{c2}$ and for a certain range of values of J, finite resistances are detected in the voltage leads, which are accounted for by vortex motion only. These non-local resistances are revised in a model proposed by Helzel *et al.* [45]. A nanowire patterned for non-local vortex geometry is considered, with length L, channel w, thickness z, and transverse lead width b (Figure 1.10).

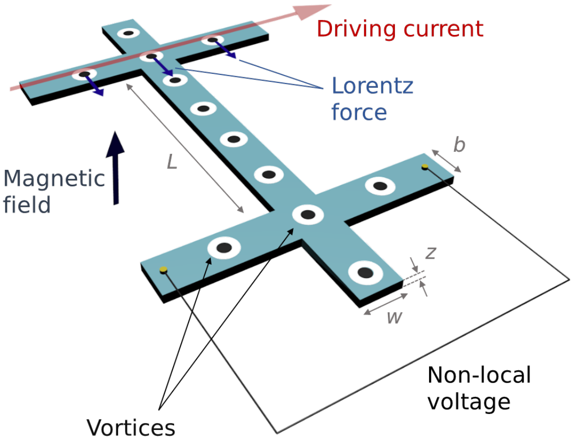

FIGURE 1.10: Non-local voltage measurement in a type-II superconducting nanowire.

At the crossing point between the channel and the leads, and for a given value of magnetic field, a total of N_b vortices exists: $N_b = n_\Phi w \cdot b$, with n_Φ being the vortex density at that field, $n_\Phi = B/\Phi_0$. Each vortex is affected by the Lorentz force exerted by the driving current density, which in one dimension is expressed as $F_L = J\Phi = I\Phi/bz$, since $J = I/bz$ (in the current lead).

Setting $\boldsymbol{F_P} = 0$, equation 1.11 is then rewritten for vortices in the current lead in one dimension as

$$N_b F_L = N_L \eta v_\Phi \longrightarrow I\Phi/z = L\eta v_\Phi \longrightarrow v_\Phi = \frac{I\Phi}{\eta L z} \ , \tag{1.12}$$

retrieving an explicit expression for v_Φ (N_L is the vortex density on the channel). Defining from Faraday's law (equation 1.9), $V_{nl} = wBv_\Phi$, then

$$V(B,I) = \frac{w\Phi_0}{\eta L z} BI. \tag{1.13}$$

Therefore, within the range of validity of this model, a linear dependence of the voltage with the field and current is expected. Experimental work and further discussion on the matter can be found in section 3.3.

1.3.6 Field effect or gating effect

The *field effect*, or *gating effect*, is a physical phenomenon that, at a basic level, consists on the modulation of the charge carrier density in a channel through an externally applied electric field. The voltage associated to this field is named *gate* voltage, for it regulates the amount of charge carriers that circulate through the channel (*i.e.*, the resistance). The gating effect is of particular relevance when dealing with semiconductor materials[7], representing the core of *field-effect transistors* (FETs).

Field effect in metallic materials is, in principle, non-existent. Due to the large amount of free charge carriers, any applied electric field is promptly screened within the bulk of the material. However, recently reported calculations indicate that in thin films of metallic superconductors, an externally applied electric field does extend within the material for at least the value of ξ [48].

Superconducting films are indeed sensitive to externally applied electric fields - a sufficiently strong electric field does alter the charge carrier concentration in the superconductor, which does in turn result in modifications of the normal state resistance, of T_c, and of I_c [49]. Making use of gating electrodes placed in close proximity to a superconducting nanostructure it is therefore possible to modulate the critical parameters in the superconducting state. The effect is related to the intense electric fields breaking Cooper pairs as they induce a new lowest-energy state corresponding to unpaired electrons, but notably enough, at the time of writing there is no complete explanation that accounts for this phenomenon at the microscopic level [50]. These predictions pave the way towards the development of transistor-like devices based on superconducting materials.

At a basic level, such a "device" consists of a superconducting channel placed near two gate electrodes. A driving current is made flow through the channel, and applying a potential difference between the two electrodes generates a strong electric field over the channel (Figure 1.11).

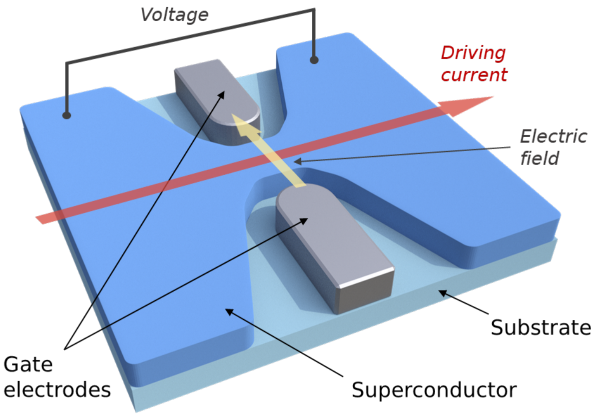

FIGURE 1.11: Basic geometry of a S-FET device.

The main effect of this electric field on the superconducting material is a decrease of the magnitude of the superconducting parameters as the gate voltage increases.

---

[7] Field effects have also been explored in other materials, such as correlated oxide systems [46], where its exploitation serves as the basic building block for the fabrication of field-effect transistors [47].

Experimental evidence on the functioning of these novel devices, named *Superconducting Field Effect Transistors* (S-FETs), has been recently reported by Paolucci *et al.* [49, 51, 52].

1.4 Objectives and structure of this thesis

The fundamental goal of the present thesis is the following: *to investigate and exploit the main capabilities of focused ion beam induced deposition of W(CO)$_6$, and to study the superconducting properties of the deposited W-C material*[8]. Three main research lines have been defined in the scope of the current project:

1. **Superconducting W-C nanostructures fabricated by Ga$^+$ induced deposition**. Growth of W-C using Ga$^+$ is the most thoroughly used and studied approach, providing with plenty of well-treaded paths to walk upon. Specifically, the following phenomena have been investigated:
    - Fabrication of nanodevices for non-local vortex transport study.
    - Vortex lattice imaging using scanning tunneling microscopy.
    - Fabrication of proof-of-concept S-FET devices.
2. **Focused ion beam induced deposition of W-C under cryogenic conditions**. Performing ion induced deposition at cryogenic temperatures is a very recently developed technique whose possibilities have been barely explored at the time of writing. In this thesis, an optimization process for W-C, an investigation of the compositional and electrical properties of the yielded material, and application examples of the capabilities of the technique are presented.
3. **Superconducting W-C nanostructures fabricated by He$^+$ induced deposition**. At the time of writing, systematic reports on growth of in-plane W-C nanostructures using this ionic species are lacking from the literature; in part due to the relatively recent commercial availability of the technique. An exhaustive report on the growth parameters and compositional and electrical properties, including investigation on vortex dynamics as well, are to be presented.

This thesis is structured into four main chapters other than this introduction and the conclusions. Chapter 2 provides with a review of the experimental techniques, with particular focus on the growth technique using focused beams of ions. Then, chapters 3, 4, and 5 respectively provide with the results retrieved on the three main goals presented above. Lastly, the conclusions and outlook are presented in chapter 6. Appendix A summarizes the work and results in the Spanish language.

---

[8] Among members of the Institute of Nanoscience and Materials of Aragón and their collaborators, this thesis is the ninth that exploits W-C deposits for different purposes. It is preceded by the work of I. Guillamón (2009), A. Fernández-Pacheco (2009), M.J. Martínez-Pérez (2011), S. Sangiao (2012), R. Córdoba (2012), A.I. Maldonado (2013), I. Serrano-Esparza (2016), and I. García-Serrano (2017).

Chapter 2

Experimental methods and their fundaments

An overview of the experimental techniques used in this thesis is provided in this chapter. They are presented according to their purpose: nanopatterning, structural and compositional characterization, electrical characterization, and others. The first is given particular emphasis given its fundamental importance to the present work.

The content relating to FIB instrumentation development, operation, and theory (previously presented in section 1.2 and now following in section 2.1) has also been utilized in the writing of a chapter in FIB processing in the *Nanolithography techniques and their applications* textbook [53].

2.1 Focused Ion Beam Induced Deposition

Focused Ion Beam Induced Deposition (FIBID), with its name being self-descriptive at this point, is one of the flagship applications of FIBs. With the fundamentals of charged particle interactions having already been discussed in section 1.2, now a description of the instrument used to perform this procedure, and a discussion on the nanopatterning technique are presented in this chapter.

2.1.1 The FIB/SEM instrument

Like other FIB-based procedures, FIBID is performed in dedicated equipment, typically and unoriginally simply referred to as "FIB instruments". A widespread instrument architecture, on which most of the fabrication in the present thesis has been performed, is that of a hybrid microscope that combines a FIB with a SEM column. These FIB/SEM instruments are widely known by their commercial names, such as *Dual Beam* (Thermo Fisher Scientific, formerly FEI), *Crossbeam* (Zeiss), and *MultiBeam* (Raith).

Integrating both a SEM and a FIB column into the same instrument provides with the remarkable advantage of being capable of using the processing capabilities of a FIB while imaging the sample via SEM (section 2.2.1). Except for the He^+ FIBID works, which will be discussed in a later section, all FIBID processes on this thesis were performed in FIB/SEM instruments.

At a fundamental level, the FIB/SEM instrument consists of a process chamber in which the sample is to be placed, and two columns, angled with respect to each other typically between 45 and 55° [54] coupled to it, each providing with a focused beam of charged particles. Different modules are also incorporated into the instrument for various purposes (Figure 2.1).

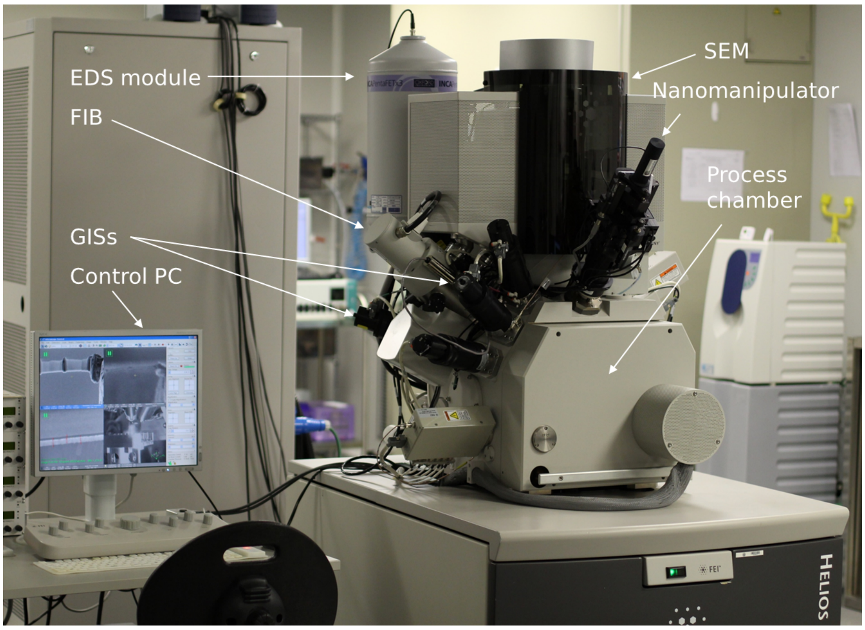

FIGURE 2.1: Thermo Fisher *Helios 600 NanoLab* FIB/SEM microscope. *Photography:* Leyre Hernández.

In the next section, the most relevant constituents of a FIB instrument are revised. Most definitions will refer to the architecture of a FIB/SEM instrument, since it is the one that was used for all Ga^+ FIBID nanofabrication, but omitting the parts referring to the SEM constituents of the equipment, they apply at a basic level to other FIB instruments as well.

The ion source

The beating heart of a FIB instrument is the *ion source*, *i.e.*, the component where the ions that will constitute the FIB are extracted. Located at the top part of the ion column, an intense electric field is applied to a source material to ionize it. The nature and operation of the ion source is of paramount importance in FIB processing, with most features of the beam critically depending on it[1].

The quest for ever-improving ion sources is an ongoing one, and multiple ion source architectures do exist and are currently being proposed. In the present work, two types of ion sources were used: a Liquid Metal Ion Source, and a Gas Field Ion Source.

Liquid Metal Ion Sources (LMISs) get their name from the state the source material they utilize is in. A LMIS is essentially constituted by a reservoir on which the source material is contained, and a sharp needle (typically 1-5 μm in diameter) connected to it (Figure 2.2a). The source material is brought to liquid state, usually by means of a heating coil surrounding the reservoir, wetting the needle below. By applying an electric field at the end of the needle, a Taylor cone forms (section 1.2.2), yielding an effective source diameter of around 2-5 nm, three orders of magnitude below that of the needle tip. A strong electric field (around 10 kV in voltage) in the apex of the Taylor cone induces field-ionization of the metal atoms, which are accelerated down the ion column.

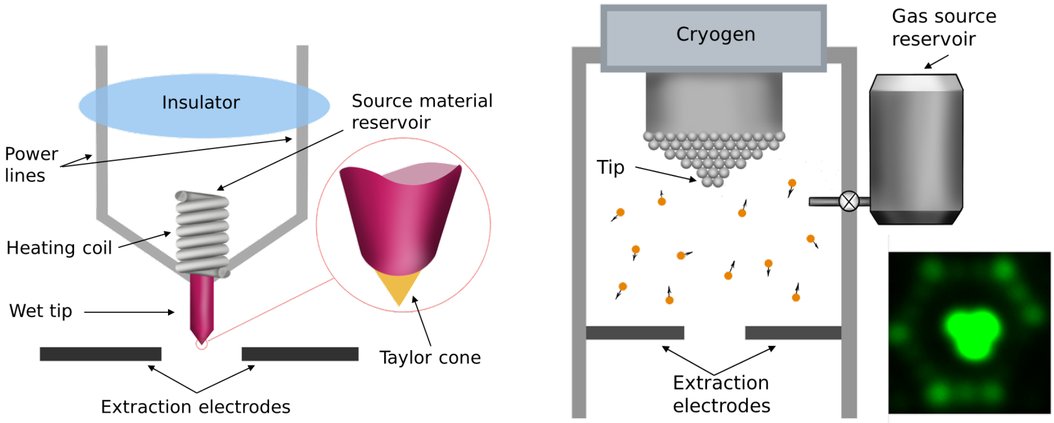

(A) Liquid Metal Ion Source.

(B) Gas Field Ion Source.

FIGURE 2.2: Ion sources. Inset in Fig. 2.2b shows a Scanning Ion Microscopy image of the trimer [55].
Image credit: Rafael Marqués.

The universally used metal in LMISs is gallium, for it exhibits outstanding properties for this very purpose, including a low melting point (29.8°C), low vapor pressure, and stability that leads to long source lifetimes. In this thesis, all Ga^+ FIBID procedures were performed in equipment housing LMISs.

Conversely, obtaining a FIB of He^+ ions requires a different approach to ionize the source material, which is supplied in gas form. Such a challenge is tackled by means of **Gas Field Ion Sources** (GFISs), which also make use of a sharp tip. However,

---

[1] As it conventionally happens in instrumentation development, it is mandatory to find a compromise between that which is useful and interesting, and what is practically doable from and engineering and manufacturing point of view. The development of ion sources is no exception to this trend.

since the Taylor cone gimmick is not exploitable with a source material in gas form, the tip now needs to physically exhibit a nanometer-sized apex in order for the ion source size to be sufficiently small. These *supertips* consist of crystalline tungsten nanofabricated as a series of crystallographic terraces with sequentially diminishing size, down to a single set of three atoms, or *trimer*, located at the tip. Gaseous helium is made flow in the vicinity of the supertip, which is positively biased against a counter electrode (Figure 2.2b).

The potential difference favors the appearance of regions where electrons from the neutral He atoms tunnel into the tip, leaving them positively charged, which in consequence leads them to them being instantly accelerated down the ion column. Furthermore, the supertip is tilted in order for one of the three atoms in the trimer to directly face the ion column axis. With a source size of virtually one atom, GFISs are used for the ionization of noble gases. In the present work, the He^+ FIBID experiments were performed in an instrument equipped with a GFIS. FIB instruments that use He^+ are different enough from those using other species that they have gained their own name - *Helium Ion Microscopes* (HIM).

The ion column

The ion column is the constituent of a FIB instrument on which the beam is constructed. After extracting the ions from the source, the beam is formed, focused, aligned, steered and overall controlled making use of several components present in the column (Figure 2.3).

The two main types of components employed in the ion beam column are *apertures* and *lenses*. An aperture is a physical orifice in a piece that is used to limit the size of the beam, which, in turn, determines the total charge that is allowed to pass down the column, *i.e.*, defining the ion beam current[2]. Electrostatic and electromagnetic lenses are arrangements of electrodes and electromagnets, respectively, that generate electric and magnetic fields used to deflect the descending charged particles. Fine adjustments of the operating parameters of these lenses are constantly performed in FIB operation in order to correct beam aberrations (such as lack of focus or astigmatism) and obtain the optimal working conditions of the beam. Most ion columns define the beam through the usage of two main lenses: the *condenser lens*, located near the source, and the *objective lens*, located near the sample.

Contained within the column are many other elements, including, but not limited to, a *beam blanker* element that is used to steer the beam away from the sample when not in operation, and a conductive cup-shaped element named *Faraday cup* that is used to calculate the ion beam current by measuring the charge it acquires when the beam is steered over it.

---

[2] In equipment that makes use of GFISs, the ion beam current can also be defined by modifying the gas pressure in the source.

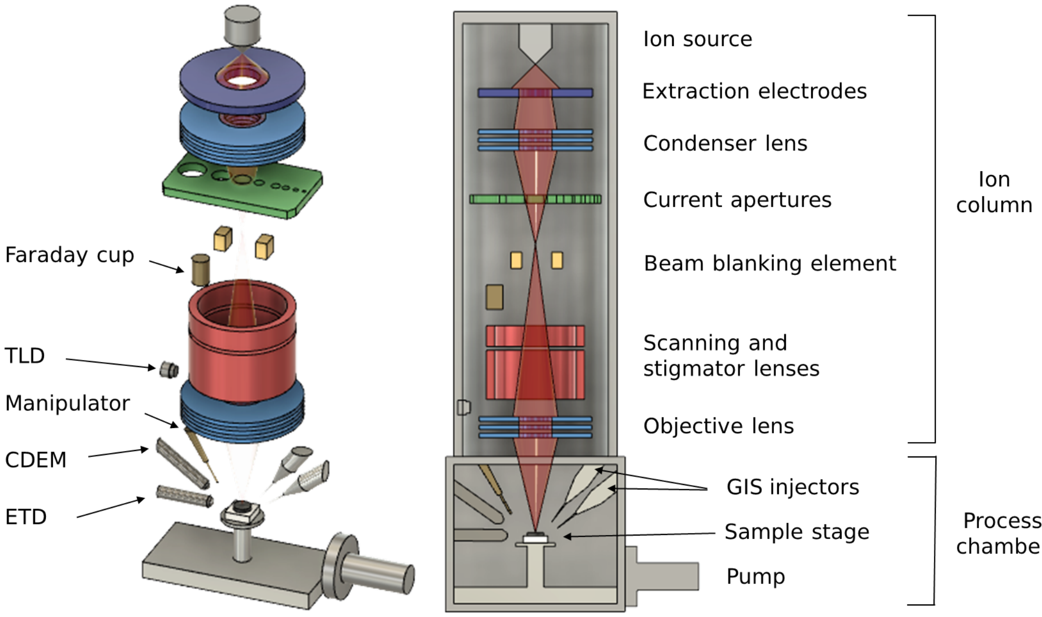

FIGURE 2.3: Overview of the main constituents of a FIB instrument. Not to scale.
Image credit: Rafael Marqués.

The process chamber

The process chamber is the working compartment of the instrument, kept in vacuum during operation. In a FIB/SEM instrument, the two beams converge in it at a geometric point named *eucentric height*. Samples are placed on a moving platform called *stage*, which can be maneuvered in all three spatial directions, rotated around the vertical axis, and tilted with respect to the horizontal up to a maximum value (around 60°). In most FIB/SEM instruments, the SEM column is vertically placed, and the FIB column is found angled with respect to it. For the purposes of (conventional) FIBID, in general normal incidence is preferred, and to achieve it, the stage needs to be tilted during irradiation to match the FIB angle.

Complementary, *in situ* processing instruments are found within the process chamber. Of paramount importance for FIBID, the nozzles through which the gaseous precursor materials are to be delivered are found here, with the reservoirs for the materials located outside the chamber. As a whole, the structure of deposits, valves, and nozzles that is dedicated to storing and delivering these gases is referred to as *Gas Injection System* (GIS). The precursor materials, usually stored in solid state, are sublimated by built-in heaters, and delivered using a nozzle that is, in conventional operation, placed at distances in the 50-200 μm range away from the substrate. Some instruments house different precursor materials in the GIS, and depending on each architecture, each precursor may have a dedicated nozzle, or they may all share a single one, which must be properly purged between injections of different gases.

Other instrumentation also present within the chamber are electrical microprobes, used to perform *in situ* electrical transport measurements, and nanomanipulators, used to handle pieces of the sample, commonplace in the preparation of samples for transmission electron microscopy.

Electron and ion detectors

Most of the relevant information retrieved from a FIB/SEM instrument during processing, including image generation, comes from the detection and interpretation of the charged particles and emitted by the sample as it is irradiated with the beam. Different detector types are set up in the instrument (Figure 2.4) to collect particles of varying nature, according to their type (secondary, backscattered, etc.), which can be mostly determined by the energy they carry, and the angle at which they are emitted. Within the scope of the present work, only relevant electron detectors will be discussed.

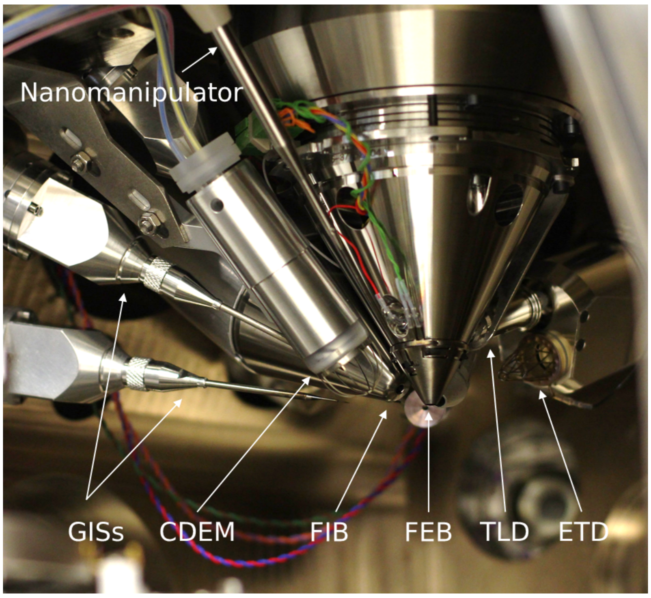

FIGURE 2.4: Process chamber with stage retracted, showing multiple electron detectors and modules in the instrument.
Photography: Leyre Hernández.

Secondary electrons (SEs), which carry information related to sample topography, are collected mainly using an *Everhart-Thornley* detector (ETD), located within the process chamber at an angle of about 30°, and covered with a biased metallic grid named *Faraday cage* designed to attract SEs towards the detector. SEs induce light emission in a scintilating material, which is then amplified using photomultipliers and converted to electrical current using a photocatode. To reduce the noise generated by incoming SE-IIs, which also reach the detector, some equipment have a *Through-the-Lens* detector (TLD) located in the column, outside of the chamber, which makes use of the magnetic field of the objective lens of the column to trap and attract SEs. TLDs also make use of photocatode-photomultiplier setups to convert the signal.

Backscattered electrons (BSEs) are detected only incidentally in the ETD, and usually regarded as an unwanted effect. They are captured using dedicated detectors designed as fixed pieces that cover a large area, upon which the BSEs impinge directly. The signal is processed by either scintillation or by inducing electric excitations on a semiconductor material. While in FIB/SEM instruments imaging is almost exclusively performed with the SEM column, in FIB instruments lacking one (such as HIMs), the usage of a FIB as the imaging probe sets the need for specialized, signal-enhancing detectors. These are called *Channel Detection Electron Multipliers* (CDEM[3]).

2.1.2 The deposition process

FIBID can be defined as a single-step nanopatterning technique based on the local, controlled decomposition of a (generally) gaseous precursor adsorbed on the surface of a substrate. The FIB induces the decomposition of the precursor molecules, which leave a non-volatile constituent permanently deposited on the surface, patterned in the shape scanned by the beam (Figure 2.5).

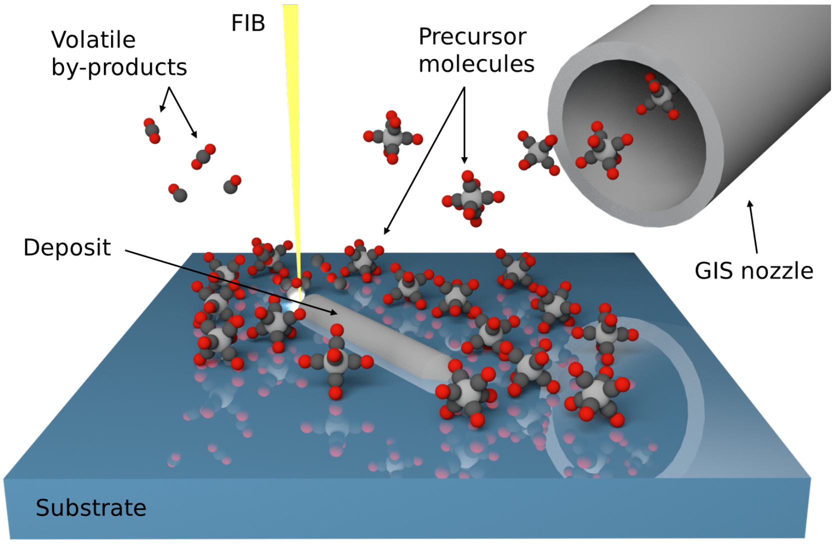

FIGURE 2.5: Overview of the FIBID procedure.

The first step in a FIBID procedure (after any FIB adjustments have been made, section 1.2.2) is the delivery of the precursor material to the surface of the substrate. Except for the notable exception of Cryo-FIBID, which will be discussed latter, this is achieved by injecting the precursor in gaseous form using a nozzle. The gaseous molecules reach the substrate and adsorb there, constituting a molecular monolayer

---

[3] Unfortunately, this acronym also stands for *Continuous Dynode Electron Multiplier*, which refers to a particular architecture of an electron multiplier detector.

on top of it. The nozzle is kept open and continuously delivering precursor during the deposition time to maintain the monolayer in dynamical equilibrium, swiftly replenishing the precursor molecules that leave it when they exceed their residence time on the surface of the precursor. This time depends on the temperature and the sticking coefficient of each precursor-substrate pair.

The second step is the irradiation of the precursor-covered substrate with the FIB, which traces a specific pattern defined by the user. As described in section 1.2, the interaction of the FIB with the substrate results in the emission of different charged particles. SEs play the relevant part on this matter, inducing the decomposition of the adsorbed precursor molecules:

$$\mathrm{W(CO)_6} + \text{electrons} \longrightarrow \mathrm{W} + 6\,\mathrm{CO}\uparrow + \text{electrons}$$

This relation is evidently an oversimplification, but provides with an intuitive view of the mechanism that drives the technique. The adsorbed precursor molecules get locally decomposed at the point the FIB is focused at by interacting with the SEs emitted there; and get separated in two constituents: a volatile part that is pumped away by the vacuum system, and a non-volatile component that remains on the substrate, constituting the deposit.

Actual precursor decomposition is only partially achieved in the manner described in the previous relationship. Incomplete dissociation is bound to occur in most processes, and, as such, some constituents other than the target element in the precursor will be significantly present on the deposit. In addition, the quality of the vacuum in the process chamber also determines how tainted the deposit will get by the presence of contaminant species (hydrocarbons, water molecules, pump oils) if any.

The bottleneck that sets the upper limit of the growth speed is either the amount of precursor the FIB has available to decompose, or the number of generated SEs that are generated upon FIB irradiation. In consequence, depending on the relative importance of each, FIBID takes place in either the *electron-limited regime*, or in the *precursor-limited regime*. In the former, the precursor is constantly delivered and replenished at a much faster rate than it is decomposed; while in the latter this relative speed is reversed. With no precursor available for decomposition, in the precursor-limited regime some side effects such as FIB milling can appear. In the present work, depositions at room temperature have always been performed in the electron-limited regime.

The beam traces a pattern over this dynamically-replenished precursor layer. As it will be later discussed, several operating parameters are adjusted to obtain the required results within the limits of the technique.

2.1.3 Operating parameters

One fundamental parameter in FIB operation is the *spot size*, *i.e*, the physical size over which the beam extends in a single, localized irradiation. In general, the lower the ion beam current, the smaller this area will be. A small spot size can be considered an interesting advantage if lateral patterning resolution is required, or a major drawback if very large areas are to be grown.

Any pattern traced by a FIB should be thought of as a succession of such spots, all identical to each other and in close proximity. A geometrical figure traced by a FIB is actually a series of irradiation spots in close proximity to each other, and potentially overlapping, over which the FIB has been individually steered (Figure 2.6).

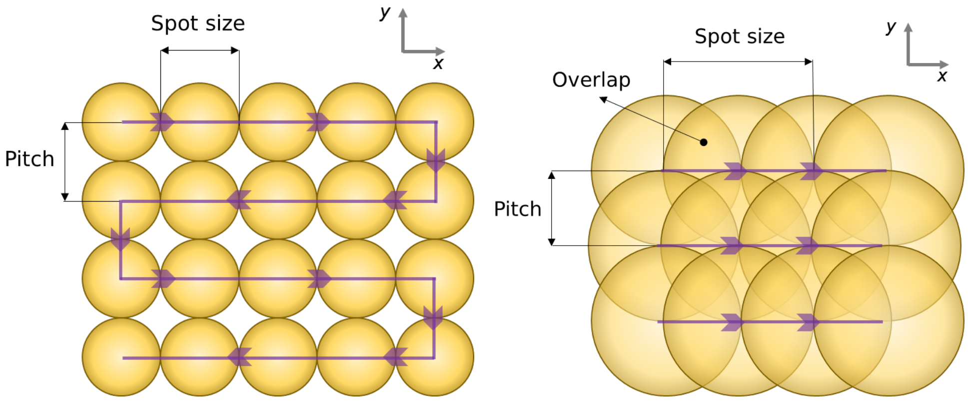

(A) 20 spots, 0% overlap, serpentine scan. (B) 12 spots, 50% overlap, raster scan.

FIGURE 2.6: Diagram of FIB scanning of the same rectangular pattern using different operation parameters. If the dwell time is set to the same value in both scanning types, approach in Figure 2.6b will be faster.

The most relevant operating parameters in FIB processing are the following:

- The *acceleration voltage* is the energy of the ions, up to which they have been accelerated down the ion column. This parameter defines the interaction volume (section 1.2.2) and is usually set to 30 kV. Generally speaking, greater lateral resolution can be achieved using high acceleration voltage, at the cost of a reduction in the growth rate.
- The *ion beam current* is, by definition, a measure of the electric charge delivered to the substrate per unit time. It is adjusted by selecting an aperture, or, in the case of GFISs, by modifying the gas pressure at the source. The ion beam current determines the spot size of the beam, which in turn limits the lateral resolution of the deposits.

- The *dose* is the charge received by a material per unit area in a given time interval. In the context of FIB processing, the term *fluence* is sometimes interchangeably with the concept of dose[4].
- The *volume per dose* is a figure-of-merit that is used to assess the efficiency of a nanoprocessing procedure. It is defined as the ratio between the volume of the processed feature (a deposit or a hole), and the total charge received by the substrate, which is extracted from the dose.
- The *dwell time* is the time spent by the FIB on each of the aforementioned irradiation spots. Typically, this parameter must be adjusted so the FIB has enough time to dissociate the required amount of precursor without completely depleting it (which would result in milling).
- The *refresh time* is the total time spent by the FIB tracing a single scan of the pattern, *i.e.*, the dwell time times the number of irradiation spots, (with a full scan referred to as a *pass*), plus any wait time set between passes, usually to ensure precursor replenishing. In some contexts, this term is used to refer to the wait time only, on which the precursor is *refreshed*.
- The *pitch* is the physical separation between two consecutive irradiation spots in an in-plane direction. In most cases, this value is set below the spot size of the beam, so successive irradiation spots overlap with each other. The pitch can also be directly controlled by directly adjusting the *overlap*, which is expressed in terms of the estimated spot size.

2.1.4 FIBID under cryogenic conditions

Fundamentals

FIBID under cryogenic conditions, or Cryo-FIBID, is a very young technique that stems as a variation of conventional Ga^+ FIBID, the difference between the two being that the procedure is performed at cryogenic temperatures, in the vicinity of -100°C [56], rather than at room temperature.

One of the features of room-temperature FIBID is the fact that, even in the electron-limited regime, the amount of precursor that is available for FIB decomposition is always capped by the fact that a single molecular monolayer of adsorbed gaseous precursor molecules can be present at a given time. Gaseous precursor molecules do not adsorb on top of each other, but rather on the surface of the substrate and of that of already deposited material (this being the principle on which 3D FIBID is grounded). Hence, there is a relatively low upper limit on the processing speed of FIBID, since in the precursor-limited regime, no more than a single (dynamical,

---

[4] *Dose* is a "practical" term, used to quantify the irradiation a material (or a person) has acquired upon a limited exposure to the irradiating source. *Fluence* is a more formal, mathematical term, defined as the charge passing through a given volume, divided by the cross-sectional area of that volume. For the present matter, the difference is not relevant.

constantly replenished) precursor monolayer is being processed at the same time, independently of any other experiment parameter.

The volatile nature of the precursor monolayer is intrinsically related to the fact that the precursor is *in gas state*. While delivering the precursor in liquid or solid state would prove cumbersome in the vacuum of the processing chamber, having a thicker, non-gaseous precursor coverage would be of great interest, provided the FIB were able to decompose it as efficiently as the gaseous one.

Cryo-FIBID achieves such a layer by performing an *in situ* condensation of the precursor by cooling the sample below its condensation temperature. While the precursor is still delivered in gas phase, it condensates as soon as it reaches the cooled substrate, with arriving gaseous molecules condensing on top of those already delivered. The resulting condensate, which the FIB can indeed decompose, is much thicker than the gaseous monolayer that is achieved at room-temperature, which in turn highly increases the processing speed by up to three orders of magnitude.

Two technical differences from conventional FIBID (apart from substrate cooling) are worth mentioning. First, to limit the amount of precursor that condensates on the substrate, Cryo-FIBID is usually not performed at the working height of the instrument, but rather far from it. Since most instruments are calibrated to optimally work at the eucentric height, some additional care must be taken, such as ensuring that the beam is still as focused as possible (far from the eucentric height), and that no funny situations related to the geometry of the GIS injectors arise[5]. Second, and contrary to room-temperature FIBID, the precursor is not continuously delivered during deposition, but rather before it and in a single, discrete gas injection before irradiation. The duration of this delivery represents a new controllable parameter that can be toyed with when performing Cryo-FIBID.

A typical Cryo-FIBID procedure can be described as a cooling-irradiation-heating cycle (Figure 2.7). First, the sample stage is brought to the required processing distance and the FIB is focused therein. Then, the sample is cooled down below the precursor condensation temperature and the precursor is delivered in the manner just described. It immediately condensates on top of the substrate, and then the irradiation is performed. Thereafter, the sample is brought back to room temperature in slow steps. A soft "baking" at 50°C (around 15 minutes) can be performed to ensure any adhered condensate leftovers are eliminated. It must also be kept in mind that despite the impressive swiftness of the actual deposition, the cooling and heating times have too be added to the exposure time. In average, a cooling-irradiation-heating cycle may take between 30 and 60 minutes. For that reason, it is advisable to

---

[5] For instance, if the required GIS nozzle is not movable and is positioned at a a very low angle with respect to the horizontal, the bulk of the precursor it delivers will not reach the irradiation point if the stage is positioned very far from the working distance. There is definitely room for creativity here, such as first delivering the precursor, and then moving the stage so that the beam does irradiate the area where it has actually been delivered.

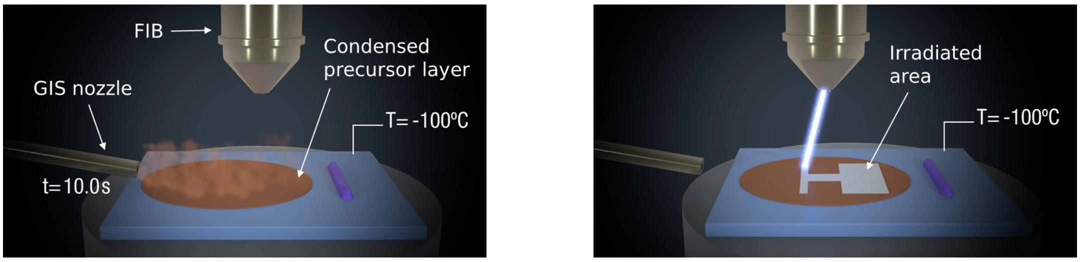

(A) Formation of a condensed layer at low temperature.

(B) Pattern tracing over the condensate.

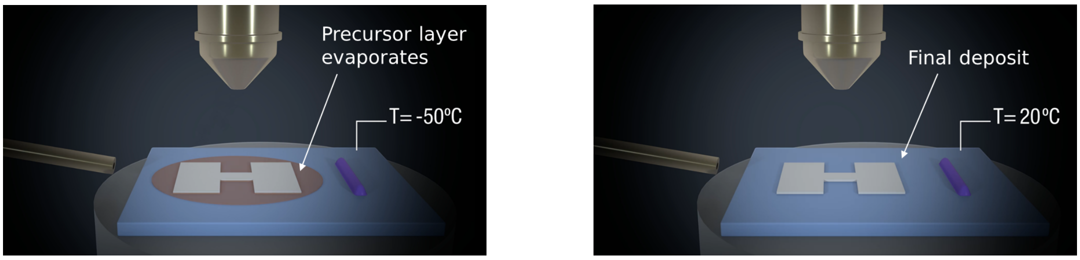

(C) Removal of unexposed areas by substrate heating.

(D) Final deposit after complete evaporation of the condensate.

FIGURE 2.7: Steps of Cryo-FIBID [56].

make the most out of each irradiation, growing multiple samples at the same time when possible.

The growth mechanism of Cryo-FIBID is, while still founded on the same grounds as conventional FIBID, different to the standard considerations of precursor decomposition. As such, geometrical, structural, and compositional differences in the material that results by decomposing the same precursor are to be expected, and are indeed found (section 4.3).

While still on its infancy, Cryo-FIBID does exhibit the potential to establish itself as a solid alternative to FIBID in more "bulky" processes that require the deposition of large amounts of material while maintaining a reasonably high lateral resolution. Reducing the processing time does entail the less-flashy but equally, if not more, important consequences of avoiding instrument instability and external disturbances during very long exposure processes. For instance, it is unlikely that the finely-tuned beam conditions achieved at the beginning of a deposition of (say) 90 minutes will be maintained throughout. The beam may drift from the intended position, the stage can move (either by electrical instability, ground vibrations, or a lab colleague closing the door a little more harshly than it would be convenient), and a constant delivery of gas into the chamber during such a prolonged time interval cannot be guaranteed. Furthermore, the usage of this technique effectively lengthens the ion source lifetime and delays the need for precursor material replacement.

Experimental setup

The Cryo-FIBID works were performed in a commercial Thermo Fisher *Nova 200* FIB/SEM instrument with a cooling module (Quorum Technologies PPT2000) based on cooled gaseous nitrogen (Figure 2.8).

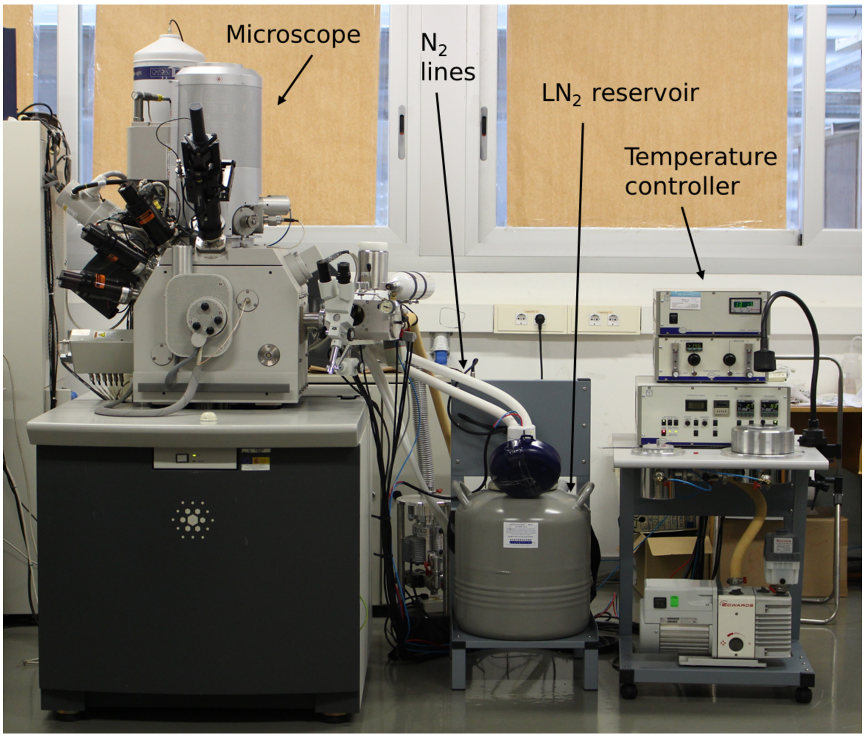

FIGURE 2.8: Thermo Fisher *Nova 200 NanoLab* FIB/SEM microscope with temperature control module.
Photography: Leyre Hernández.

The refrigeration module consists of an open circuit of gaseous nitrogen (N_2), externally supplied from a reservoir. N_2 initially flows from a pressurized bottle along two rubber tubes which are then placed inside a metallic coil. This coil is submerged in liquid nitrogen (LN_2), which is at a temperature of 77 K (around -196°C). N_2 flowing inside the coil rapidly cools losing heat to the cold reservoir, and is then made flow towards the sample, located into the processing chamber of the FIB/SEM instrument. The rubber tubes are placed in direct contact with a metallic sample holder in the sample stage, swiftly cooling and maintaining a stable temperature as long as the gas keeps flowing (Figure 2.9). After reaching the sample holder, the tubes lead the gas out of the chamber, where it is evacuated to the ambient. The minimum achievable temperature can be moderately adjusted by modifying the gas pressure, but in any case it has a lower bound of -155°C.

While the N_2 circuit provides with the base cooling required to work at cryogenic temperatures, the fine control of the temperature is achieved by means of a built-in heater in the sample holder. The stage temperature is externally controlled by defining a setpoint in this heater, which takes into account the cooling provided by

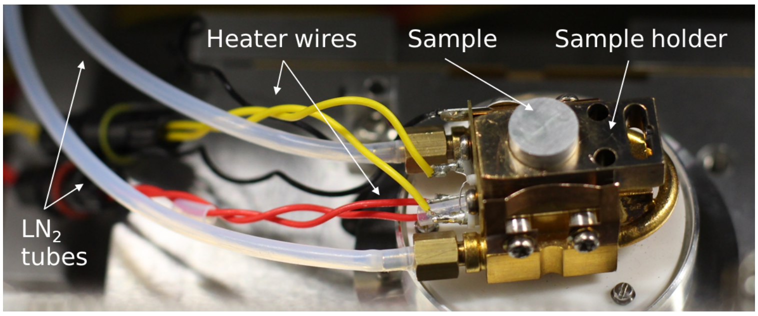

FIGURE 2.9: Sample stage for Cryo-FIBID in the *Nova 200 NanoLab* FIB/SEM microscope.
Photography: Leyre Hernández.

the N_2. The heater can also be utilized to drive the sample holder temperature up to 50°C.

Other than that, the equipment disposition remains equivalent to a conventional FIB/SEM setup. One severe drawback of this refrigeration approach is that the continuous passage of gas through the tubes surrounding the sample holder makes the sample vibrate, also yielding a net stage drift over time. The presence of the tubes also limits the mobility of the stage, which is constrained to very small in-plane rotations[6]. It is also advisable to perform tilting in small steps rather than in one continuous sweep, particularly at low temperature, to reduce stress on the tubes.

Before defining a precise guide on performing Cryo-FIBID, an important matter merits discussion first: since the deposition (or, more precisely, the precursor delivery) is performed 10 mm away from the GIS nozzle. The reason for this requirement stems from the fact that the condensate forming on top of the substrate grows in thickness very fast, posing a two-fold issue:

- The thickness of the layer that is to be deposited directly depends on the total amount of condensed precursor available for decomposition. A single irradiation could potentially decompose the whole layer of precursor, unlike in conventional FIBID, where only a single precursor monolayer is available. Therefore, and in combination with a discrete (rather than continuous) injection of precursor gas into the chamber, the thickness of the condensed layer is regulated by distancing the stage away from the GIS nozzle.
- An indiscriminate, uncontrolled growth of the condensate layer could lead to effective thicknesses of several mm. Should this happen at the eucentric height, the condensate could potentially enter in direct contact with fragile instrument components closely located above it (detectors, etc). This represents a serious hazard to the equipment, and as such it must be avoided.

---

[6] Fortunately, for most purposes this issue can be overcome by rotating either the beam scan direction, or the orientation of the patterns.

Most components in the instrument (detectors, lenses in the column, and GIS nozzles) are positioned within the instrument and optimized for best performance when the sample is at the eucentric height. As a consequence, extra caution must be taken when assessing the operation parameters and quality of the procedure. The advantage of simultaneously sharing the field of view with both the FIB and the FEB is evidently lost when working far from it, and as such, one of the obstacles to overcome in Cryo FIBID is now evident: it is not possible to retrieve SEM images prior to deposition, and all sample positioning must be made using the FIB.

The consequences of this feature are indeed significant, both coming from the inherent sample damaging induced by the FIB, and the (usually) added difficulty that imaging a sample with Ga^+ FIB represents. While at the eucentric height, it can be useful to mill some distinguishable features on the surface of the substrate near the area of interest. They can be used to facilitate positioning and FIB focusing without irradiating the area of interest, minimizing the ion dose it receives.

In addition, and also due to this very large working distance, significant differences between the nominal values of the dimensions of the patterns and the actual size of the deposits do arise as well, since the instrument is optimized to grow patterns at the eucentric height. The length correction factor is found to depend on the specific geometry of each deposit and on the scanning direction of the beam, but the ratio between the nominal value of a length and its real value ranges between 1.15 and 1.30 in most cases. If necessary, it is of use to grow a test sample to precisely define the correction factor for that deposit, and then recalculate the deposition time accordingly (section 4.2.1).

On this thesis, the applicability of Cryo-FIBID for the growth of W-C via decomposition of $W(CO)_6$ is reviewed, with chapter 4 devoted to that purpose. The results of the study, as well as a brief review on the state of the technique at the time of writing, can be found there.

2.1.5 Numerical simulations of trajectories of charged particles

Further insight on the mechanism and boundaries of specific growing conditions can be gained by computationally simulating the trajectories followed by the ions or electrons as they impinge on a certain material with a given energy.

On the present work, the open software *Stopping and Range of Ions in Matter* (SRIM) [23], based on the 1980s program *Transport of Ions In Matter* [57], was used to estimate the projected ion range in different experimental conditions. The interaction volume is calculated by simulating the trajectories of a fixed number of ions as a series of individual binary collisions, on which the ion gradually loses energy.

To estimate the interaction volume when using electrons as a probe, of relevance when performing electron-based spectroscopy (section 2.2.2), the (also open) software *Monte Carlo Simulation of Electron Trajectory in Solids* (CASINO) was also used.

In a similar way to SRIM, it makes use of Monte Carlo methods to simulate a large number of electron trajectories under adjustable conditions.

2.1.6 Summary of FIBID experimental conditions

As it is evident at this point, the FIBID technique is the cornerstone of the present work. It has been used to induce the deposition of a W-C material via the decomposition of the $W(CO)_6$ precursors. Three scenarios have been assessed: conventional, standardized deposition using Ga^+ ions; novel, ultra-fast growth using Ga^+ ions in cryogenic conditions; and highly-precise, less aggressive fabrication using He^+ ions. The experiments were performed in the following commercial equipment: Thermo Fisher *Helios 600 NanoLab Dual Beam* (FIB/SEM), Thermo Fisher *Nova 200 NanoLab Dual Beam* (FIB/SEM) with a Quorum Technologies PPT2000 cooling module; and Zeiss *Orion NanoFab* (HIM), respectively.

Table 2.1 shows the most typically used parameters for each scenario. Since several experiments were performed in that, the specific conditions for each instance and more details are indicated on their corresponding section. In some "extreme" cases, such as the fabrication of very large thin films for vortex lattice imaging (section 3.4) the used conditions significantly differ from those shown in table 2.1.

Unless explicitly stated otherwise on the corresponding section, silicon substrates with a 300 nm-thick thermally-grown SiO_2 layer on top were used as substrates. A series of titanium pads were grown using optical lithography on top, to which the electrical contacts would be placed thereafter. Electrical contacts between the samples under study and these Ti pads were placed by Ga^+ FIBID of the platinum-based $(CH_3)_3(CH_3CpPt)$ precursor, whose deposition yields a Pt-containing, conducting material. This growth of Pt was performed in Thermo Fisher *Helios 600 NanoLab Dual Beam* and *Helios 650 NanoLab Dual Beam* FIB/SEM instruments.

	Ga^+ FIBID	Cryo Ga^+ FIBID	He^+ FIBID
Instrument	*Helios 600*	*Nova 200*	*Orion*
Acceleration voltage	30 kV	30 kV	25-30 kV
Ion beam current	1.5-10 pA	1-10 pA	15 pA
Ion dose	$4.88 \cdot 10^{-1}$ nC/μm^2	$5.5 \cdot 10^{-4}$ nC/μm^2	0.7-2.0 nC/μm^2
Base pressure	10^{-6} mbar	10^{-6} mbar	10^{-7} mbar
Deposition pressure	10^{-5} mbar	Not applicable	10^{-5} mbar
GIS nozzle distance	50-100 μm	10 mm	50-100 μm
Substrate temperature	Room	-100°C	Room

TABLE 2.1: Typical parameters used in all three FIBID procedures.

2.2 Compositional and structural characterization

The experimental techniques that were used to assess the structure and composition of the grown samples are reviewed here.

2.2.1 Scanning Electron Microscopy

SEM imaging, readily available in the FIB/SEM instruments employed to perform Ga^+ FIBID, was used to assess *in situ* the shape fidelity of the deposits after they were grown.

To perform SEM, the focused electron beam (FEB) is scanned in a similar way to the operation of a FIB described in section 2.1.3. Interaction of the electrons from the beam induces emission of SEs and BSEs, which are collected by the electron detectors and then processed to generate a contrast image. SEs mostly carry topographical information, while the contrast in BSE-generated images relates to the composition of the sample, since the BSE yield strongly depends on the atomic weight of the atoms in the substrate.

In order to avoid unwanted FEB-induced deposition of chamber contaminants or remainders of previously injected gaseous precursor materials, a preventive wait time before imaging was always maintained after sample loading and after depositions.

SEM imaging of the samples was performed in *Helios 600 NanoLab Dual Beam* and *Helios 650 NanoLab Dual Beam* FIB/SEM instruments.

2.2.2 Energy Dispersive X-Ray Spectroscopy

Energy Dispersive X-ray Spectroscopy (EDS or EDX) is a compositional characterization technique that makes use of a focused beam of electrons to induce the emission of characteristic X-rays by the sample under study.

Electrons in the beam transfer their energy to the atoms in the sample, inducing electronic transitions in the atoms of the sample, which, in de-excitation, emit X-rays with very definite energies, characteristic of different elements and acting as a fingerprint of their presence in the sample. The relative counts provide with information on the relative presence of each element in the sample.

EDS over whole samples was performed in *Helios 600 NanoLab Dual Beam* and *Helios 650 NanoLab Dual Beam* FIB/SEM instruments, and in a Thermo Fisher *Inspect F50* SEM instrument. Precise EDS in localized areas in sample lamellae was carried out in a Thermo Fisher *Titan Low Base* transmission electron microscope.

2.2.3 Transmission Electron Microscopy

Transmission Electron Microscopy (TEM) is an extremely powerful characterization technique, capable of achieving sub-nanometric resolution, based on the study of the interactions of a highly energetic (300 kV) beam of electrons that is *transmitted* through a fine slice of the sample under study. TEM can be used to analyze the cross sectional profile with resolution of one order of magnitude above that of a conventional SEM (0.08 over 0.9 nm for the used instruments, respectively). The structural information, from which possible crystallinity is detected, is retrieved from these cross-sectional images by extracting the Fast Fourier transform of the image, where the diffraction spots and can be indexed, if present.

In the present work, the following operating modes of TEM have been used: *High Resolution TEM* (HRTEM), employed to discern atomic planes and assess possible crystallinity on the samples; and *Scanning TEM* (STEM), a variant of TEM on which the electron beam is scanned through the sample, akin to SEM, instead of illuminating the whole area under study. In STEM mode, a particularly useful approach *High Angle Angular Dark Field* (HAADF) imaging. Instead of conventionally collecting and detecting the electrons that are transmitted in the vicinity of the axis of the main beam, only those that have been scattered at high angles are recorded, using an annular detector placed for this purpose. The scattering of the electrons depends on the atomic number of the constituents of the samples, and, as such, STEM-HAADF images provide with compositional contrast, similarly to those generated by BSEs in SEM. In addition, while in STEM mode, the fine electron probe can also be used to perform EDS and analyze the local composition of the sample.

TEM studies were performed in the present work in the commercial TEM instruments by Thermo Fisher *Titan^3*, *Titan Low Base* (Figure 2.10), and *Tecnai F30*. Sample preparation and TEM operation were carried out by on the Laboratory for Advanced Microscopies.

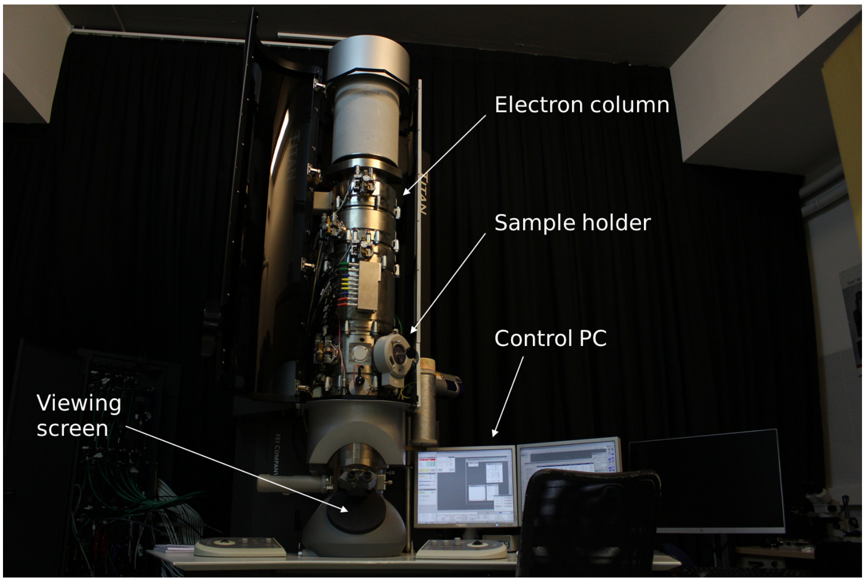

FIGURE 2.10: Analytical *Titan Low Base* TEM microscope.
Photography: Leyre Hernández.

2.3 Electrical magneto-transport measurements

2.3.1 Overview

Magneto-transport is a term typically used in the field of semiconductors to refer to study the electrical properties (*i.e.*, the *transport* of electrons) in presence of a magnetic field. While semiconductors are not the object of study of this thesis, such a characterization is particularly useful for superconducting samples as well, since, as described in section 1.3, the magnetic field is one of the bounding parameters of the superconducting state, and it plays a fundamental part in studying non-local vortex transport.

The electrical magneto-transport characterization of the samples was performed on a commercial instrument called *Physical Property Measurement System* (PPMS), by Quantum Design. It is equipped with a holder on which the samples are placed, which are then kept in vacuum conditions. Electrical contact between the sample and the sampleholder is achieved by means of ultrasonic wire bonding, a technique through which fine aluminium wires are placed to join one with the other.

The PPMS instrument equipped with a Helium-3 refrigerator insert, capable of lowering the temperature of the sample down to 0.35 K, and with a superconducting magnet capable of providing magnetic fields up to 9 or 14 T (depending on the instrument model), both in-plane and perpendicular to the plane of the sample. In most cases, the PPMS instrument is operated by taking successive readings of resistance R in terms of driving current I[7] (making use of four probes), while the temperature and the magnetic field are modified according to the needs of the experiment.

Each data point returned by the equipment is retrieved as an averaging of a fixed number of readings, which the instrument is told by the operator to assume as equivalent. For the present matter two operation modes are of relevance: the *AC* and *DC* mode.

The current source is synchronized to the grid frequency (Spain, 50 Hz), and provides with a square wave of frequency equal to one third of the grid's (8.3 Hz, or 120 ms per cycle). In AC mode, the resistance is read for each half of the cycle (positive and negative, 60 ms each), and the two values are averaged over the fixed amount of cycles to retrieve a single data point. This approach enables for cleaner data, eliminating internal offsets of the instrument and removing some thermoelectric effects in the sample. In DC mode, only one half of the cycle, defined by the user, is taken into account to perform the averaging.

AC mode provides with enhanced noise reduction when compared to DC mode, but at the cost that the device under study is assumed to yield a symmetrical resistance response in terms of the sign of the current. If it does not, some information is

---

[7] The instrument actually reads voltage, V, as a function of current, but returns data in terms of resistance, recalculating it following Ohm's law, $R = V/I$.

lost on the averaging process, which can yield results lacking physical sense, such as negative values of electrical resistance. Caution must be taken, therefore, when selecting the most appropriate operation mode.

2.3.2 Local resistance

The immense majority of electrical measurements that are performed in the matter of electrical characterization of devices are performed in what, in the present text, shall be referred to as *local mode*. The term *local* is used to indicate a (typically assumed) configuration on which the voltage is being read in the same area on which the current is flowing, *i.e.*, *locally*.

This clarification may come as surprising to some, for in most conventional, typical applications, the voltage read in areas depleted of current is zero. What would be the point of measuring voltage in a region when there is none? For that reason, the term *local* is used here for comparative purposes, to distinguish these measurements from those not performed locally. It is common in the literature, when such comparison is not necessary, to simply drop the term and refer to the measured parameter as by its name, without further clarification.

In any case, in the present work the term *local* will be referred to all measurements on which voltage is being measured in an area between two points, through which a driving current is flowing (Figure 2.11a). In most cases, such a measurement will be performed in the so-called *four-probe* configuration: two contacts, or *probes*, are used to inject the driving current, and two more are used to measure the voltage. The main appeal of this configuration is that no current flows through the voltage leads, and as such, only the voltage of the sample is measured. The contact resistance does not contribute in this configuration.

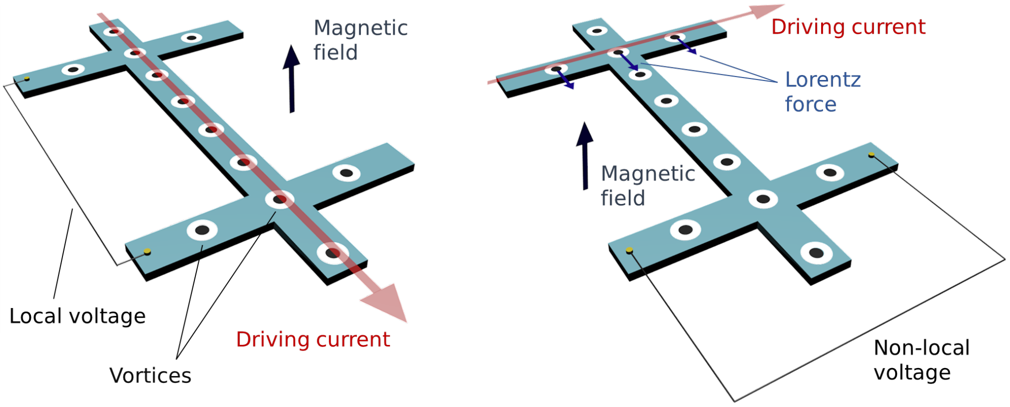

(A) Local mode.

(B) Non-local mode.

FIGURE 2.11: Contacting modes.

2.3.3 Non-local resistance

Non-local voltage measurements are performed by measuring voltages in areas different to those where the driving current is being injected, and which are, in principle, depleted of it. The idea behind these measurements is that the driving current will induce some physical effect, different from conventional electrical resistivity, that will result in the appearance of a finite, measurable voltage in a different location in the sample.

Specifically in the context of this thesis, non-local measurements are performed in nanodevices patterned as a long channel crossed by two perpendicular leads at its ends. The driving current is injected at one of them, and the voltage is measured at the other (Figure 2.11b).

As described in section 1.3.5, in presence of a magnetic field perpendicularly applied to the direction of the plane, the driving current exerts a Lorentz force on superconducting vortices present on the current lead, pushing them in a direction that is perpendicular to both the applied field and the direction of the current, *i.e.*, along the longitudinal axis of the nanostructure. The energy dissipated by the vortices as their normal cores drift across the superconducting bulk yields a measurable voltage, which is measured in the voltage leads.

2.4 Scanning Tunneling Microscopy

2.4.1 Overview

Scanning Tunneling Microscopy (STM) is a characterization technique[8] based on the *tunneling* effect that happens when a polarized sharp tip is brought in close proximity to a sample or substrate. In (conventional) STM operation, an atomically sharp tip is brought to close proximity of the sample under study, and a bias voltage is applied between the two. Electrons from the tip are attracted to the sample (or the other way around, depending on the relative polarization between the two) with the vacuum separating the two acting as a potential barrier. While conventional conduction is not possible due to the existence of this barrier, electrons do have a nonzero probability of *tunneling* through the vacuum that separates the two. The probability of these tunneling events exponentially decreases with increasing distance, and as such, the tunneling current that is established between the sample and the tip acts as an extremely precise probe of the nature of the surface below.

A complete description of the technique and of the tunneling phenomenon is far beyond the scope of this thesis. However, one further remark needs to be made: for tunneling to occur at all, electronic states on which the electrons coming from the tip can enter must exist on the sample. The distribution of electronic states is

---

[8] STM can also be used to perform manipulation of individual atoms and molecules, and as such can also be considered an extremely powerful nanofabrication technique.

referred to as *density of states*, and there must be an overlap between the tip and the sample in order to establish a current. For that matter, STM is usually thought of as an *spectroscopic* technique, since what is actually being probed is the density of states of the sample, rather than the topographic features of its surface.

Moreover, this nuance will prove extremely relevant for this thesis, since it happens that in the samples under study, the density of states is far more interesting than the topography. In fact, STM is as useful for electronic state probing than it is for topography, if not more. In the present study, STM characterization can be exploited for imaging of the Abrikosov lattice. The existence of a superconducting gap in the density of states of a superconductor (section 1.3.2), *i.e.*, a finite range of electron energies along which no electronic states can exist, allows for clearly discerning superconducting vortices from the surrounding, superconductor bulk. Greater values of the tunneling current are expected when the tip is positioned above the normal core of a vortex, where the superconducting gap is absent, with the superconducting gap severely restricting tunneling conductance in the bulk. This operation mode is named *Scanning Tunneling Spectroscopy* (STS). In the context of the present thesis, STS was used to retrieve spectroscopic images of the Abrikosov lattice, not unlike it has been done before [58–60].

2.4.2 Experimental details

The experiments were performed in a SPECS *Joule-Thomson* STM [61] in ultrahigh vacuum (pressure below 10^{-10} mbar) at temperatures between 1.15 and 3.41 K (Figure 2.12).

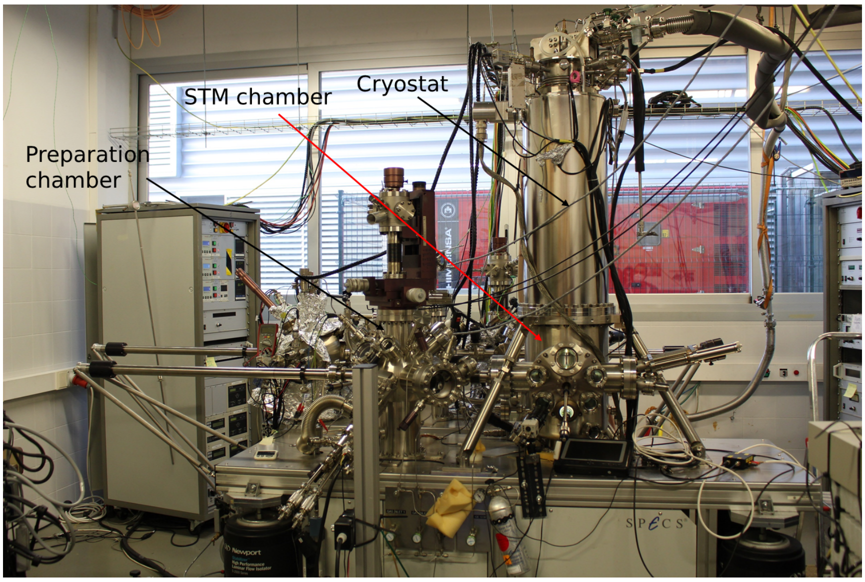

FIGURE 2.12: SPECS *Joule-Thomson* STM instrument.
Photography: Leyre Hernández.

A W tip fabricated by potassium hydroxide electrochemical etching was used for the measurements. The fabrication of the substrate and sample merit special discussion, presented later in section 3.4.1. It was mounted in the STM sample holder using Mo wires. The tip was grounded and sample bias convention was used. Images were taken with a current of 5 pA and a bias voltage of 2 V. Each $I - V$ measurement roughly took 3 minutes.

The differential conductance data were acquired using a lock-in amplifier at 961 Hz (optimized in the equipment to remove all unwanted noise sources). dI/dV curves are extracted by performing a voltage sweep within the required range of bias voltage applying an oscillating "probe" voltage to the sample of finite amplitude, named modulation voltage. The dI/dV curves are extracted by analyzing the variation of I within each finite voltage step. In the present experiment, the modulation voltage was set to 0.5 mV. Obtaining a full-sized STS image (such as the one later shown in Figure 3.15b) typically took around 12-13 hours.

Chapter 3

Ga^+ FIBID of superconducting nanostructures

In this chapter, the labor done on three lines of work that make use of Ga^+ FIBID W-C are reported. After a brief introduction on previous work and growth and characterization procedures, results on the following topics are reported:

- Non-local vortex transport in superconducting channels, 50 nm in width (section 3.3). In addition to the experimental work, numerical simulations based on the Ginzburg-Landau theory were carried out in collaboration with the *Condensed Matter Theory* group in the University of Antwerp (Belgium). Specifically, the work on these simulations was performed by Ž. Jelić and M. Milošević.

- Growth of films for STM investigation, and vortex lattice imaging (section 3.4), in collaboration with the A. Domínguez and D. Serrate, from the *Nanofabrication and Advanced Microscopies* research group in the University of Zaragoza.

- Field effect on narrow nanowires, achieving local suppression of superconductivity via the application of a gate voltage (section 3.5).

3.1 State of the art

If FIBID can be considered one flagship of FIB processing, then Ga^+ FIBID, stands proudly at its bow - FIBID using Ga^+ ions is undoubtedly the most extended, used, and readily-available facet of FIBID. Tungsten-containing deposits are grown using tungsten hexacarbonyl, $W(CO)_6$ as a precursor material. They exhibit significant amounts of C in terms of atomic composition, present as leftover constituents in incomplete precursor dissociation.

The interest in growth of W-C using FIBID was notoriously sparked by the 2004 work of Sadki *et. al*, where superconductivity of the material was reported for the first time [62], and extensive work has been carried out on the matter ever since (table 3.1).

	Resistivity ($\mu\Omega$·cm)	T_c (K)	W:C:Ga:O (atomic %)	Microstructure
Sadki, 2005 [63]	200	5.2±0.5	40:40:20:0	Amorphous
Luxmoore, 2007 [64]	200	5.5±1.0	51:37:12:0	Nanocrystalline order
Spoddig, 2007 [65]	-	5.2 ± 0.5	17:35:13:4	-
Li, 2009 [66]	100-350	5.0-5.5 ± 0.3	53:34:11:2	Nanocrystallite clusters
Li, 2011 [67]	330	5.0± 0.3-0.6	48:30:16:6	Nanocrystallites
Córdoba, 2013 [68]	275	4.3±0.3	40:43:10:7	Nanocrystallites

TABLE 3.1: Reported properties of Ga$^+$ FIBID W-C nanostructures.

The W-C material grown via Ga$^+$ exhibits relatively low values of room-temperature resistivity, roughly around 200 $\mu\Omega\cdot$ cm, that enables the deposits to be used as intermediate contacts in the electrical characterization of other samples. In addition, the material is also sturdy and robust, as evidenced by experimental studies on their mechanical properties, performed by probing suspended nanowires grown over trenches [69]. Typically, Ga$^+$ FIBID W-C deposits exhibit an atomic content of W between 40 and 50%, as well as significant fractions of C (30-40%) and Ga (10-20%), implanted during the irradiation.

The most noteworthy feature of this material is the occurrence of superconductivity below a critical temperature T_c between 4 and 5 K. In pure, crystalline W, superconductivity does occur as well, but the transition is located at much lower temperatures, in the vicinity of 15 mK [70]. The (upper) critical magnetic field[1], B_{c2} is typically reported within the 7 to 8.5 T range [42, 71, 72] at working temperatures of 2 K, and extrapolated to zero temperature to values of around 9.5 T [62]. The critical current density strongly depends on the geometry of the device, and as such, significantly differs between reports. A somewhat crude expected range is 0.01-0.1 MA/cm^2 [42, 62, 64, 65, 73]. Last, the two characteristic superconducting lengths, λ and ξ, take values of around 850 and 6.5 nm, respectively[2].

---

[1] In the context of the present thesis, the value of the lower critical magnetic field cannot be determined by means of magneto-transport measurements only. Doing so would either require performing extremely fine resistivity measurements to account for the appearance of the first vortices, or using a different technique, as STM. A basic approach to the latter is presented in section 3.4.

[2] As it will be discussed later, modulations in the superconducting behavior related to size effects start to take relevance when at least one characteristic length of the nanostructure (*i.e.*, width, or thickness) is comparable to the value of ξ. The low magnitude of this parameter in Ga$^+$ FIBID W-C makes inducing these size effects based on geometry only quite challenging.

The actual origin of the superconducting behavior in the W-C material is, at the time of writing, somewhat controversial and still a matter of debate. Early reports like that of Sadki *et al.* [62] relate the increase in T_c when compared to pure W to the amorphous structure of the material as well as to the presence of C and Ga impurities, both lacking in pure W single-crystals. However, as it will be mentioned later, it has also been reported W-C deposits grown by He^+ FIBID exhibit a crystalline structure and are still superconducting [74], indicating that, at least, the lack of crystallinity cannot be the *sole* reason for the superconducting behavior. Indeed, other factors altering the value of T_c must also be taken into account, including the electron-phonon interaction described in the BCS theory, and the subsequent changes therein when switching from a crystalline to an amorphous material. In addition, the amount of impurities introduced by the growth procedure can also modify the crystalline phase of the material, further altering the superconducting behavior.

Paramountly for the purposes of the present thesis and as aforementioned in Chapter 1, the Ga^+ FIBID-grown W-C is a type-II superconducting material, exhibiting an Abrikosov vortex lattice when subjected to an externally applied magnetic field [73]. The presence of this lattice has been directly evidenced by STM imaging [58, 73, 75], as it will be presented in section 3.4. Remarkably, narrow ($\sim$ 50 nm-wide) W-C nanowires grown by this procedure show a magnetic field-induced reentrance to the superconducting state [68]. Increasing the magnetic field would in principle drive the nanowire to the normal state in a sharp transition as the B_{c2} value is reached, but instead, the resistivity presents a non-monotonical dependence with the field: it first increases at the onset of the transition, then decreases returning to the superconducting state, and finally increases again up to its normal value. This phenomenon is accounted for by considering that in such a narrow nanostructure, the vortex "lattice" becomes a single line of vortices hosted within the axis of the nanowire, confined between two potential walls. Recalling that the Lorentz force induced by the driving current pushes the vortices *sideways*, *i.e.*, in a direction that is both perpendicular to the driving current and to the magnetic field, within a certain range of values of magnetic field, is energetically unfavorable for the vortices to pierce through the potential walls, and they remain confined. As a consequence, the driving supercurrent flows through the superconducting sides and vortices do not move, hence a zero-resistance is retrieved. This phenomenon does not happen in wider nanowires, since if multiple vortex rows are hosted in the nanostructure, there is room for motion and vortices still move. As such, this report also indicates that in principle, 50 nm-wide Ga^+ FIBID host a single row of vortices, which will be of use in the study of long range non-local vortex transport (section 3.3).

3.2 Growth and local characterization

3.2.1 Growth protocol

The growth of the samples was performed via conventional FIBID in the Thermo Fisher *Helios 600 Dual Beam* instrument. $W(CO)_6$ kept at a reservoir at 55°C was used as a precursor. In all cases, an acceleration voltage of 30 kV, and a previously optimized volume per dose of $8.3 \cdot 10^{-2}$ $\mu m^3/nC$, were used.

Both the non-local vortex transport and field effect experiments required the nanowires to have a relatively reduced lateral size (around 50 nm), and as such, the lowest available ion beam current in the instrument was used to perform the deposition. Si chips with a thermally-grown, 300 nm-thick SiO_2 layer were used as substrates. These chips also had sets of pre-lithographied Ti pads, used as a bridge to achieve electrical contact between the nanostructures and the instrumentation used to carry out the electrical measurements.

Samples were patterned as straight channels with two perpendiculars leads for voltage and current with line width of 50 nm (Figure 3.1).

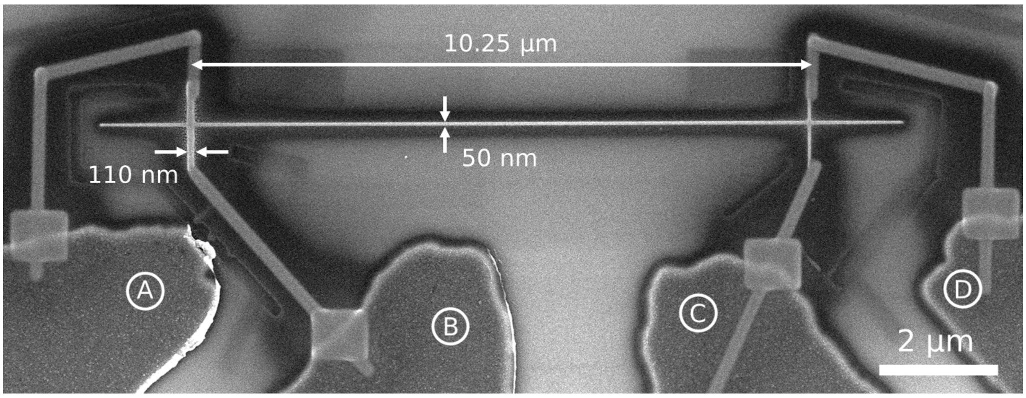

FIGURE 3.1: SEM image of the W-C nanostructure used for non-local vortex transport experiments. In a non-local measurement, the driving current flows from electrode B to electrode A, and the voltage is measured between electrodes C and D.

Although always of importance in all FIBID procedures, the focus quality and lack of aberrations in the FIB were rather critical in the patterning of 50 nm-wide nanostructures, since minimal deviations from an optimized beam resulted in drastic quality decreases in the deposit. Auxiliary alignment marks milled by the FIB near the deposition points were used in most cases.

Samples for STM experiments demanded a significantly different approach due to the very different requirements of the technique. Obtaining a sample suitable for both instruments was a first challenge *per se*, the details of which are presented in section 3.4. The actual sample was as 100 × 100 μm film grown on a Si substrate.

Such a dramatic increase in size called for an adjustment of the operating parameters, which, for the purposes of this sample, were modified to an ion beam current of 3.7 nA, and values of the X and Y pitch of 50 and 300 nm, respectively[3]. With a dwell time of 200 ns and the optimized value of the ion dose, the deposition time amounted to 24 minutes.

3.2.2 Compositional and structural characterization

As presented in section 3.1, growth of W-C via FIBID is already a solidly established application of this procedure and several reports on the composition and microstructure of the material are readily available (Table 3.1). In the context of the present work, conventional TEM studies were carried out on some of the samples, to double-check the actual properties of the deposits with those in the literature.

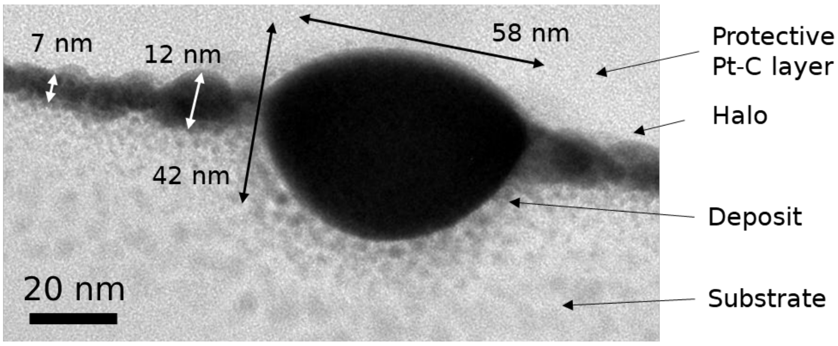

FIGURE 3.2: HRTEM image of a (nominally) 50 nm-wide representative W-C nanowire. Damage amorphization and substrate milling induced by the FIB are visible.

The samples exhibited thicknesses near 40 nm. In contrast to SEM inspection, TEM images reveal slightly larger line width values, falling in the 50-60 nm range (Figure 3.2). As analyzed by EDS, the metallic content moderately varies within different samples, with most samples exhibiting roughly 30% and 50% of atomic W and C, respectively. Implanted Ga and residual O account for the rest of the composition. The amount of C is also more prominent the further the analysis is performed from the center of the nanostructure (Figure 3.3).

The nanowires also exhibit a halo, of a maximum thickness of 10 nm (near the nanostructure, and decreasing outwards), mostly constituted by carbon. It most likely appears as a SE-II-induced by-product during deposition, but due to its reduced thickness and lack of metallic content, it will exhibit a significantly higher resistivity than the main nanostructure, and as such, it should not influence the electrical measurements to a significant extent, since the current will flow through the less electrically-resistive path.

---

[3] It should be noted that, as defined by the spot size of this current (50 nm), a pitch of 300 nm corresponds to no overlap at all (-200%). Reduced values of pitch yielded highly irregular surfaces, unsuitable for the needs of the STM experiments.

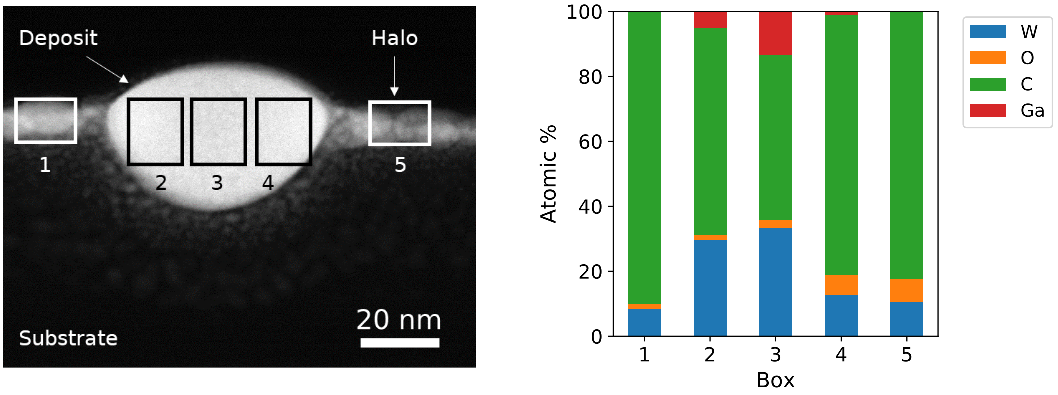

(A) STEM-HAADF image.

(B) EDS quantification of the boxes in the previous image.

FIGURE 3.3: TEM-based compositional characterization of a (nominally) 50 nm-wide representative W-C nanowire.

The core of the nanostructure is too dense to properly assess the presence of crystallinity (or lack thereof). On the halo, short-range order in the form of crystalline nanograins (2-3 nm in size), although the composition of these (80% and more of atomic C) is significantly different to that in the core.

3.2.3 Local electrical characterization

There is not much left to add on the local superconducting properties of W-C Ga$^+$ FIBID nanostructures to what has already been reported. A small variability in the parameter values between different samples, justified by the presence of imperfections in the nanostructure, does exist, but the general trend is in good agreement with the results reported in the literature. In this section, typical results extracted in the local configuration (Figure 2.11a) from representative 50 nm-wide nanowires are presented.

The room-temperature resistivity of the nanowires varies between samples, but is always contained in the 170-300 $\mu\Omega\cdot$ cm range. Samples exhibit a relatively sharp transition to the superconducting state at $T_c \sim 4.5$ K (Figure 3.4), with an amplitude not greater than $\Delta = 0.25$ K in the vast majority of cases. The critical current density, J_c, shows greater variability between different samples, but in most cases falls within the 0.1-0.2 MA/cm^2 range.

The occurrence of the magnetic field-induced superconducting transition strongly depends on the value of the driving current: with the superconducting state simultaneously bound by temperature, driving current, and current density (Figure 1.5), increasing the value of one parameter reduces the critical value of the other two. In this case, increasing the driving current (while keeping the temperature constant) reduces the magnetic field value at which the nanowire becomes normal (Figure 3.5a).

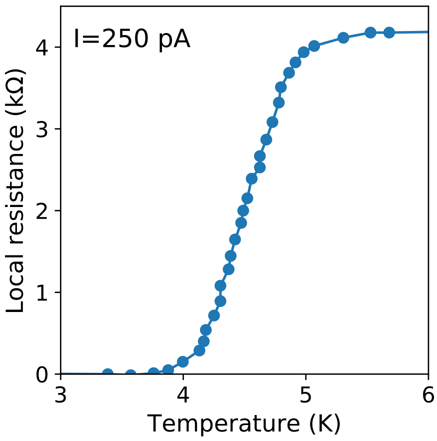

FIGURE 3.4: Temperature-induced superconducting transition in a 50 nm-wide nanowire. The solid line is a guide to the eye.

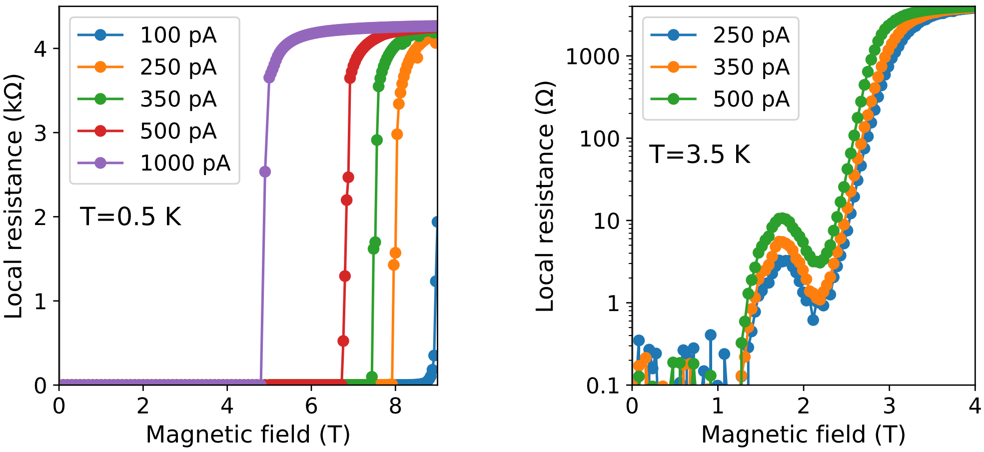

(A) Field-induced superconducting transition. (B) Superconductivity re-entrance (log scale).

FIGURE 3.5: Local magneto-resistance curves of a Ga^+ FIBID W-C nanowire, at low temperature and close to T_c. Solid lines are a guide to the eye.

The expected superconductivity re-entrance [68] is detected at 3.5 K, reasonably close to T_c (Figure 3.5b). A full re-entrance is not achieved, with the resistance dropping down to 1 Ω, most likely due to the used driving currents being relatively high.

The "nominal" magnitude of B_{c2}, *i.e.*, its projected value at theoretical values of zero temperature and zero current, is extracted by fitting both the temperature and current to expected trends, and then extrapolating the value according to said trend. The critical field is expected to depend on the temperature [25] as per

$$B_{c2}(T) = B_{c2}(0)\left[1 - \left(\frac{T}{T_c}\right)^2\right], \tag{3.1}$$

with experimental data being in good agreement with this trend (Figure 3.6a). The values of B_{c2} at zero temperature for each driving current I are extrapolated through this fit, and then these were empirically fit to a $I^{2/3}$ dependence (Figure 3.6b). The final projected value of B_{c2} for $I = 0$ and $T = 0$ is of 10.9 T, reasonably close (if slightly above) to the values reported in the literature (typically around 9.5 T).

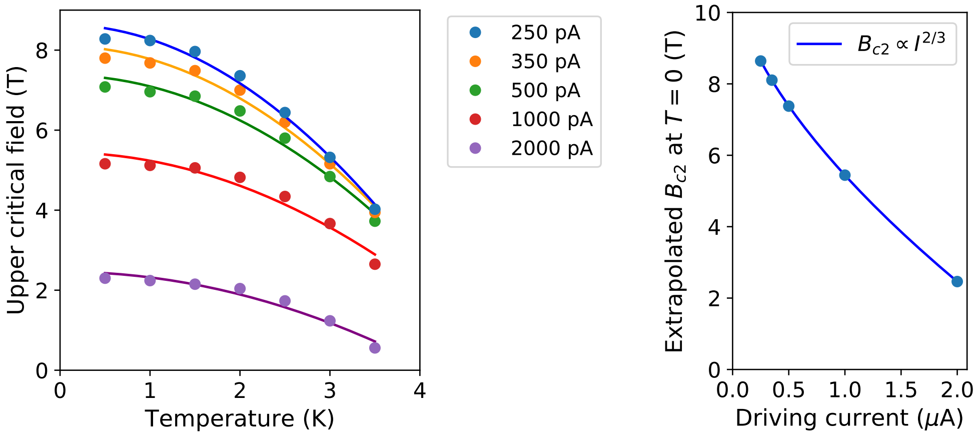

(A) Critical field temperature dependence. Solid lines are a fit to equation 3.1.

(B) Fit for $I = 0$ extrapolation.

FIGURE 3.6: Upper critical field characterization.

Taking these results into account, the coherence length and penetration depth can be respectively estimated from equations 1.7 and 1.8, and yield average values of $\xi \sim 5.5$ nm and $\lambda \sim 750$ nm, also in agreement with the reported values.

3.3 Long-range non-local vortex transport

3.3.1 Experimental results and discussion

As aforementioned, the quantized nature of superconducting vortices makes them likeable candidates for the transport of single "bits" of information in the design of superconducting nanodevices. In this section, an experimental study in long-range vortex transport in Ga$^+$ W-C nanowires is presented. Although self-contained, it represents a piece in a larger research labor concerning non-local vortex transport in Ga$^+$ FIBID W-C nanowires, published by Córdoba *et al.* in 2019 [76].

The main motivation for this study was related to the fact that while previous results had shown the capability of Ga$^+$ FIBID W-C to sustain this kind of non-local vortex motion [42], the scope of the effect had not been fully explored. These initial results indicated that wide (∼200 nm) nanowires did present this effect, reaching non-local voltages of around 0.2 Ω.

To further investigate this phenomenon, additional experiments were designed and performed, namely putting the persistence of the effect to the test in narrower and longer nanostructures. 3 μm-long, 50 nm-wide nanowires presented a strong signal associated to nonlocal vortex transport, with non-local resistances up to 35 Ω in value, two orders of magnitude above their 200 nm-wide counterparts. Having established that narrower nanowires favored a more efficient vortex transport, it remained to investigate how far this motion could propagate, for which the following experiment was devised and performed.

The experimental setup used to probe the non-local vortex-carrying capability of a type-II superconductor, initially proposed by Grigorieva *et al.* and studied in MoGe films [44], has been already presented in sections 1.3.5 and 2.3.3. A completely equivalent approach is taken here (Figure 2.11b).

The nanostructures are patterned as a long, straight channel with two perpendicular leads at each end (Figure 3.1). The channel measures 10.25 μm in length between the two contacts, and has a width of 50 nm. The lead through which the driving current is intended to be injected is grown with a width of 110 nm, greater than that of the rest of the nanostructure, for it to be capable of sustaining high current values before it transits to the normal state. The length of the channel is three orders of magnitude greater than the inter-vortex separation at the working values of applied magnetic field (equation 1.6), which falls in the range of tens of nanometers. The channel length also ensures that any remnants of the driving current flowing through the voltage lead are completely negligible. As such, the voltage lead can be safely considered depleted of current at all times.

The non-local magneto-resistance dependence of the sample presents a monotonic increase in resistivity with increasing magnetic field starting at a certain threshold, peaking at absolute values of resistance as high as 8 Ω. It then monotonically decreases when the magnetic field is further increased (Figure 3.7).

The appearance of finite values of resistance in a region of the nanowire completely depleted of driving current is attributed to the non-local transport of superconducting vortices, driven by the Lorentz force provided by the driving current injected at the other end.

When the width of the channel is greater than ξ but of falls within its order of magnitude, (*i.e.*, when it is comparable to the "lateral size" of a vortex), for values of magnetic field above its crossover value (from bulk to surface superconductivity, when vortices are allowed to enter the nanowire), the energetically favorable arrangement of the vortices is that of a single row, disposed along the center of the nanowire and enclosed by superconducting edges [68]. In turn, the edges act as potential barriers for the vortices, preventing them from entering or leaving the nanowire at the

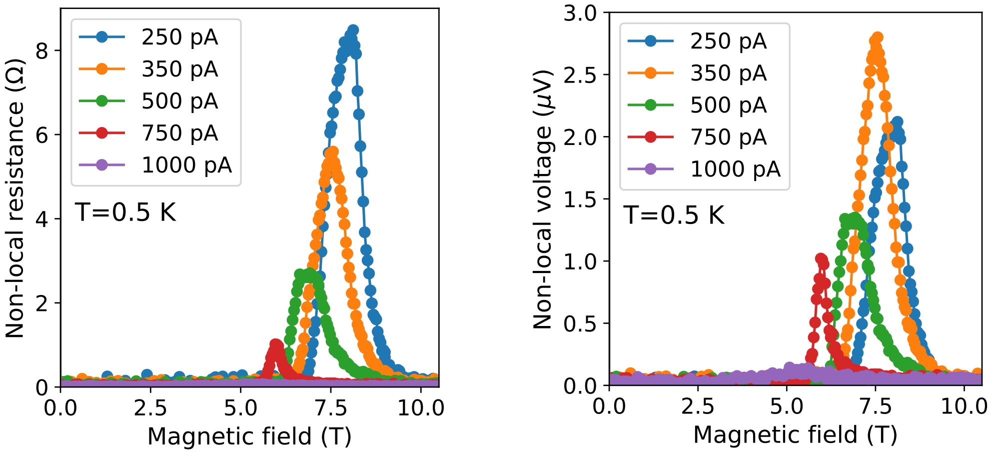

(A) Non-local resistance.

(B) Non-local voltage.

FIGURE 3.7: Non-local magneto-resistance in a 10 μm-long W-C nanowire. The detected resistances are solely generated by passing vortices.

sides, and thus restricting the motion to the longitudinal direction. In the case of W-C nanowires, they are reported to host a single row of vortices when they are patterned with widths below 70 nm, in agreement with the expected values of ξ for this material [68, 77, 78].

Considering a fixed value of driving current (an individual curve in Figure 3.7), at zero and very low values of magnetic field, vortices are simply not present within the nanostructure, and as such, the non-local signal is evidently zero, since no driving current flows through the voltage lead. Further increasing the field (while keeping the driving current constant) results in the apparition of (few) vortices within the nanostructure, which are positioned at the energetically favorable locations, corresponding with sites where the intrinsic pinning of the material is maximum. At this point, the pinning force effectively nullifies the push or pull exerted on the vortices by the (constant) Lorentz force, and the non-local signal remains zero, even when vortices are present within the nanostructure.

As the magnetic field is increased, so does the vortex density within the material, resulting in a saturation of the vortex pinning sites. At that point, intrinsic pinning can no longer hold the now-numerous amount of vortices in place against the Lorentz force, and they start to move along the longitudinal axis of the nanostructure. The potential barriers at the edges hamper any lateral displacements, resulting in an ordered motion along the axis. As vortices cross through the voltage lead, the electrical field they generate as they move (equation 1.9) is detected in the voltage lead in the form of a non-zero non-local signal.

Further increasing the field results in more vortices passing through the voltage lead, with an associated voltage increase, which manifests itself in the monotonic increase in the signal after the onset of motion occurs. However, further increasing the field leads to the (fixed) driving current value reaching its critical value at that field, $J_c(B)$. When that happens, vortices present in the current lead pierce the potential walls on one side and enter through at the other, resulting in the appearance of dissipation in the lead, and a significant loss of effectiveness in pressure transfer towards the channel. As a consequence, the non-local signal decreases.

Driving the field to even higher value does amplify this effect, driving the whole current lead to the normal state, and further reducing the efficiency of vortex push. The non-local signal continues to decrease down to zero. At higher values of magnetic field, the whole nanowire returns to the normal state as the critical value of the field is reached (B_{c2}), even in the areas depleted of current, and the non-local signal remains zero.

The same argument holds for different values of driving current. Higher values result in a greater magnitude of the Lorentz force against pinning, with an associated "earlier" onset of vortex motion, but also drive the nanowire to the normal state "earlier", in terms of magnetic field intensity. Conversely, the phenomenon can also be evaluated by keeping the magnetic field constant and increasing the driving current, with the principles remaining the same - a competition between the Lorentz force and intrinsic pinning. The higher the current and the field, the higher the Lorentz force and the "lower" the pinning, respectively.

3.3.2 Numerical simulations

To gain further insight on the mechanisms of non-local vortex transport, numerical simulations based on the Ginzburg-Landau theory were performed in a scientific collaboration with Ž. Jelić and M. Milošević., researchers from the University of Antwerp. Details on the theory these simulations are based on, the *Time-Dependent Ginzburg Landau* framework (TDGL), are outside the scope of this thesis, and can be found elsewhere [79, 80], while the specifics of the simulations performed here can be retrieved from the corresponding article [76]. The results are, however, quite intuitive, and are presented here for illustrative purposes.

The simulations were carried out utilizing the temperature of the experiments, and defining a nanostructure geometry comparable to its real counterpart, with a channel and lead width of 50 nm, and a channel length of 1.16 μm. Vortex sites can be directly visualized in the form of Cooper pair density (CPD) maps, which color-code the n_s parameter, allowing to differentiate the normal cores of the vortices from the superconducting bulk. In the simulation, the potential barriers at the ends of the nanostructure were lowered, accounting for a "tip effect" in the nanodeposition procedure - the Gaussian shape of the FIB spot results in a smooth thickness decay near the edges of the nanowire.

The simulated dependence of the non-local voltage with the applied magnetic field (Figure 3.8a) is in quantitatively good agreement with the experimentally retrieved data. The maximum in non-local voltage is achieved at the value of magnetic field (close to its critical value) that can host the most vortices within the channel without driving the nanowire to the normal state. Conversely, modifying the driving current while keeping the magnetic field (*i.e.*, the number of vortices) constant yields comparable results (Figure 3.8b), where the maximum in non-local voltage corresponds to the most current the lead can withstand without going normal, so the force exerted on the vortices is maximum.

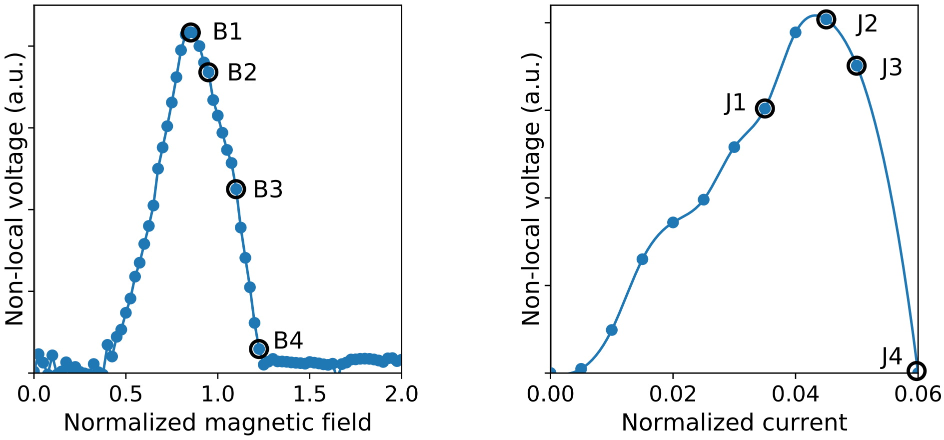

(A) Magnetic field dependence.

(B) Current density dependence.

FIGURE 3.8: TDGL simulations of the non-local voltage yielded by passing vortices as a function of the magnetic field and the driving current. Both parameters are represented normalized to nominal values defined in the TDGL framework [76]. CPD maps at the labeled points, B1-4, and J1-4, are shown in figures 3.9a and 3.9b, respectively.

From the CPD maps (Figure 3.9), it can be seen that, as expected, the current lead is driven to the normal state "earlier" than the rest of the nanostructure, since it is the only area where the current (which, in addition to the action of the magnetic field, further pushes the superconductor to the normal state) actually flows[4].

The simulation tool was also exploited to estimate the potential extent of the effect. To do so, using the same geometry, the following experiment was simulated: after recording the initial positions of the vortices in absence of current, a long, finite current pulse was applied to the current lead. The positions of the same vortices

---

[4] Deformation effects on the row can also be observed, either in the form of a zigzag pattern or in an accordion-like compression towards the center of the channel. These are, to an extent, artifact-like byproducts of the TDGL simulations - the (simulated) sharp corners at the crossing point of the current lead with the main channel create effective barrier walls which compress and distort the lattice, which alter the way the lattice appears within. The lattice compression can also be accounted for by the decay in momentum transfer along the main channel of the nanowire. In any case, these geometrical features are not the object of the simulation and their interpretation should be taken with care.

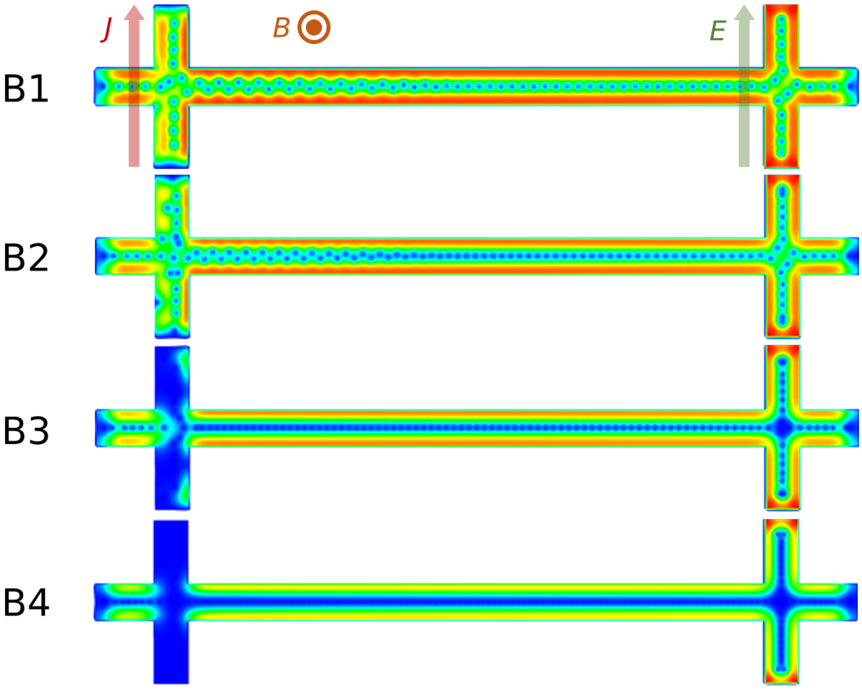

(A) CPD snapshots at the indicated points in the simulated field sweep of Figure 3.8a.

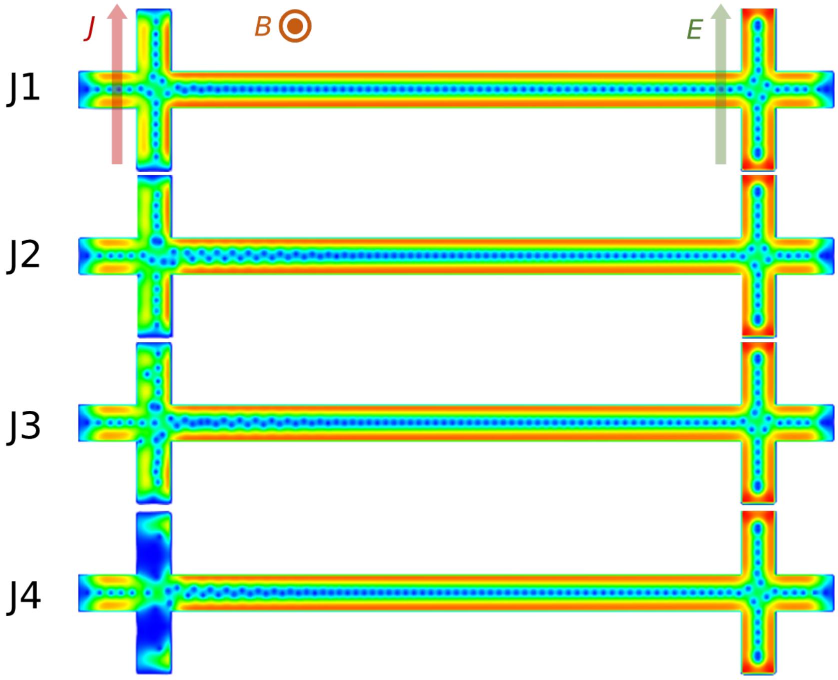

(B) CPD snapshots at the indicated points in the simulated driving current density sweep of Figure 3.8b.

FIGURE 3.9: CPD maps of the field and driving current sweeps of Figure 3.8. Color differences indicate changes in the value of n_s at each point, with red and warm tones indicating superconductivity ($n_s = 1$), and blue and cold tones indicating normal state ($n_s = 0$). The vortices appear as dark blue spots, confined between two superconducting walls at the edges of the nanostructure.

were recorded again. These individual *vortex displacements* were found to depend on the distance to the current injection point (Figure 3.10).

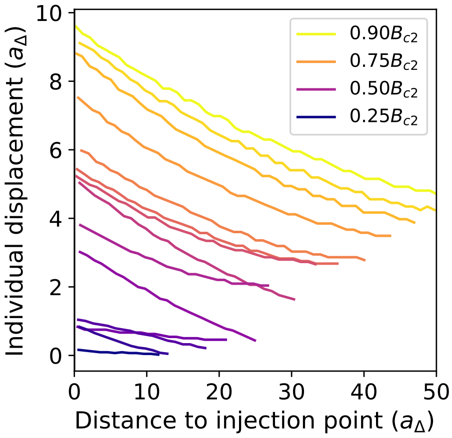

FIGURE 3.10: Vortex displacements as a function of distance to the current injection points. Both axes are indicated in terms of the inter-vortex separation, $a_\triangle$. Consecutive lines are $0.05B_{c2}$ apart.

To consider that proper "motion" occurs, vortices should travel at least one full inter-vortex distance ($a_\triangle = 1$), otherwise, their motion can be simply considered as a perturbation surrounding their equilibrium positions. As such, the propagation extends until the displacement reaches 1 or less. As the field is increased, the vortex displacements follow a saturation-like trend that extends over large distances, implying that the maximum distance vortices is, in principle, orders of magnitude greater than the inter-vortex distance. While this "experiment" is a simplified version of reality (for instance, it does not take pinning into account), it still provides with an intuitive view of the long-range capabilities of vortex transport in this manner.

3.4 Vortex lattice imaging

Up to this point, only experiments concerning resistance measurements of superconducting nanowires have been presented. The scientific potential of vortices in the W-C material is not restricted to these kind of observations. STM-based studies of the dynamics of the Abrikosov lattice, including its melting and the forcing of modulation-induced correlations are a prime example [58, 59, 73, 81].

As such, STM investigation of Ga$^+$ FIBID W-C is an already laid and well-defined path, yet one that can still be further extended. While the focus of the present thesis is the aforementioned investigation of electrical properties in superconducting nanowires, this section presents the first steps taken in scientific collaboration with A. Domínguez and D. Serrate, from the INMA (CSIC-University of Zaragoza), consisting in the development of a protocol of Ga$^+$ FIBID fabrication of samples destined for STM investigation. The first proofs-of-concept are also presented here, which include STS imaging of the Abrikosov lattice. These two efforts set the grounds for subsequent STM-based experiments, for both the sample preparation procedure and experimental realization proved successful.

As presented in section 1.3.2, one of the electrical signatures of a superconducting material is the presence of a finite gap in its density of electronic states, representing an energy range on which individual, unpaired electrons are not allowed to exist. In STM operation (section 2.4.1), the sample and the tip are counter-biased at a voltage V_b, so that a tunneling current I_t (of individual, unpaired electrons) flows between the two. As such, a $I_t - V_b$ characteristic is retrieved between the two, with the remarkable property that the variation of I_t with V_b, dI_t/dV_b, or *conductance*, is proportional to the local density of states at the point that is being probed [60].

Therefore, scanning the surface of a superconducting material and performing STS therein allows for imaging of the Abrikosov vortex lattice - as the cores of the vortices are normal, for $|V_g| < \Delta$, no current is expected to flow between the sample and the tip (*i.e.*, $dI_t/dV_b = 0$ until $|V_g| \geq \Delta$), since there are no available electronic states for unpaired electrons within the superconducting gap. Mapping the retrieved values of conductance over an area of the sample thus enables to visualize the vortex lattice in the material, with the image contrast representing the presence of superconductivity, or lack thereof in vortex sites.

In the context of this thesis, carrying out the experiment posed the additional challenge of preparing a sample that was simultaneously suitable for both the FIB/SEM instrument and the STM equipment. The following sections summarize the sample preparation procedure, and the experimental results retrieved.

3.4.1 Sample preparation

In the SPECS *Joule-Thomson* STM instrument used to carry out these experiments, sample positioning is performed manually via visual inspection of an optically magnified image. When dealing with "large" films that reach spans of millimeters, it does not represent a significant drawback, however, manually locating a μm-sized feature ranges from challenging to virtually impossible. As such, the main obstacle faced when designing the experiments was to obtain a sample large enough so it could be located by visual inspection in the STM instrument, but small enough to not exceed the range of applicability of FIBID. In addition, since in STM inspection a current is continuously being delivered to the sample, electrical discharging is required, and as such, the insulating SiO_2 substrates are not suited for this purpose.

With both objectives in mind, a substrate-sample arrangement was designed. A reasonable middle ground in the size sample issue was achieved with sample sizes of 100×100 μm (Figure 3.11), the deposition parameters of which can be found in section 3.2.1. SEM inspection revealed a reasonably flat surface, and its thickness, assessed via FIB/SEM cross-sectioning, was found to take values of ~ 50 nm.

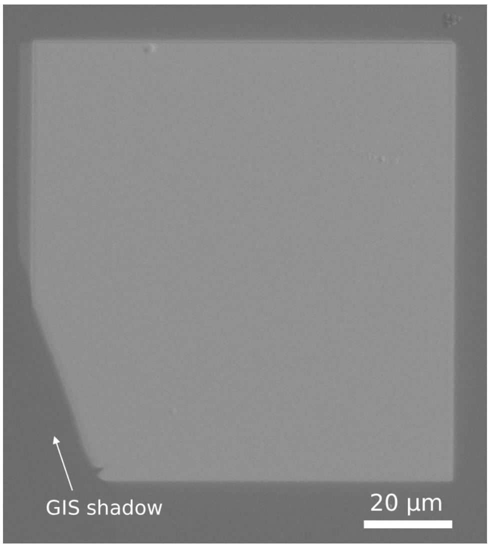

FIGURE 3.11: SEM image of W-C film. A GIS nozzle "shadow" is visible on the lower left corner of the sample. This effect was removed in the final sample by positioning the pattern away from the center of the field of view.

As a substrate, a 5 × 5 mm Si piece with a native SiO_2 layer on top was used. To fulfill the aforementioned need for charge discharging, a 50 nm-thick layer of Au was evaporated on top of the substrate. Prior to evaporation, a wire with a diameter of 100 μm was placed between two opposite corners of the substrate, to act as a somewhat rudimentary "mask" in the Au evaporation process (Figure 3.12).

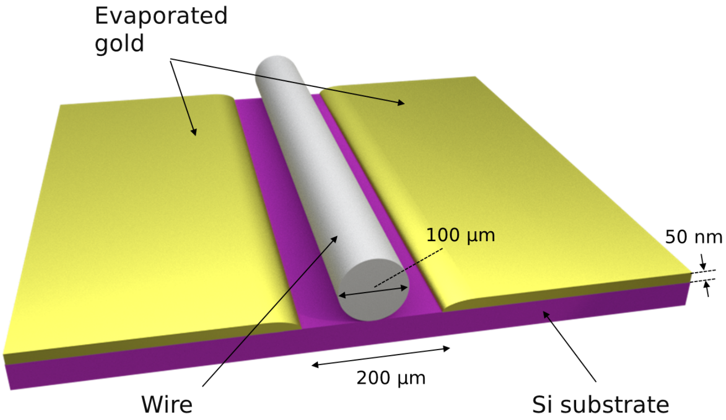

FIGURE 3.12: Scheme of the evaporation procedure for the fabrication of the substrates. The wire acts as a mask, yielding an uncoated trench beneath. Not to scale.

The presence of the wire yields a roughly 200 μm-wide Si/SiO_2 trench that separates the two Au-coated regions in the chip (Figure 3.13a). To further ease sample positioning in the instrument, Au from four additional 400 × 200 μm areas was milled away via FIB exposure (with an ion beam current of 21 nA) near the center of the

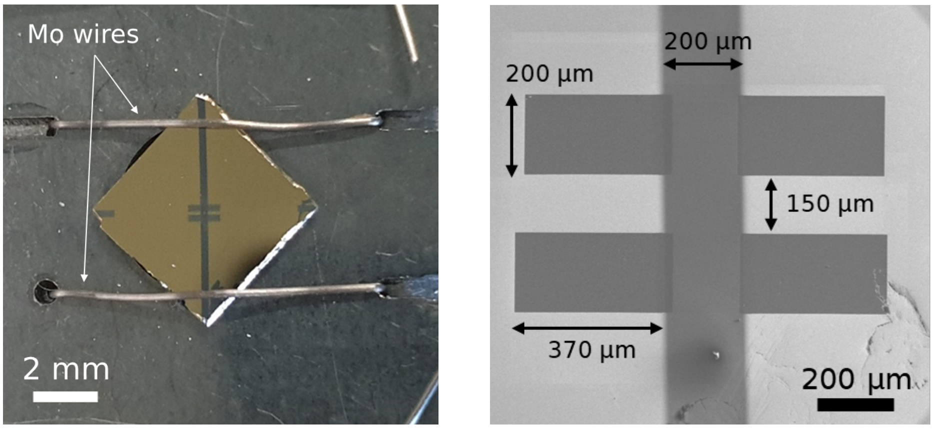

(A) Mounted sample.

(B) SEM image of the sample growth location.

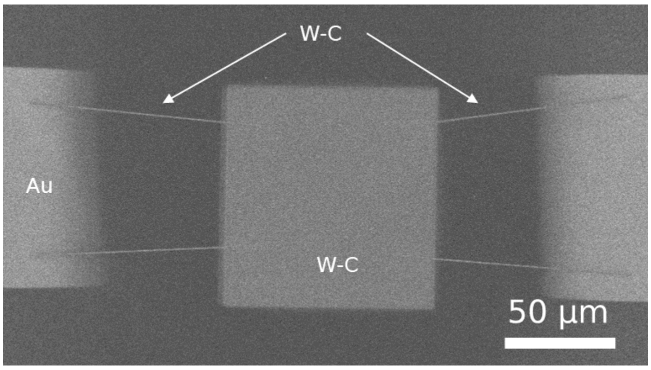

(C) The film in position, joined to the evaporated gold by Ga^+ FIBID W-C nanowires.

FIGURE 3.13: SEM images of the sample used for STM experiments, presented in increasing order of magnification.

trench. Adjacent areas were separated 100 μm one from the other, so that the sample could be placed in between the two in the trench (Figure 3.13b).. The film was then joined to the Au "electrodes" via FIBID of long, nanowire-like contacts using an ion beam current of 48 pA, with nominal width and thickness of 400 and 30 nm, respectively (Figure 3.13c).

The resulting disposition is visible to the naked eye and proved sufficient for sample positioning (Figure 3.14). This simple, yet effective procedure can be easily reproduced for further studies that require connecting the two seemingly distant fabrication and characterization techniques of FIB/SEM nanofabrication and STM analysis.

3.4.2 Experimental results

Topographic analysis of the surface via STM imaging revealed the presence of numerous nm-sized grains on top of the film (Figure 3.15a), not detected via SEM inspections. While these grains do not completely hinder the experiment, they do pose a significant issue, as the tip drags them during scanning. Grains sticking to the tip

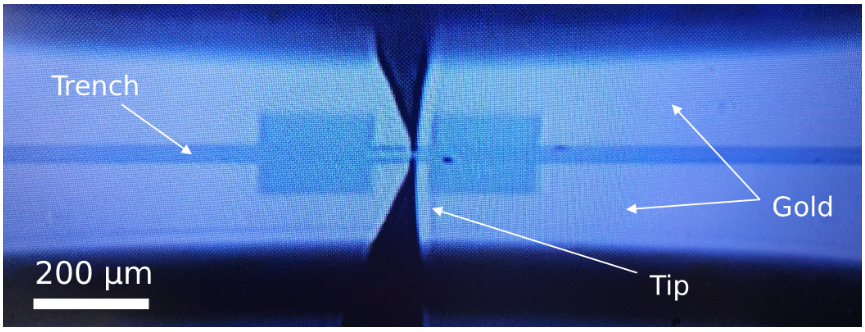

FIGURE 3.14: Optical image showing the STM tip located under the sample, positioned using the FIB-milled trenches. The tip is approximated to the sample from below, and its reflection is visible on top.

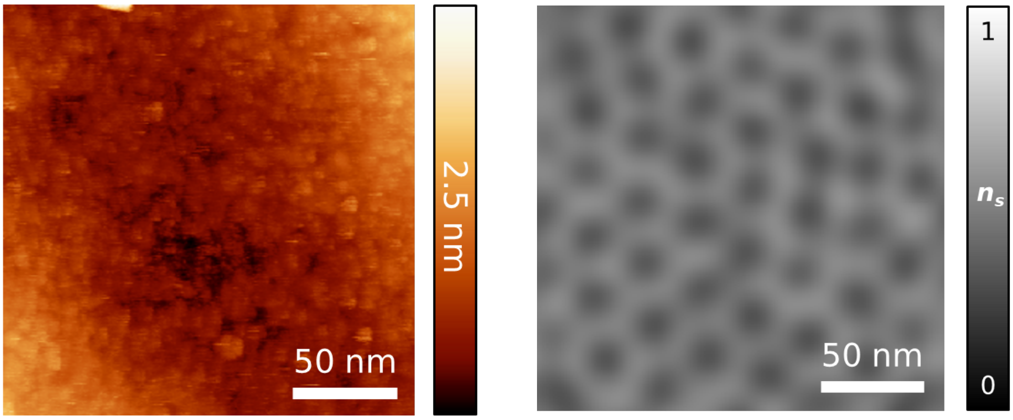

(A) Topography.

(B) STS image. Each dark spot corresponds to a superconducting vortex.

FIGURE 3.15: Topography and spectroscopy images of a region of the W-C film. $T = 1.2$ K, $B = 2.3$ T.

or moving around over the surface alter the nature of both the surface and the tip, leading to the formation of artifacts and the rise of instabilities[5].

The distribution of the density of superconducting carriers, n_s was mapped by STS, individually measuring the conductance, G, at zero[6] and high bias voltages at each spot, and then normalizing to its value at high bias, namely,

$$n_s \propto \frac{G(+3\text{mV})) - G(0)}{G(+3\text{mV})}. \tag{3.2}$$

In superconducting regions, the presence of the gap makes $G(0)$ take a zero value,

---

[5] Further discussing this issue would require an in-depth discussion on STM operation procedures, vastly exceeding the scope of this work. As such, it will not be presented here. It will suffice to say that the surface of the films was not as neat as one would like it to be, and as such, retrieving the images was far from trivial.

[6] It is worth remarking that what is measured in the experiment is the conductance G, and not the tunneling current I. While at zero voltage the tunneling current remains zero, the conductance (*i.e.*, the slope of the $V - I$ curve), can and does take other values.

and thus $n_s = 1$ (white contrast, superconductivity), while when the tip is positioned over a superconducting vortex, the value of G at zero voltage matches that at high voltages, and as such, $n_s = 0$ (black contrast, indicating the lack of superconductivity over the normal core of a vortex).

Representing a n_s contrast STS map unequivocally shows the Abrikosov vortex lattice in the film (Figure 3.15b). Vortices arrange hexagonally, with a lattice parameter of $a_\triangle = 29.8$ nm at 2.3 T, reasonably close to the expected value of 32.2 nm (equation 1.6). The dependence of the shape and magnitude of the superconducting gap with temperature and applied magnetic field was investigated as well (Figure 3.16), retrieving, at a fixed temperature of 1.2 K, values of 0.54 and 0.42 meV under applied fields of 0 and 2.3 T, respectively, also within the order of magnitude of the predicted zero-field BCS value of 0.68 meV (equation 1.1).

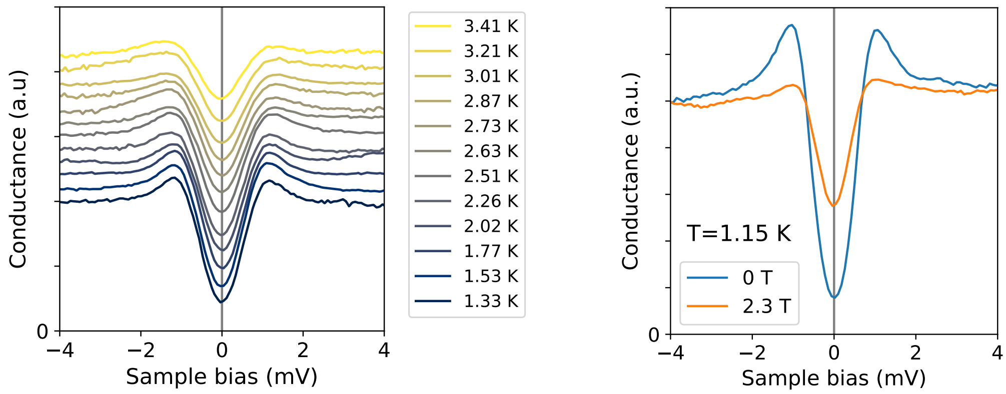

(A) Temperature dependence (offset applied between curves).

(B) Magnetic field dependence.

FIGURE 3.16: The superconducting gap, probed by STS. The conductance is normalized to its value at high bias voltage.

While not groundbreaking at all *per se*, this preliminary study provides with a reproducible procedure to link the FIB/SEM nanofabrication technique with characterization and processing via STM at the Laboratory for Advanced Microscopies, which is to be exploited in future works (Chapter 6). As such, the path towards collaborative STM investigation of Ga^+ FIBID W-C or any other FIBID material is significantly more clear, since adequate universal, substrates can now be easily produced, and a recipe for Ga^+ FIBID of W-C films has been optimized. With particular focus on the investigation of superconductivity, prospective experiments could include the study of how vortices interact with magnetic spins (placed by STM-positioning of magnetic Co atoms), aiming towards the detection of a nanoscale Bitter effect [82], or findings of Yu-Shiba-Rusinov states [83].

3.5 Field effect on narrow nanowires

The already-mentioned work performed by Paolucci *et al.* [49] served as a starting point to the experimental investigation of the tunability of the resistivity of Ga$^+$ FIBID W-C nanowires using a gate voltage, V_g. Local suppression of superconductivity induced by a gate voltage represents a powerful tool in the design of superconducting circuits, for it allows to include functional nanodevices in their architecture, like transistors, Josephson junctions[7], superconducting quantum interference devices (SQUIDs), etc. Such architectures can prove challenging in W-C, due to the reduced value of its coherence length.

As such, a proof-of-concept experiment was carried out, growing W-C nanowires by Ga$^+$ FIBID in Si/SiO$_2$ substrates with a set of Au nanocontacts pre-patterned by electron beam lithography. The operating parameters were set to the optimized values described in section 3.2.1, using an ion beam current of 1.5 pA, the optimized volume per dose of $8.2 \cdot 10^{-2}$ μm^3/nC, and a deposition time of around 15 seconds. In addition, a trench between the contacts was milled between the contacts also by FIB irradiation, using the same ion beam current in "reduced area" exposure mode (Figure 3.17).

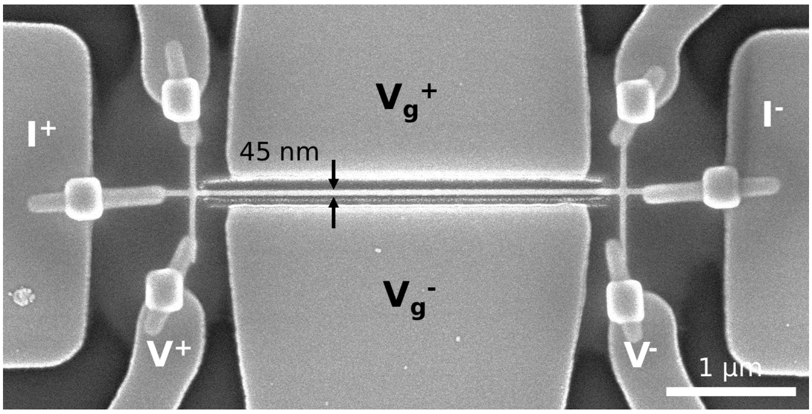

FIGURE 3.17: SEM image of a W-C nanowire used for the study of field effect. The driving current and voltage measurement points are indicated as I and V, and the gate electrodes are labeled as V_g.

The field-effect was assessed by measuring the resistance of the nanowire in the superconducting state (in DC mode), and sequentially applying a fixed value of gate voltage in the 0-4 V range. To account for hysteresis, each measurement was carried out in a looping fashion, increasing the driving current from 0 up to ± 3 μA, and then decreasing it down to 0 for both current signs (Figure 3.18). Contrary to most reported S-FET devices [84], no relevant thermal hysteresis was detected, suggesting the absence of significant thermal heating effects.

---

[7] Succinctly, a superconducting-normal-superconducting Josephson junction (sometimes called *weak link*) is a locally normal region sandwiched between two superconducting leads. When a supercurrent is made flow through the normal region (whose "normality" can be achieved by different means), interesting phenomena arise, which can be exploited for different purposes.

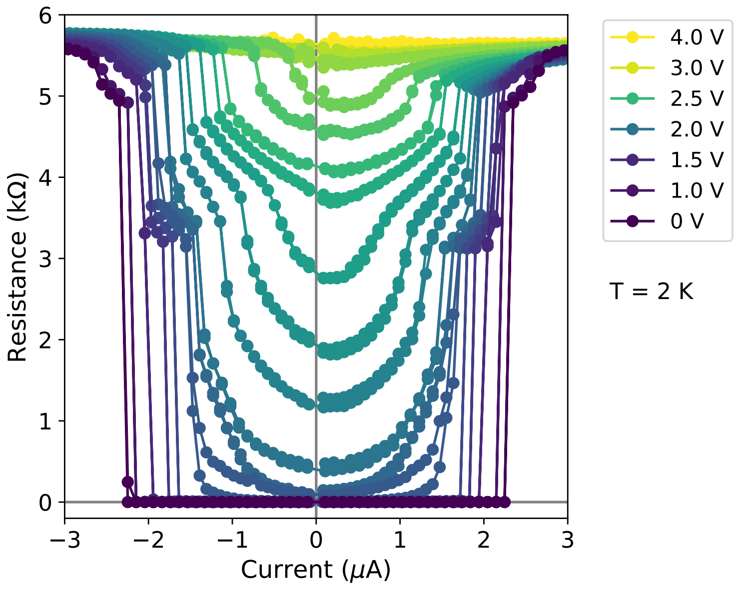

(A) Positive gate voltage.

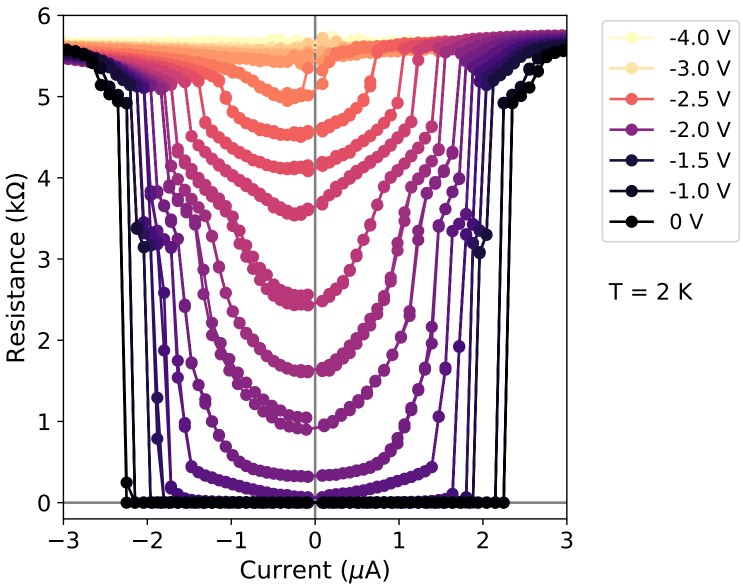

(B) Negative gate voltage.

FIGURE 3.18: Field effect at 2 K. Unlabeled curves (all between ±1.5 and ±4.0 V), are 0.1 V apart. Solid lines are a guide to the eye.

The critical current of the nanowires monotonically decreases with increasing V_g, and a fully normal state is retrieved for $V_g \geq 4$ V. A sign-dependent asymmetry manifests in one leg of the $I - V_g$ values when reversing the sign of I or of V_g, indicating a "favored" current-voltage sign combination, ascribed to the presence of a leakage current[8].

---

[8] The presence of polarized gate electrodes in close proximity to the main conducting channel induces the apparition of a *leakage current*, I_l, flowing from or towards them if the substrate separating

In addition, some $R - I$ curves present a step-like transition to the normal state, plausibly indicating the nanostructure is driven to it in the form of normal nucleations in local regions, instead of doing so sharply and as a whole[9]. Indeed, for $V_g > 2$ V, nonzero values of R are detected at $I \sim 0$, indicating that part of the nanostructure is already normal under these conditions. The most likely explanation is the occurrence of nanoscale inhomogeneities either in the superconducting nanowire or in the local electric field. Further increasing the voltage drives the nanostructure completely to the normal state (below T_c), as indicated before. Repeating this measurement at 3 and 4 K (Figures 3.19 and 3.20) shows that, as it is to be expected, the increased value of T weakens the device superconductivity, with all transitions being shifted towards lower values of I and V_g.

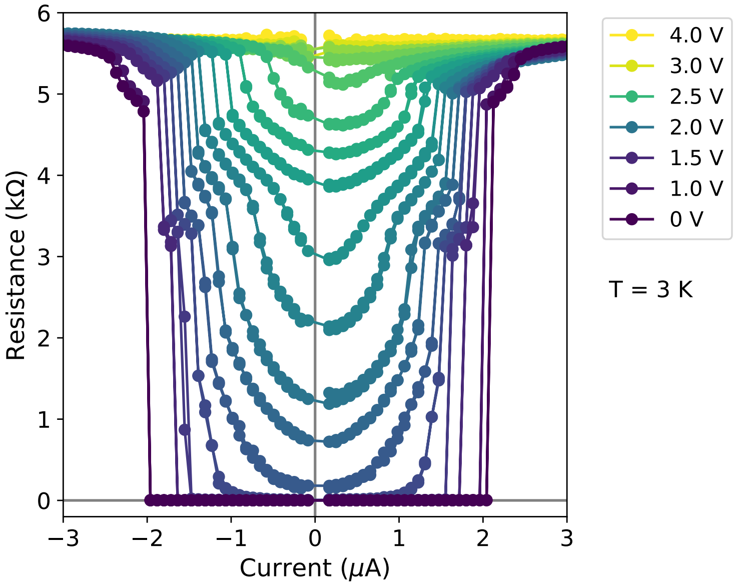

FIGURE 3.19: Field effect at 3 K. Unlabeled curves (all between 1.5 and 4.0 V), are 0.1 V apart. Solid lines are a guide to the eye.

De Simoni *et al.* [85] propose a model based on the Ginzburg-Landau formalism, on which the dependence of the critical current I_c with the gate voltage V_g is given by

$$I_c(T, V_g) = I_c^0 \left[1 - \left(\frac{T}{T_c}\right)^2\right]^{3/2} \left[1 - \left(\frac{V_g}{V_g^c}\right)^4\right]^{3/2}, \tag{3.3}$$

where I_c^0 is an extrapolated value of I_c at zero temperature and with no applied electric field, and V_g^c is the value of V_g at which the value of I_c is fully suppressed.

---

both is not completely insulating. In this case, I_l is estimated to not exceed 80 nA in the working range with $|V_g| \leq 4$ V, representing at most a 2.7% of the total injected current. Its presence does not hinder the occurrence nor the observation of the field effect in the superconducting nanodevices.

[9] It is worth recalling that since no magnetic field is applied in this experiments, vortices cannot play a role in these results - they are not present within the nanostructure.

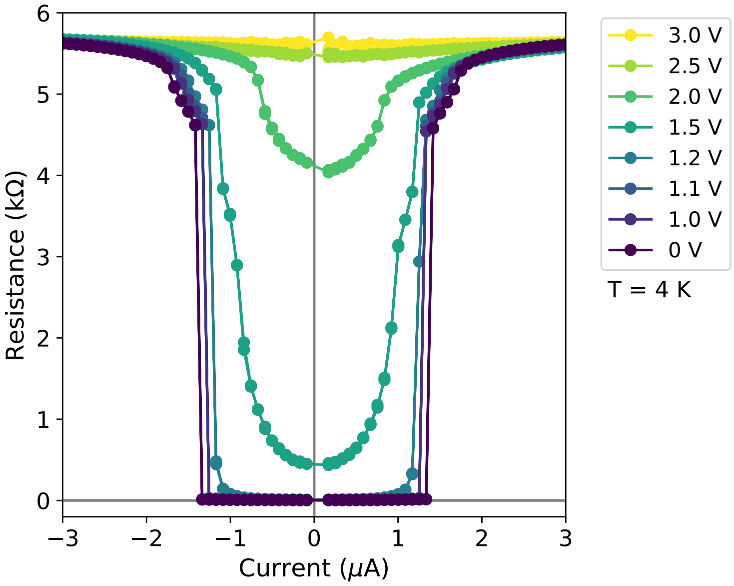

FIGURE 3.20: Field effect at 4 K. Solid lines are a guide to the eye.

In the absence of gate voltage ($V_g = 0$), the previous model does not account for the experimentally observed dependence of I_c with temperature: the nanodevice is capable of withstanding higher values of current at "high" temperatures below T_c than those indicated by the model. The narrow lateral size of the nanodevice can represent a plausible justification for this phenomenon, with finite size effects overcoming the general trend predicted by the model.

However, taking the first term as a constant of proportionality only, the $I_c - V_g$ data is in good agreement with the predicted dependence (Figure 3.21). The values of V_g^c retrieved from the fit are 3.0, 2.9, and 2.5 V at 2, 3, and 4 K, respectively.

The performance of field-effect-based transistor-like devices is typically assessed by means of several figures of merit, two of which are the *transconductance*, g_m, and the *kinetic inductance*, L_k [49]. The transconductance accounts for the variation of the critical current with the gate voltage, and it is calculated by taking the numerical derivative of the $I_c(V_g)$ dependence:

$$g_m \equiv \frac{dI_c}{dV_g}. \tag{3.4}$$

In the present nanodevice, g_m, calculated from the experimental data, is reasonably comparable to the experiments of Paolucci's Ti S-FET [49] in terms of both absolute values and general temperature trend (Figure 3.22a).

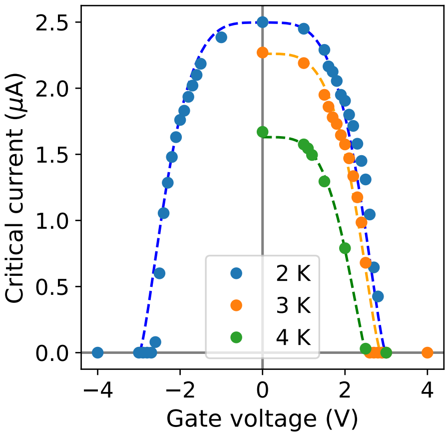

FIGURE 3.21: Dependence of the average absolute value of the critical current with the gate voltage. Dashed lines are a fit to equation 3.3.

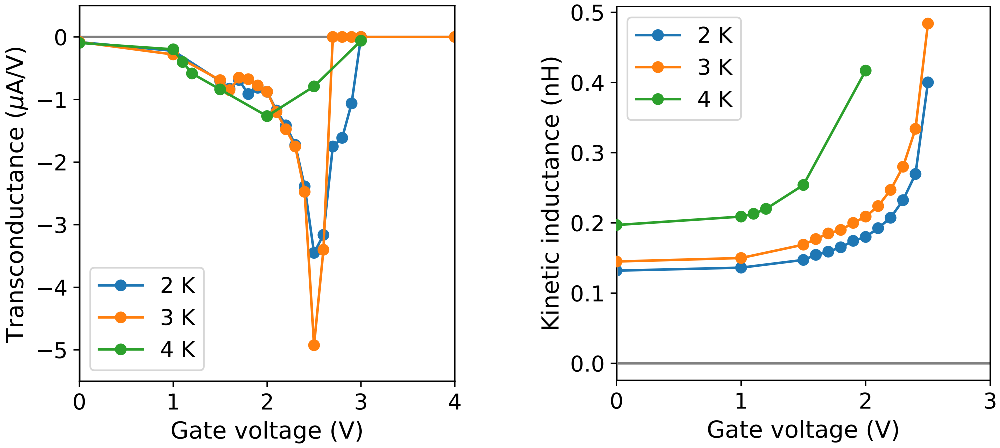

(A) Transconductance.

(B) Kinetic inductance.

FIGURE 3.22: Figures of merit in the study of field effect, calculated using the average of the absolute values of the critical current at positive and negative values of I_c, and averaging between positive and negative values of V_g at 2 K. Solid lines are a guide to the eye.

The maximum value of g_m is located around 5 μA/V, about half of the maximum value reached in said Ti S-FET, and three orders of magnitude above typical values of semiconductor-based field-effect transistors (in the order of nA/V, with V_g around tens of V [86]).

On the other hand, similar superconducting devices are also characterized by means of the kinetic inductance (Figure 3.22b), defined as

$$L_k = \frac{\hbar}{2eI_c}, \tag{3.5}$$

$\hbar$ being the reduced Planck's constant, and e being the electron charge [87, 88]. The maximum values of L_k reached in the present device (Figure 3.22b) are one order of magnitude below those reported by Paolucci *et al.*, with the required gate voltage also being reduced from 8 to 3 V. At moderate values of V_g, L_k is in the same order of magnitude for both the Ti and W-C S-FETs. These results suggest that W-C does hold great potential to build superconducting FET-based nanodevices.

Apart from the already presented Ti S-FET device, the absolute values of g_m and L_k and the overall performance of the Ga^+ FIBID W-C device are also comparable to the results reported in S-FETs of other materials. A comparison is provided in Table 3.2.

	T_c (K)	V_g^c (V)	g_m (μA/V)	L_k (nH)
W-C (present work)	4.7	2.5-3	5	0.5
Titanium [49]	0.54	32/8	0.33/15	8
Aluminium [84, 89]	0.6/1.5	23/>70	-	-
Vanadium [90]	5	15	150	0.4
Niobium [91]	7.9	>40	1.6	1

TABLE 3.2: Reported properties of S-FET devices of different materials. Variability between (same-material) samples or reports is indicated with a diagonal bar separating the two different values.

3.6 Conclusions

In this chapter, the experimental results on three different lines of work that use Ga^+ FIBID as a working material have been reported. All three represent a small step forward in an already well-treaded path, further contributing to the applicability and appeal of the technique for the fabrication of this material.

Specifically:

- Non-local transport of superconducting vortices across a channel length of 10 μm has been achieved, yielding an equivalent resistance of 8 Ω in an area depleted of current, solely caused by crossing vortices. This result represents, at the time of writing, the furthest reported value of non-local vortex transport in this manner. Supported by numerical simulations based on the Ginzburg-Landau theory, these results strengthen the applicability of Ga^+ FIBID W-C for the fabrication of functional superconducting nanodevices based on controlled vortex motion.

- An easily reproducible protocol for the fabrication of substrates and superconducting W-C films for STM investigation has been developed and put to the test, successfully achieving STS imaging of the Abrikosov vortex lattice in a

Ga^+ FIBID W-C film fabricated for this purpose. These results enable for further investigation of FIBID-grown materials via STM, including the investigation of other superconducting phenomena on W-C, as well as with advanced studies related to intriguing superconductivity phenomena.

- Local suppression of superconductivity via the application of a gate voltage has been reported in a Ga^+ FIBID W-C S-FET nanodevice. This is the first time that such a phenomenon has been reported in this material, closely following the phenomenology observed by Paolucci *et al.* in Ti transistors. While maintaining comparable properties to the Ti counterparts, Ga^+ FIBID W-C offers enormous patterning flexibility, enabling for the nanomanufacture of advanced FET devices that exhibit great potential in the field of nanosuperconductivity.

Overall, these results feature the vast applicability in basic and applied research of an already well-established growth technique for nanopatterned superconductors. When in need of precise patterning of custom, nano-sized, superconducting devices, Ga^+ FIBID of W-C Ga^+ does deliver with flying colors, and it is indeed bound to see further and exciting new applications and developments in the near future.

Chapter 4

Cryo-FIBID of W-C metallic nanostructures

The object of this chapter is to present recent advances on the recently developed technique of Focused Ion Beam Induced Deposition under cryogenic conditions. A reproducible protocol indicating how to perform it; and the acquired results on the compositional and electrical properties of the deposits are presented here. Because of the novelty of the technique and the subsequent lack of references to construct a path upon, this chapter is structured slightly differently to the others - first, an entire section detailing the growth procedure will be presented. The experimental results will be presented thereafter, in the order they were retrieved.

4.1 State of the art

Within the field of nanomanufacturing, and particularly in the industrial framework, a deciding factor between one or other fabrication technique is the resolution-to-speed ratio - as a rule of thumb, the most appropriate technique will be that that achieves the required resolution target most rapidly. FIBID is characterized by its textitserial nature: in a FIBID procedure no more than one sample is grown at the same time, since the beam must be sequentially scanned over all areas that require patterning. This limits its applicability mostly to circuit edit, TEM sample preparation and cross-sectional FIB/SEM imaging.

Working under cryogenic conditions is an already common scenario in charged-particle beam processing. For instance, FIB milling for TEM sample preparation ranges from challenging to virtually impossible for "soft" materials that are overly sensitive or damaged by exposure to the beam. Low temperatures make some of these materials "hard" enough for them to be FIB-processed whilst maintaining their original properties and structures, and as such, the cryogenic approach is a valuable tool in this procedure [92, 93]. Another noteworthy approach to the exploitation of cryogenic conditions is the usage of water as a temporary resist in nanolithography processes - once solidified under cryogenic conditions (in the form of an *ice resist*, as it is named), some areas are selectively removed by FEB irradiation, and then a metal layer is evaporated on top [94]. The high doses required to carry out this procedure, however, somewhat limit its applicability.

In the context of gas-driven processing, the most relevant feature of cryogenic conditions is that the residence times of gases in the surface of the cooled sample are greatly enhanced in comparison to their room-temperature values. As such, it is intuitive to envision significant changes in the parts of the procedure that strongly depend on the amount of gas present in the surface, and the time it resides there. For instance, the processing speed of gas-enhanced FEB etching can be substantially increased by carrying it out under cryogenic conditions [95].

At this point, it is only logical to consider enhancing the performance of FIBID by carrying out the procedure at low temperature (as described in section 2.1.4), since more precursor available to dissociate would in principle imply a reduced amount of ion dose required to decompose it. Indeed, early works in deposition at cryogenic temperatures using (broad) ion and electron beams beams report successful growth of Sn [96] and the titular W [97]. A more recent and highly relevant work is that of Bresin *et al.*, where the deposition of Pt via FEBID performed at cryogenic temperatures is reported [98]. The low temperature of the substrate favors the formation of a multilayer of condensed precursor material, which is then decomposed by the FEB with a growth rate four orders of magnitude greater than its room-temperature counterpart, all while retrieving a comparable composition of that at room temperature (around 14% of Pt), and achieving a patterning resolution of 22 nm [98]. The mechanism has also been used by the same team to creatively build 3D structures by irradiating one layer, re-injecting the precursor for it to condensate again, irradiate the second-layer, and then heat it all to evaporate the unexposed areas [99]. The usage of a FIB instead of a FEB for this purpose remained an unexplored field until very recently.

FIBID under cryogenic conditions, or, as the authors have coined it, *Cryo-FIBID*, is a nanopatterning technique developed by De Teresa *et al.*, and patented in 2018 [100]. Initially assessed on the deposition of metallic W-C nanostructures via decomposition of $W(CO)_6$ by a Ga^+ FIB under cryogenic conditions, and prior to the writing of this thesis and the realization of the experiments therein, an extensive series of characterization and systematic studies were performed to develop an optimized protocol. This initial development set the grounds for further investigation of the capabilities of the technique, providing with a complete set of optimized operating parameter values (GIS nozzle distance, sample thickness, substrate temperature, and ion dose), and represents the starting point for the experiments performed here.

The extremely recent development of Cryo-FIBID also makes the review on already published work fairly brief: at the time of writing, two main reports exist in the literature concerning Cryo-FIBID: the deposition of W-C [56, 101], directly related to the results shown in this chapter; and the growth of Pt-C deposits following the same principles [102]. In the latter reference, Salvador-Porroche *et al.* report an increase in processing times of 40 times compared to the same procedure performed at room-temperature, and a material resistivity suitable for nanostructure contacting purposes, as well as the application of the approach for large-area substrate marking and defining of working areas.

4.2 Deposition process

Contrary to other growth procedures described in previous chapters, Cryo-FIBID differs from conventional FIBID in more than one way, meriting special treatment for that very reason.

4.2.1 The ion dose

The concept of ion dose (or fluence), which was already discussed in section 2.1.3, takes special relevance in the design of Cryo-FIBID experiments, since the conventional values for this parameter that can be found in room-temperature FIBID of the corresponding materials no longer apply at low temperatures.

Specifically, the dose D is defined as the charge per unit area, or

$$D = \frac{I \cdot t}{A}, \tag{4.1}$$

where I is the ion beam current, t is the exposure time, and A is the area of the deposit. The required deposition time, which is set in the FIB/SEM instrument, can be deducted from the previous equation. In the present work, a dose of 55 $\mu\text{C}/\text{cm}^2$ was used in most of the deposit, unless specified otherwise. With an ion beam current of 10 pA, typical deposition times are of the order of miliseconds.

It is worth mentioning that in conventional FIBID, the *volume per dose*, v_D, also described in section 2.1.3, is a more typical approach to quantify the irradiation dose, due to the fact that this parameter also includes the thickness of the deposit:

$$v_D = \frac{A \cdot z}{I \cdot t} = \frac{z}{D}. \tag{4.2}$$

The main virtue of v_D is that it remains constant when the thickness of the patterned deposit is changed[1]. This is the reason this rather "artificial" construct[2] is used as

---

[1] On first approximation only, since the SE yield changes as the beam impinges on previously deposited material.

[2] Not much more artificial than D itself, actually, but the dose is a more widespread and intuitive parameter in other fields of science.

the operating parameter in the Thermo Fisher instruments, for it is associated to the *material*, rather than to the specific *deposit* - the user fixes v_D, and the software recalculates D as the thickness is modified. In Cryo-FIBID, since the standard values of v_D no longer apply, the basic approach was taken, and D is adjusted by manually setting t instead of z, which is the more common approach. The software in the instrument recalculates z and v_D from this value, but the values obtained in such a way are not relevant in Cryo-FIBID.

The size deviation from the nominal value mentioned in the previous section (*i.e.*, the change in A from its expected, nominal value, to the actual size of the deposit) may represent a significant difference in deposition time if the pattern is big enough. For μm-sized patterns, it is advisable to first grow one using the nominal value of A to assess the extent of the deviation and its influence on the deposition time, and then adjust the value of A to the real measured value, with the subsequent change in t[3].

4.2.2 The process

Taking the previous discussion into account, the growth protocol of Cryo-FIBID can be summarized as follows.

Setup

1. The refrigeration line is purged by setting the N_2 at a base level of 1 bar. This gas should flow throughout the full line at room temperature for at least 30 minutes, which can be invested in the following steps.
2. The sample stage is placed at the eucentric height, and the area of interest is located via SEM imaging. Thereafter, the stage is tilted to 52° and the GIS nozzle of the gas to be deposited (in the present case, $W(CO)_6$, as usual) is injected. Using very low magnification, the end of the injector can be imaged via SEM.
3. With the injector inside the chamber and while retrieving a live image of its position above the tilted substrate via SEM, the height of the stage is increased very slowly. A significant, abrupt change in position of the otherwise static GIS nozzle will indicate direct contact between the injector and the stage. The height at which this occurs should be noted, as it will be used as a reference for growth[4]. The stage is then lowered, and the GIS can be retracted.

---

[3] Or, alternatively, if the dimensions of the deposit must be as precise as possible, the nominal values can be recalculated to account for the deviation factor. In this case, the dose of A should be kept at its nominal value, which, ideally, would coincide with the real one if the correction is properly applied.

[4] The actual *need* for performing this measurement is arguable, since most GIS nozzles are typically located around 0.1 mm away from the eucentric height; which represents a 1% of the required 10 mm. In any case, it is not harmful to do so, either.

4. Depending on the sample, it may be advisable to grow some alignment marks using the FIB at the eucentric height to facilitate sample location and FIB focusing at high working distances. Should it be the case, the FIB current can be increased to mill one or two distinct features, such as crosses, that can be used as reference points. The vibrations induced by the passage of N_2 will very likely result in a significant shape fidelity loss of these features (whose milling can take several minutes, depending on their size and the selected current), but in principle, it should not be a problem as long as they are "visible" with the FIB.
5. The stage is then lowered down to the working distance, equal in instrument coordinates to 10 mm plus the previously measured GIS distance. The difference in focus between the eucentric point and the working point is significant, and as such, it is wise to lower the sample in steps of 1-2 mm, readjusting the FIB focus on each using the previously milled samples or any other useful sample feature. It is not necessary to achieve perfect focus, just enough so the features are visible in the next step and the FIB can be refocused again minimizing other sample irradiation.
6. Once at the working distance, the FIB is finely focused using a sample feature or an alignment mark.
7. The coil in the refrigeration system is inserted in the LN_2 reservoir.[5].

Deposition

1. The N_2 pressure is increased to 1.6 bar, and a temperature setpoint is introduced in the heater. In the case of $W(CO)_6$ Cryo-FIBID, a sample holder temperature of 173 K (-100°C) was used in all cases.
2. Once the temperature has stabilized, the stage is relocated to center the field of view in the area where the deposit is to be grown.
3. The GIS nozzle is injected, and the precursor is delivered during 10 s. The GIS is retracted afterwards.
4. With the GIS injector retracted and the precursor flow closed, the FIB irradiation is performed during the deposition time estimated from the corresponding dose (section 4.2.1).
5. The N_2 pressure is decreased to its purging value of 1 bar.
6. The sample holder temperature is increased in steps of 10°C (letting it stabilize) up to 323 K (50°C).

---

[5] As the heater can be used to regulate the stage temperature, it can also be inserted at the beginning of the session. If it is not, the stage will remain at room temperature until the coil is cooled.

7. The sample is let at 50°C for 15 minutes, to ensure complete removal of the condensate.
8. The temperature is lowered to 20°C and the stage is brought to the eucentric height, where the sample can be imaged.

It is advisable to keep the N_2 flowing at all a times at the purging value of 1 bar to minimize the chances of the line getting obstructed. At the end of the session and with the coil outside the LN_2 reservoir, gas should be let flow through the line for at least 5 minutes.

These are the main guidelines that define the workflow in Cryo-FIBID sessions. There is still plenty of room to toy around with, varying typical parameters such as the deposition time (*i.e.*, the ion dose); or modifying those that are somewhat more unconventional, such as the working distance, the precursor injection time, or the temperature of the precursor reservoir. Some of them will be explored in the next sections.

4.3 Results

4.3.1 Initial assessment

The initial work performed on Cryo-FIBID consisted of systematic growth of nanowires to assess the patterning capability of the technique. These nanowires were then further characterized by means of TEM and low-temperature electrical measurements, in a similar fashion as the experiments presented in the previous chapter, and as described in chapter 2.

Growth and shape fidelity

Following the procedure described above, the first deposits were grown with an ion current and dose of 10 pA and 55 $\mu\mathrm{C/cm^2}$, respectively, patterned as a nanowire with four perpendicular leads (Figure 4.1). An alignment mark was milled in close proximity to the deposition area using an ion beam current of 50 pA prior to cooling.

This nanostructure was fabricated by sequentially irradiating five rectangle-shaped patterns, one for the main body of the nanowire, and the other four corresponding to each of the perpendicular contacts. These squares were nominally 200 nm in width, and 10 and 1.5 μm in length, respectively. These dimensions correspond to pattern areas of 0.3 and 2 $\mu\mathrm{m}^2$, which, as it can be calculated from equation 4.1, yield deposition times of 16.5 and 110 ms, amounting to a total of 176 ms of total exposure time.

The standard volume per dose for room-temperature growth of W-C used in this thesis is $8.2 \cdot 10^{-2}$ $\mu\mathrm{m^3/nC}$ ($8.2 \cdot 10^{-9}$ $\mathrm{cm^3}/\mu\mathrm{C}$) which, for $z = 30$ nm, yields $D = 3.61 \cdot 10^{-1}$ $\mathrm{nC}/\mu\mathrm{m}^2$ ($D = 3.61 \cdot 10^4$ $\mu\mathrm{C/cm^2}$). Growing the same deposits at room

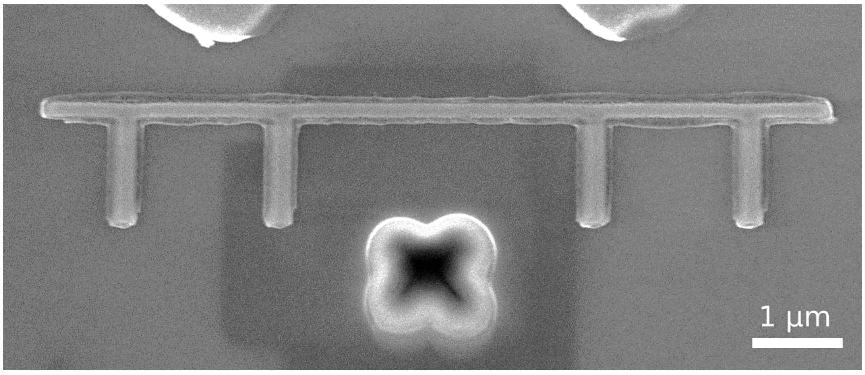

FIGURE 4.1: SEM image of a standard W-C nanowire grown by Cryo-FIBID. The alignment mark is visible. In later deposition, the mark was milled further away from the actual deposition point.

temperature with such a dose would take around 116 seconds - three orders of magnitude above the time yielded in cryogenic conditions. This is a vast, dramatic improvement in the processing speed that clearly highlights the potential of the technique.

A remarkable geometrical feature present in the deposits is the appearance of some sort of wing-like feature that surrounds the main body of the deposit (Figure 4.2a). SEM images taken at 52° reveal that this feature is slightly lifted above the surface of the substrate (Figure 4.2b). This effect seems to recurrently appear in the Cryo-FIBID deposits grown in this manner, and, as it will be discussed later, is dependent on the ion dose.

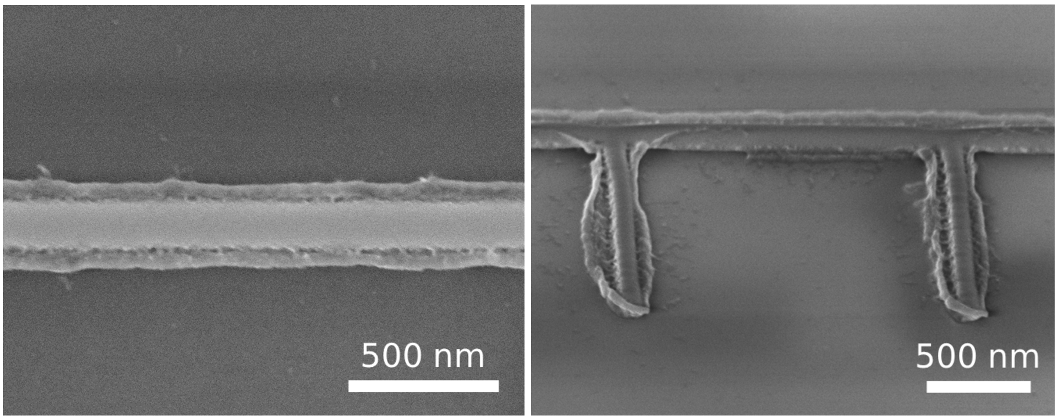

(A) Top view.

(B) Tilted view.

FIGURE 4.2: SEM images of the wing-like features in Cryo-FIBID W-C nanowires.

Microstructure and composition

The composition and microstructure of the samples were assessed, as usual, by means of TEM analyses. Conventional TEM imaging indicates a deposit thickness of around 30 nm, and reveals the presence of two layers within the deposit, one showing darker contrast than the other, and thus indicating significant compositional differences between the two (Figure 4.3a).

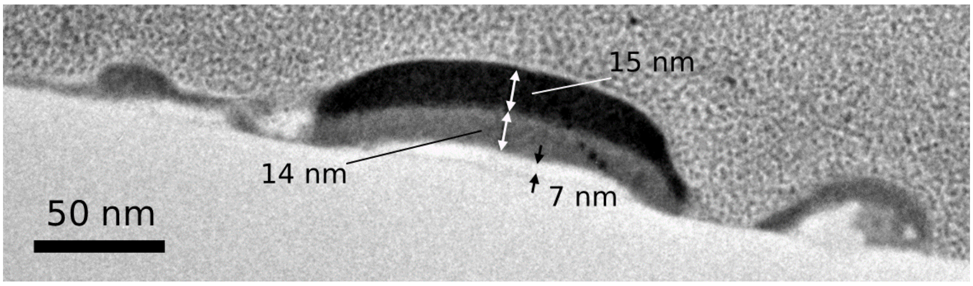

(A) TEM image.

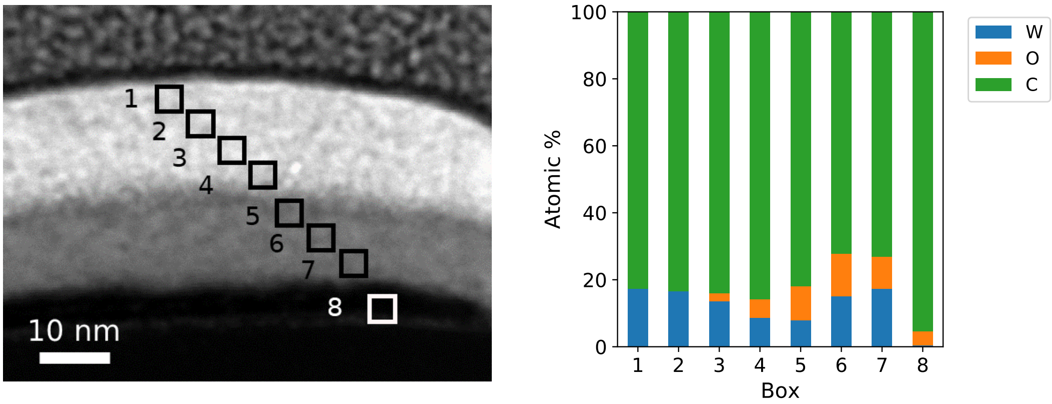

(B) STEM-HAADF image.

(C) EDS quantification.

FIGURE 4.3: TEM study of W-C Cryo-FIBID nanowires.

EDS combined with STEM-HAADF indicates that on average, the lower part of the deposit shows a greater amount of oxygen in terms of atomic percentage (Figures 4.3b and 4.3c). Conventionally, this feature tends to happen on the upper layers of the deposit, rather than at its bottom, and is usually accounted for by oxidation induced by air exposure during sample handling. In this case, the fact that it occurs in the vicinity of the substrate is compatible with effects arising from the essentially distinct growth mechanism, which involves the decomposition of the condensate layer, much thicker than the molecular monolayer present in conventional FIBID.

The metallic content falls in the 10-20% range approximately. Gallium is virtually absent from the sample (below the detection limits of the instrument, less than 1%), in agreement with the low dose and irradiation times characteristic to growth. Notably enough, the cross-sectional cut shows a thin strip of carbon (above 95%) between the deposit and the substrate. Its origin can be related to contaminant deposition prior to the growth of the sample, induced by the FIB imaging required to focus the beam. This further strengthens the suggestion of growing alignment marks within a reasonable distance of the sample, far enough to contaminate the deposition area as less as possible, but close enough so the beam remains in focus. The wing features present W content (10-15%), and a greater amount of oxygen than the upper part of the deposit.

Concerning crystallinity, no long-range order is detected in the samples. The lower layer seems to be fully amorphous, while the upper part shows features that point towards very-short range order (around 0.7 nm).

Electrical properties

At room-temperature, the samples exhibit ohmic behavior, with $\rho_{300\text{K}} \sim 900\ \mu\Omega\cdot\text{cm}$. The metallic-like behavior they show allows the material to be used for the purposes of electrical contacting, as it will be shown in section 4.3.3.

Low-temperature electrical measurements performed on Cryo-FIBID nanowires evidenced one important drawback of the technique: at the time of writing, down to 0.5 K, superconductivity has *not* been detected in W-C nanostructures grown by Ga^+ Cryo-FIBID. This phenomenon is in stark contrast with the room-temperature Ga^+ FIBID W-C deposits, and even the He^+ FIBID nanostructures, both of which present superconducting behavior (within a certain variability, but reasonably close).

With $\rho_{2K}/\rho_{300\text{K}}$ being around 1.2, the temperature dependence of the nanostructures is significantly similar to their counterparts grown at room-temperature, but the expected superconducting transition does not occur within the expected 3-5 K range, nor at all within the measured range, down to 0.5 K (Figure 4.4).

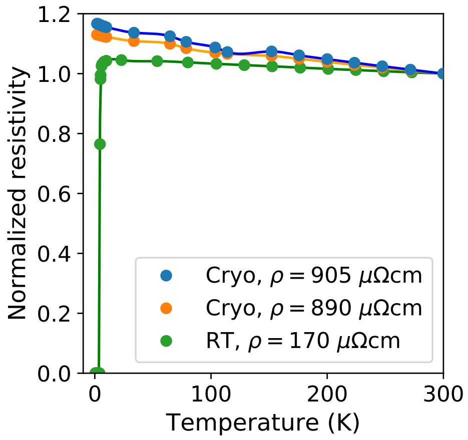

FIGURE 4.4: Temperature dependence of the resistance of W-C nanowires grown via Cryo-FIBID. A measurement corresponding to a standard, comparable nanowire grown via room-temperature Ga^+ FIBID is also shown for comparison. $\rho_{300\text{K}}$ values are indicated.

Any further measurements related to the superconducting properties of the deposits were evidently not carried out on these samples.

It is expected for these samples to undergo surface oxidation as they are exposed to air after fabrication, during handling and preparation for the low temperature measurements. To ensure this oxidation was not a fundamental reason for the lack of superconducting behavior, a thin protective carbon layer was deposited on top of some of the nanowires by exposing them to the FEB during a few minutes. No significant differences were observed in the electrical measurements.

4.3.2 Deposition tuning

As presented in section 4.1, the experiments reported here represent a further step in the already developed protocol for Cryo-FIBID of W-C. Whilst that initial assessment provided with the much needed tools required to reproduce the procedure, a logical continuation is that of exploring the limits and applicability of the technique, as well as to investigate further improvements on the protocol. In this section, the results concerning the effects of modifying both a typical and a less-conventional growth parameters are reported: namely, the study of the influence of the ion dose, and the precursor temperature.

Influence of the precursor temperature

As mentioned in section 2.3, the precursor materials are stored in solid form in dedicated reservoirs in the GIS, which are heated to sublimate them by setting a "precursor temperature", T_p. As the GIS nozzle is opened, this vaporized gas is continuously released to the chamber until the valve is closed.

The design of the GIS nozzles in the Nova 200 FIB/SEM instrument does not allow for precise control of the GIS valves - they are either in the "open" or "closed" positions. As such, the precursor pressure can not be directly regulated - the precursor gas flows into the chamber when the valve is opened and quickly reaches a dynamical equilibrium with the vacuum system, which is constantly pumping gases away from inside. The chamber pressure is usually one order of magnitude above its base value when the precursor is being released (typically from 10^{-6} to 10^{-5} mbar).

However, the precursor pressure can be indirectly regulated by modifying the value of T_p, which is indeed a controllable parameter. Lowering its value significantly reduces the precursor flow. For Cryo-FIBID, lowering the precursor pressure while keeping the injection time at 10 seconds results in a thinner condensate layer available for decomposition. The thickness and the composition of the deposits can be adjusted in this manner.

The "standard" GIS operation value of T_p for $W(CO)_6$ is 50°C, which, as described in section 4.3.1, yields conducting nanostructures with thickness of around 30 nm. To explore the influence of T_p on the properties of the deposits, its effect was assessed for values of 40 and 45°C, whilst keeping all other parameters in their previously-optimized values (ion beam current of 10 pA and ion dose of 55 μC/cm^2).

Visual inspection of SEM images (Figure 4.5) reveals that for $T_p = 40°\text{C}$, the deposits present a more diffuse look and less sharp appearance that those with T_p values of 45 or 50°C. Deposits with $T_p = 45°\text{C}$ also exhibit wing-like features.

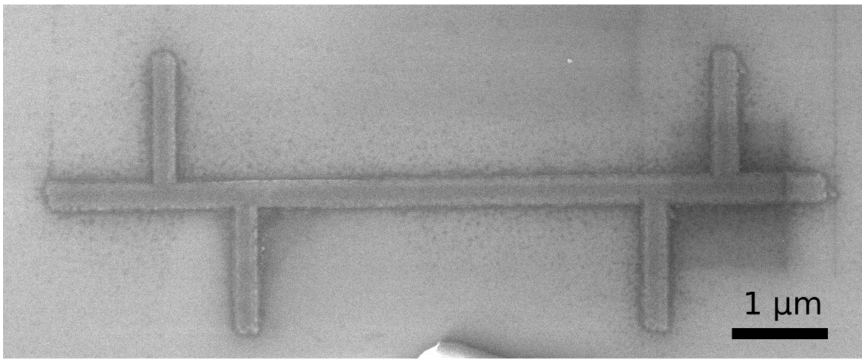

(A) $T_p = 40°\text{C}$.

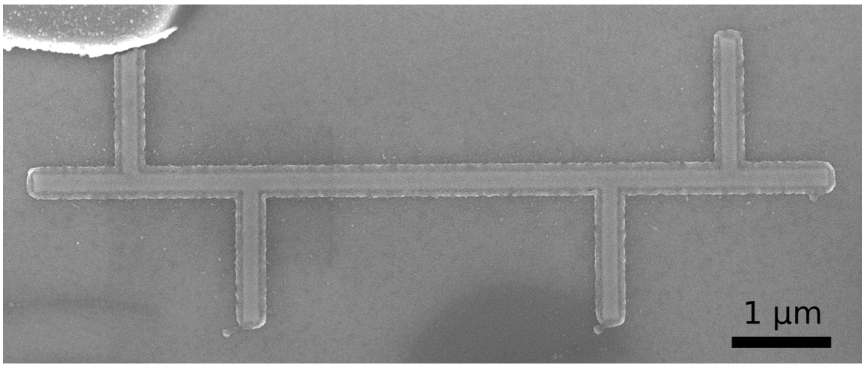

(B) $T_p = 45°\text{C}$.

FIGURE 4.5: SEM images of Cryo-FIBID W-C nanowires grown with the indicated precursor temperatures.

These samples were joined to pre-lithographied Ti pads using Pt FIBID contacts and their room-temperature electrical response was assessed using the microprobe station in the *Helios 650* instrument. Samples with $T_p = 40°\text{C}$ did not present conducting behavior, while those with $T_p = 45°\text{C}$ exhibit an ohmic response, with $\rho_{300\text{K}} \sim 170\ \mu\Omega\cdot\text{cm}$. The temperature dependence of the resistance of the latter was measured using the PPMS instrument, revealing that no superconducting transitions occur (down to 0.5 K), in a similar fashion to the nanowires grown with $T_p = 50°\text{C}$. A significant increase in resistivity was observed in comparison to the previous measurement taken in the microprobe station inside the *Helios 650* chamber, from 170 to 360 $\mu\Omega\cdot\text{cm}$.

The compositional and structural properties of the nanowires with $T_p = 45°\text{C}$ were assessed in a TEM study. STEM-HAADF images show a deposit thickness of 15 nm, reduced, as expected, when comparing it to those grown with $T_p = 50°\text{C}$. EDS analyses indicate that these deposits exhibit a reduced amount of W, not greater than an atomic 10%. One of the samples exhibits a central area sandwiched by two regions almost completely depleted of tungsten (Figure 4.6). The presence of oxygen in the lower region can be originated as a signal coming from the SiO_2 of the substrate, as well as coming from oxygen leftovers from the precursor decomposition. These can also be present on the top layer, which, furthermore, is likely to have undergone oxidation upon exposure to ambient conditions.

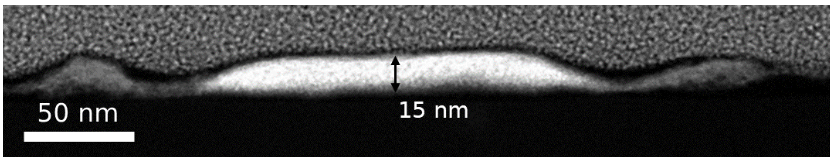

(A) General view.

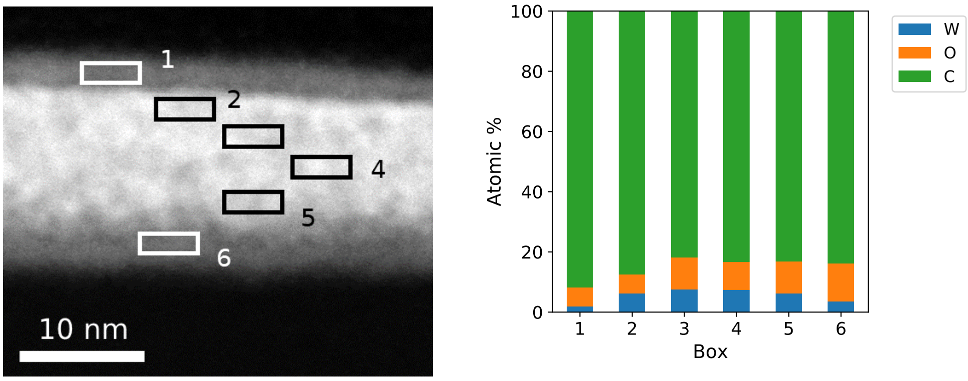

(B) High magnification view.

(C) EDS quantification of the boxes in the previous image.

FIGURE 4.6: TEM characterization of Cryo-FIBID W-C samples grown with a precursor temperature of 45°C.

Influence of the ion dose

The appearance of the wing-like features that encircle all of the deposits grown using the "standard" conditions in the present work poses an intriguing question. Although they are in principle harmless when the deposits are large (in the μm range), they represent a serious patterning artifact and severely hamper the lateral patterning resolution and shape fidelity of the technique.

A plausible hypothesis for their occurrence relates to condensate "overexposure", akin to somewhat comparable mechanisms that take place when a resist is irradiated in optical or electron beam lithography [103]. Stray particles such as backscattered primary ions, SEs, or SIs could be responsible for the decomposition of the precursor as they are emitted or backscattered away from the point of direct irradiation.

This hypothesis was put to the test by sequentially growing a test pattern of 10 μm-long lines with variable, increasing separation in between. The ion beam current was set to 1 pA, to more easily achieve lower values of ion dose; and T_p was set to 45°C. The prominence of the wings does indeed depend on the ion dose, decreasing as its value is reduced (Figure 4.7).

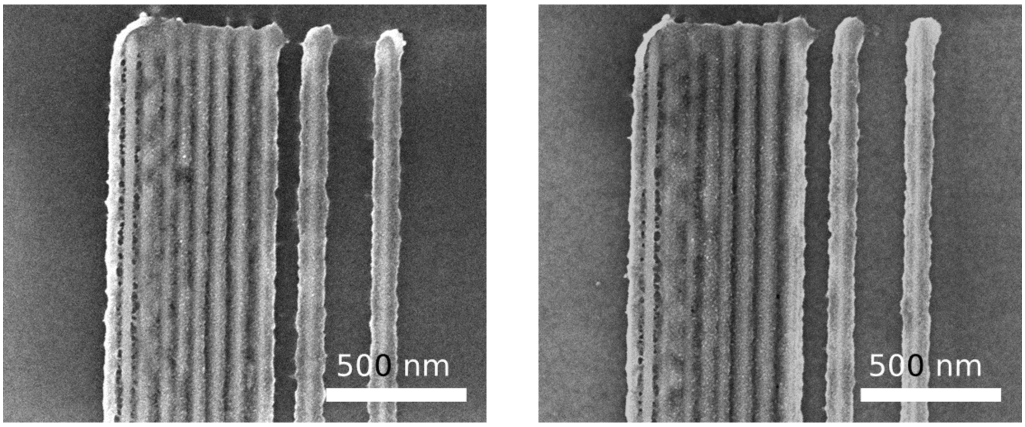

(A) 55.0 μC/cm^2. (B) 49.5 μC/cm^2.

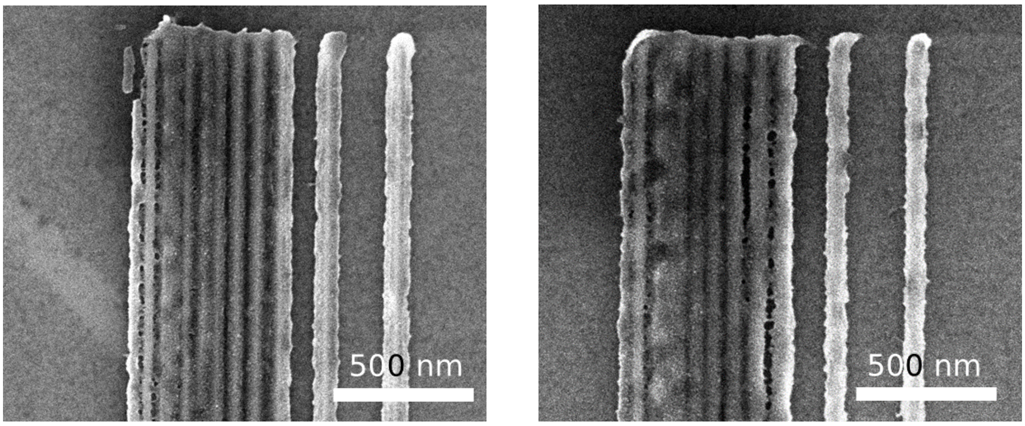

(C) 44.0 μC/cm^2. (D) 22.0 μC/cm^2.

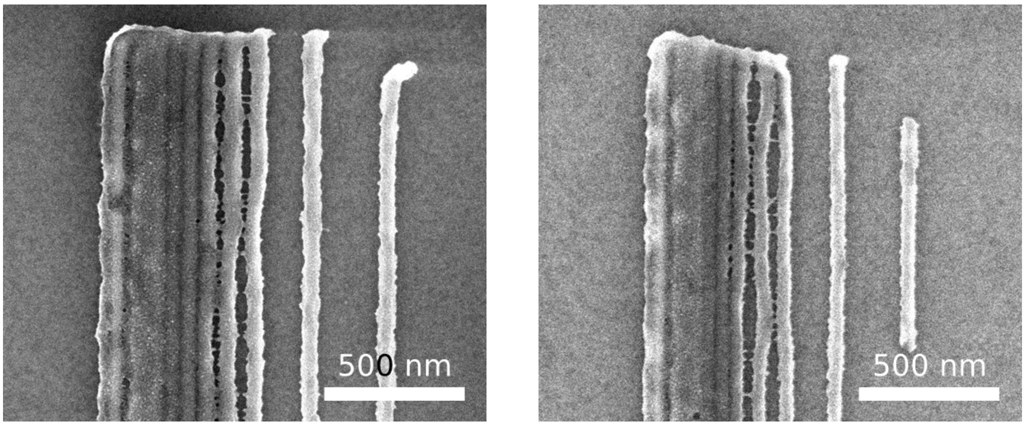

(E) 16.5 μC/cm^2. (F) 11.0 μC/cm^2.

FIGURE 4.7: Dose dependence study in Cryo-FIBID W-C nanowires. Each array consists of 16 nanowires patterned in "line" mode, nominally 10 μm in length and with progressively increasing nominal separation (1, 2, 5, 10, 20, 30, 40, 50, 60, 70, 80, 90, 100, 200 and 300 nm.

TEM analysis of some of these samples reveals a thin, upper layer joining those in close proximity (Figure 4.8).

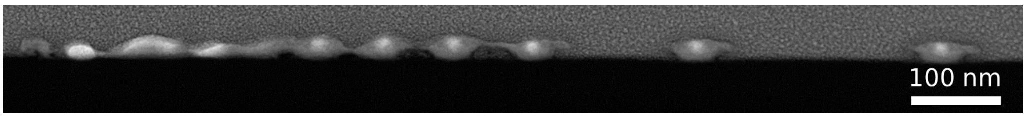

(A) 44.0 $\mu C/cm^2$.

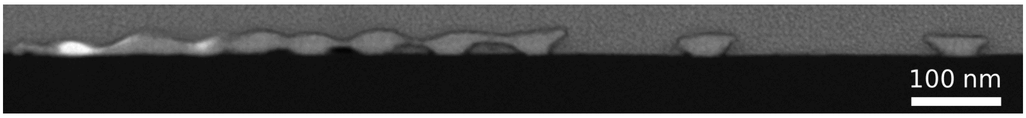

(B) 22.0 $\mu C/cm^2$.

FIGURE 4.8: Cross-sectional HAADF images of the arrays of W-C Cryo-FIBID nanowires shown in figures 4.7c and 4.7d.

The trapezoidal shape of the cross-sectional area of the nanowires is accounted for by differences in received dose along the condensate layer (Figure 4.9).

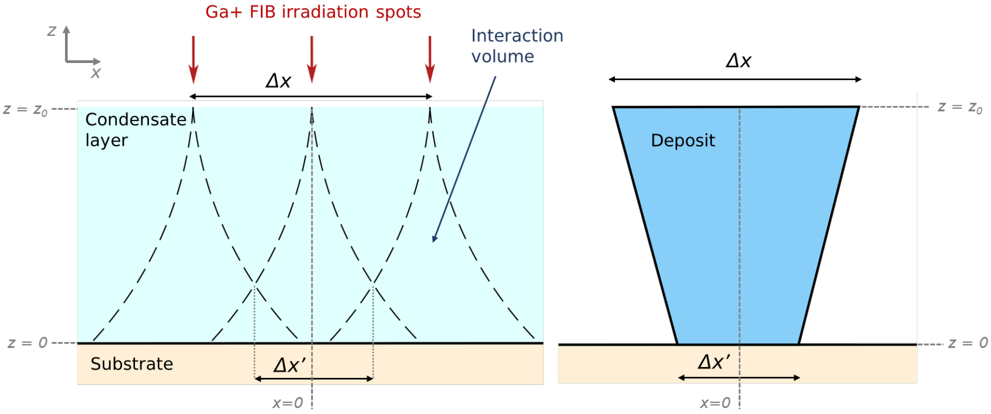

(A) Dose variability in a single deposit (cross-sectional view, exaggerated vertical scale).

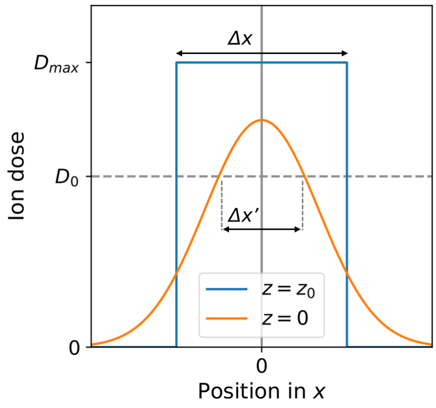

(B) Dose at the top and bottom parts of the condensate.

FIGURE 4.9: Dose distribution in a single nanowire, grown by exposure of three irradiation spots.

In analogy to optical and electron-beam lithography procedures, a certain area of the condensate can be considered to be "revealed" (*i.e.*, irradiated enough so it gets permanently deposited on the substrate above the precursor condensation temperature) once it has received some ionic dose, D_0. The dose delivered to the substrate is maximum at the top part of the condensate (D_{max}) and then it decreases with depth within the layer, since, within their interaction volume, incoming ions progressively lose energy and are scattered as they interact with the molecules of the condensed precursor and the deposit itself.

Near the substrate, the lateral extent to which the received dose equals or exceeds D_0 (and thus, results in deposition), is reduced in comparison to that at the top. Only areas that are either directly below the irradiation spots, or that receive an enhanced dose thanks to overlapping with interaction volumes of neighboring irradiation spots get a dose sufficiently high to induce deposition. As a consequence, the lateral size of the deposit, Δx, is greater at the top part of the deposit (fully irradiated), than at the bottom, $\Delta x'$ (partially irradiated). This effect is equally observed in negative-tone resists in optical lithography or electron-beam lithography [103].

Similar arguments justify to the appearance of the upper layer (Figure 4.10).

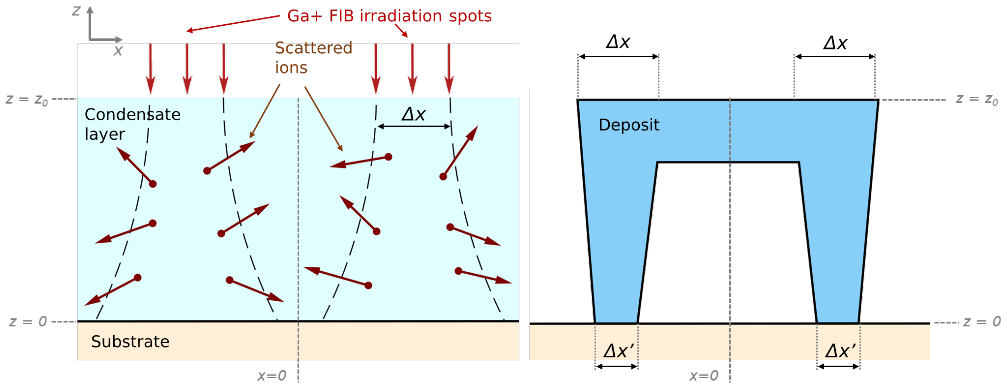

(A) Dose variability in two neighboring deposits (cross-sectional view, exaggerated vertical scale).

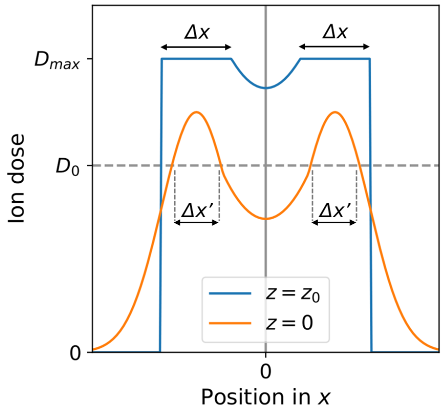

(B) Dose at the top and bottom parts of the condensate.

FIGURE 4.10: Dose distribution in two neighboring nanowires.

Forward- and backscattered ions are responsible for irradiation in areas neighboring the spot the beam was focused at. With incoming ions having more energy at the top of the layer, backscattering is more pronounced in the upper layers of the condensate, resulting in sensitization in areas neighboring irradiation spots in close proximity. In deeper layers of the substrate, the backscattering effect is reduced (in addition to the lower layers already receiving a reduced dose in comparison with those at the top), and the lateral irradiation only exceeds D_0 at the top.

In terms of composition, the nanowires grown with a dose of 44 $\mu\mathrm{C}/\mathrm{cm}^2$ present a variable amount of atomic W, ranging in the 40-20% range. The metallic content peaks at the "core" of the nanowires, while the areas surrounding it present a larger amount of oxygen in average. In samples deposited with an ion dose of 22 $\mu\mathrm{C}/\mathrm{cm}^2$, the metallic content is much lower, reaching a maximum of around 10%.

Overall, these results support the initial hypothesis of condensate "overexposure" being responsible for the appearance of the wing-like features. In general terms, reducing the dose does reduce the prominence of the wings, although at the cost of also reducing the metallic content of the sample. These wings may likely be particularly prominent in Cryo-FIBID of W-C given the high atomic number of W, which results in higher ion scattering than that induced by lighter atoms.

4.3.3 Growth of targeted nanostructures

After setting the grounds for the deposition process and with a clear vision of what to and not to expect from the deposits, the technique was "properly" exploited for actual purposes, both functional and demonstrative in nature. In this section, the two examples that were presented in the corresponding article [56] are reviewed.

Contacts for electrical characterization of external samples

The vast majority of scientific experiments that require electrical characterization of nano-objects require, in some form, connecting the nano- with the macro-scale, since most of the characterization is performed in the latter[6]. A series of electrical contacts, nanometric in one end and (at least) micrometric in the other.

In the present work, such a link was achieved by making use of substrates prelithographied with Ti pads (as described in section 2.1.6). This approach is particularly convenient if the actual sample under study is grown via FIBID, since steering the beam to place the sample near these pads is reasonably simple. However, when

---

[6] Electrical characterization in the micro-scale, between the two, is also commonplace. Microprobe stations, either built inside the instruments or operated outside, represent a convenient way of assessing the electrical properties of a sample, provided that these can be studied in ambient or near-ambient conditions, in most cases. However, they do still require a connection between the nano-sized object that is to be studied and the μm-sized region where they are to be placed.

the samples of interest are grown using methods that do not allow for direct positioning of the sample (*e.g.*, some chemical methods, which result in a random distribution of a large number of samples over the substrate), if the same approach of pre-lithographied pads is used, one can either hope that one of the samples randomly falls nearby (which, statistically, does happen and is indeed a feasible approach), or perhaps reposition it via nanomanipulation.

A third approach would be to grow the contacting pads oneself, placing them wherever the sample is located. Optical or electron-beam lithography require delicate alignment procedures that make placing the contacts in this manner quite challenging for small samples - unless the sample in question were really worth it, in most cases it is generally easier to get the contacts first, and then use one of the former approaches. In addition, lithography techniques require the use of a resist, that sometimes sticks to the substrate and/or can contaminate the sample under study. FIBID makes it much more easy to place the contacts wherever they are required, but patterning μm-sized areas requires extremely large amounts of time, which are, once again, inconvenient (section 2.1.4).

The breakneck speed of Cryo-FIBID comes here into play - massively increasing the growth rate while maintaining the precision positioning of FIBID makes this technique a very suitable candidate for the growth of electrical contacts. Furthermore, the extremely short exposition times also minimize substrate amorphization and metal implantation when compared to conventional FIBID.

This approach was put to the test using a 25 nm-thick Pt-C nanowire grown via conventional FIBID as a dummy sample and placing four kite-shaped electrical contacts on top of it via Cryo-FIBID (Figure 4.11a).

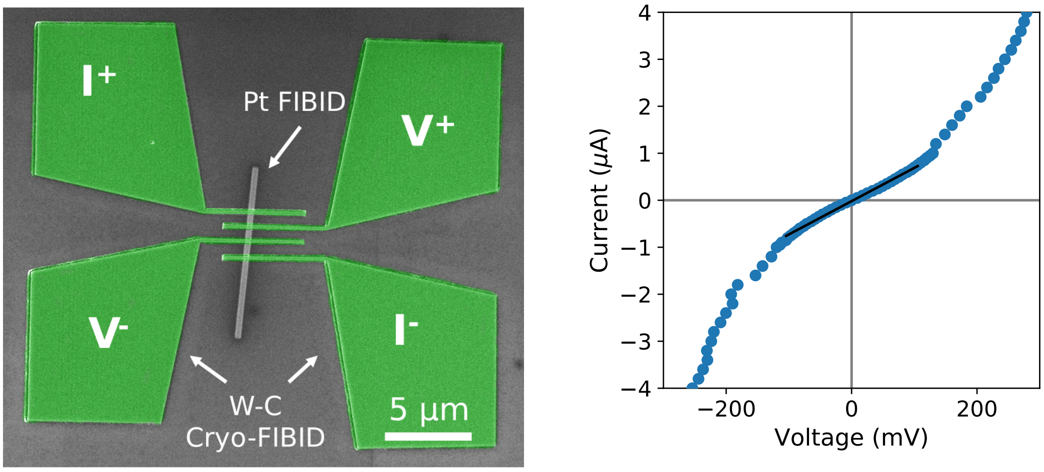

(A) SEM image of the final layout. The W-C Cryo-FIBID contacts are shown in green.

(B) Current-voltage characteristic of the Pt-C NW retrieved using four microprobes over the W-C Cryo-FIBID contacts.

FIGURE 4.11: Functional W-C electrical contacts grown by Cryo-FIBID, placed on top of a FIBID Pt-C nanowire.

The contacts were patterned using an ion beam current of 10 pA and the optimized dose for Cryo-FIBID of 55 μC/cm^2, amounting to a total deposition time of 50 s (at room temperature, growing this structure would take roughly 10 hours). Placement of the contacts over the nanowire was achieved by making an alignment mark near the area of interest, minimizing irradiation over the sample. Thereafter, using the microprobe station in the Helios 650 FIB/SEM instrument, the voltage-current characteristic was retrieved (Figure 4.11b). The results are in agreement with those previously reported for Pt-C nanowires of comparable thickness [104].

Speed demonstration

It should have been made clear at this point that the main appeal of Cryo-FIBID is the increase in processing speed. While "targeted" might be too-big-of-a-word to describe a large array of squares whose only purpose is to show how fast they can be deposited and that are otherwise pointless, growing it is quite the flashy way of demonstrating this feature (Figure 4.12).

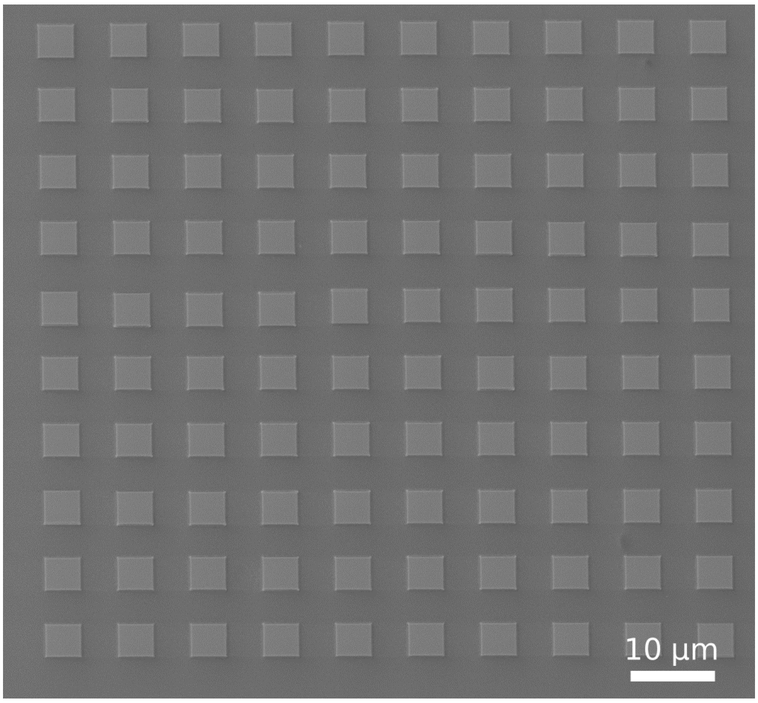

FIGURE 4.12: Array of 100 4×3.85 μm W-C squares grown via Cryo-FIBID.

Using the standard dose of 55 μC/cm^2 and an ion beam current of 10 pA, the deposition of the array of 100 W-C micrometric squares[7], took 1 minute and 25 seconds (854 ms per square), not taking into account cooling and heating. Growing this structure at room temperature would take roughly 14 hours.

---

[7] Despite being originally patterned as 5×5 μm squares, due to the deformation induced by working far from the eucentric height, the deposits are actually rectangular, 4 × 3.85 μm in size.

4.4 Conclusions

In this chapter, the experimental procedure of FIBID under cryogenic conditions, the characterization of the subsequently grown samples, and the potential applications of the deposits have been presented and discussed. These steps, along those already performed and published [56, 101], set the foundations for that which exhibits the potential to become a relevant nanopatterning technique in the nanofabrication framework.

Conventional FIBID of large areas of material is, in most cases, discarded as an option due to the procedure being cumbersome and unpractical. With typical doses and beam currents, the deposition time is usually too long (tens of hours) for the process to be worth it - with the added difficulties posed by keeping the beam in operation during such prolonged intervals of time. While still limited by the coooling-heating cycle, Cryo-FIBID vastly overcomes this issue by reducing the deposition time from two to three orders of magnitude, ensuring the viability of the technique for the deposition of this type of structures. As it has been shown in this chapter, Cryo-FIBID certainly holds the potential to expand the scope of FIBID towards larger areas whilst keeping its resist-free and self-alignment features. For instance, all growth issues addressed for the growth of large thin films via FIBID (section 3.4) are greatly simplified if the procedure is performed at low temperature. Functional electrical contacts whose deposition would take hours in conventional conditions have been successfully placed on a test sample with an irradiation time of less than two minutes.

The other key advantage of Cryo-FIBID over conventional Ga^+ FIBID is the reduction in ion damage and metal implantation it involves. While, as already described, amorphization and Ga implantation induced by ion bombardment over the sample is an intrinsic, unavoidable feature of Ga^+ FIBID, the much reduced values of ion dose required in Cryo-FIBID also decrease the prominence of this effect, as evidenced, for instance, by the virtual lack of atomic Ga in the chemical characterization of the samples (that is, below the resolution limit of the instrument).

One of the less-exciting features of W-C Cryo-FIBID deposits is the lack of superconductivity shown by its deposits. At the time of writing, the reason for this difference in the electrical behavior is not fully understood and poses an open question. As a silver lining, this phenomenon might provide further insight on the true nature of superconductivity in W-C grown by conventional FIBID, which is also, at the time of writing, not a completely resolved issue.

In any case, Cryo-FIBID does certainly represent a promising and exciting variant of the now-solidly established FIBID, and is bound to see more development in the near future.

Chapter 5

He^+ FIBID of superconducting nanostructures

In this chapter, the results on the investigation of He^+ FIBID of W-C are presented. They were carried out in collaboration with the *Institute of Ion Beam Physics and Materials Research* at the Helmholtz-Zentrum Dresden-Rossendorf, in Dresden (Germany). The operation of the HIM instrument was performed by Gregor Hlawacek.

5.1 State of the art

The relatively recent rise and establishment of Helium Ion Microscopy and its applications to material growth make the investigation of W-C He^+ FIBID a mostly unexplored, inciting research field. HIMs indeed provide with a much more fine beam, whose reduced spot size and lighter ion mass translate to lateral patterning resolution enhancement, and a less "aggressive" ion-substrate interaction, with reduced substrate amorphization and no metal implantation. The logical follow-up question is whether the resulting nanostructures will also exhibit the superconducting properties that make Ga^+ a fun playground to get one's hands busy on.

At the time of writing, reports on He^+ FIB induced decomposition of $W(CO)_6$ are certainly scarce, further enhancing the appeal of its investigation. The bulk of the already performed work is centered on 3D growth of W-C nanostructures, which will not be investigated in the context of the present thesis. While 2D and 3D FIBID are distinct enough to merit different treatment, the already performed work is still worth reviewing here. It must be kept in mind, however, that the fundamental differences between the growth mechanisms are expected to make themselves apparent in the properties of the deposits.

Most remarkably, 3D deposits of He$^+$ FIBID W-C exhibit crystallinity, a feature that Ga$^+$ FIBID W-C notably lacks[1]. Secondly, the amount of atomic W detected in 3D He$^+$ FIBID deposits significantly exceeds that reported in Ga$^+$ growth; up to 70% compared to around 40%, respectively.

These results pour more fuel to the burning question of the origin of superconductivity in FIBID W-C, since these two very notable differences are highly likely to make the answer different for each type of growth. In particular, 3D He$^+$ FIBID W-C shows 20-30 nm-sized grains that exhibit crystallinity compatible with a WC_{1-x} phase[2], which would account for the superconducting behavior of the material. The measured critical temperature is also different and higher than that of Ga$^+$ FIBID, falling within the 6.2-7.1 K range (roughly up to 2 K above that of Ga$^+$ FIBID) [74, 105].

The present work is centered, however, on in-plane growth, reports of which are absent from the literature. At the time of writing, a single published applied research article refers to the usage of in-plane He$^+$ FIBID W-C nanostructures: Basset *et. al* [106] report the fabrication and usage of superconducting He$^+$ FIBID W-C nanowires in combination with Nb as constituents of microwave resonator devices. The nanowires exhibit superconducting behavior with T_c between 4 and 6.5 K, and B_{c2} above 5 T. Other remarkable feature of these nanowires is their length, up to 390 μm, achieved in virtue of the increased stability of the HIM instrument (when compared to Ga$^+$ FIBs).

In any case, a systematic growth and characterization report of in-plane He$^+$ FIBID W-C nanostructures is lacking in the literature at the time of writing. In this chapter, such a contribution is presented.

5.2 Growth and local characterization

5.2.1 Instrument setup

As anticipated in chapter 3, growth of W-C nanostructures was performed using a commercial Zeiss ORION NanoFab HIM, hosted in the Ion Beam Center facility of the Helmholtz-Zentrum Dresden-Rossendorf research center in Dresden, Germany. The instrument was operated at acceleration voltages of 25-30 kV, and while the impact on the ion beam current on the features of the deposits was explored for the 1-40 pA range, the "operating", standard current was of 15 ± 5 pA. It is worth noting that, unlike Ga$^+$ FIBID, in some instances the ion beam current was modified by changing the gas pressure at the GFIS, rather than changing the aperture only. Different doses in the 0.3-2.0 nC/μm^2 range were assessed, with particular focus on nominal values of 0.7 and 2.0 nC/μm^2.

---

[1] At least in a long-range scale, as mentioned before. Some reports indicate the existence of very-short range order in the form of nm-sized nanocrystallites.

[2] With $1-x$ ranging between 0.13 and 0.36.

The already familiar $W(CO)_6$ material, heated to 55°C, was used as a precursor for the deposition, and was injected using a multi-GIS system, with the nozzle positioned around 50-100 μm away from the substrate in the vertical direction, and 200-250 μm away from the center in the substrate plane. The instrument had a base pressure of $2\text{-}3{\cdot}10^{-7}$ mbar, which was raised to $1{\cdot}10^{-5}$ mbar during deposition. No other precursor materials were used during any of these experimental sessions.

Silicon pieces with a thermally-grown 300 nm-thick SiO_2 layer on top were used as substrates. As usual, a contacting pattern of several Ti pads was grown using optical lithography prior to the FIBID procedure.

Samples were patterned following the "standard" geometry - a long, straight channel with two leads perpendicularly placed near its ends (Figure 5.1a). To assess the electrical properties of these nanowires, Pt contacts were placed in the ends of the transverse leads via Ga^+ FIBID, joining the nanostructure with the Ti pads (Figure 5.1b).

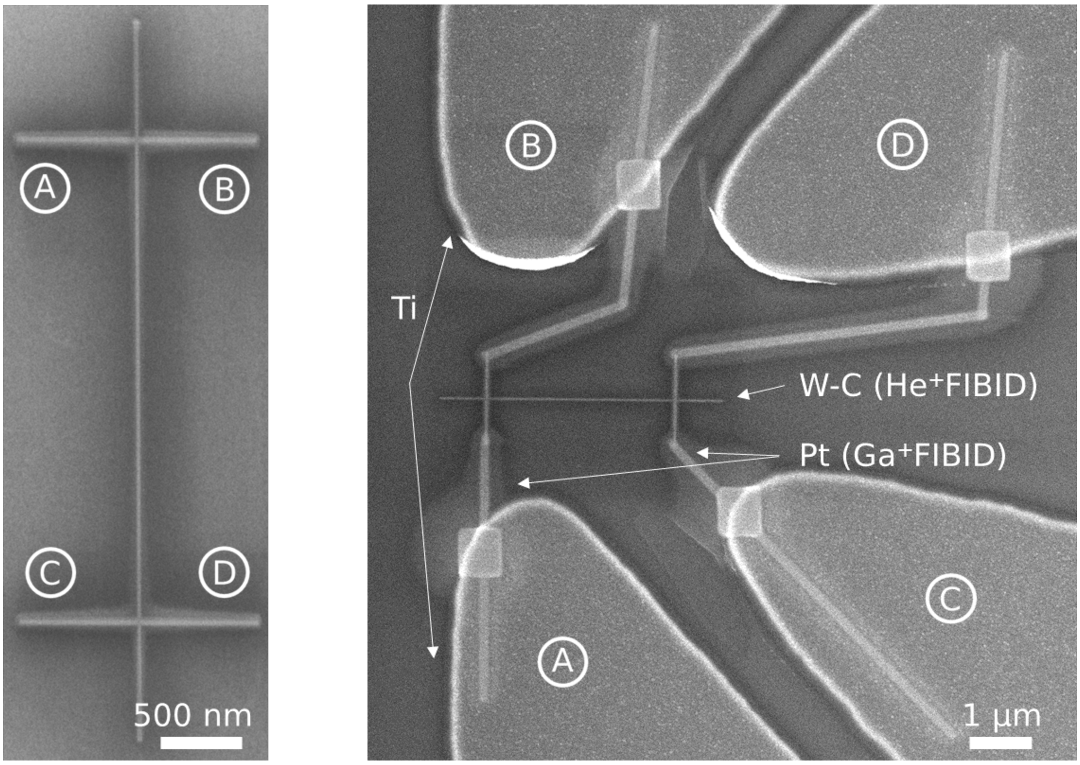

(A) Standard geometry.

(B) Contacted nanowire.

FIGURE 5.1: SEM images of W-C nanowires grown by He^+ FIBID. Labels A to D indicate the four electrical inputs and outputs used to carry out both the local and non-local voltage measurements.

5.2.2 Lateral resolution

The patterning capabilities of the procedure were explored by systematically modifying the nominal line width during the patterning procedure.

Using an ion beam current of 15 pA, a notable agreement between the nominal and the real line widths was found when the nanowires were grown using a dose of 0.7 nC/μm^2 (Figure 5.2a), achieving a lateral patterning resolution of 10 nm. Growing with a higher ion dose of 2.0 nC/μm^2 results in shape fidelity loss below 30 nm (Figure 5.2b).

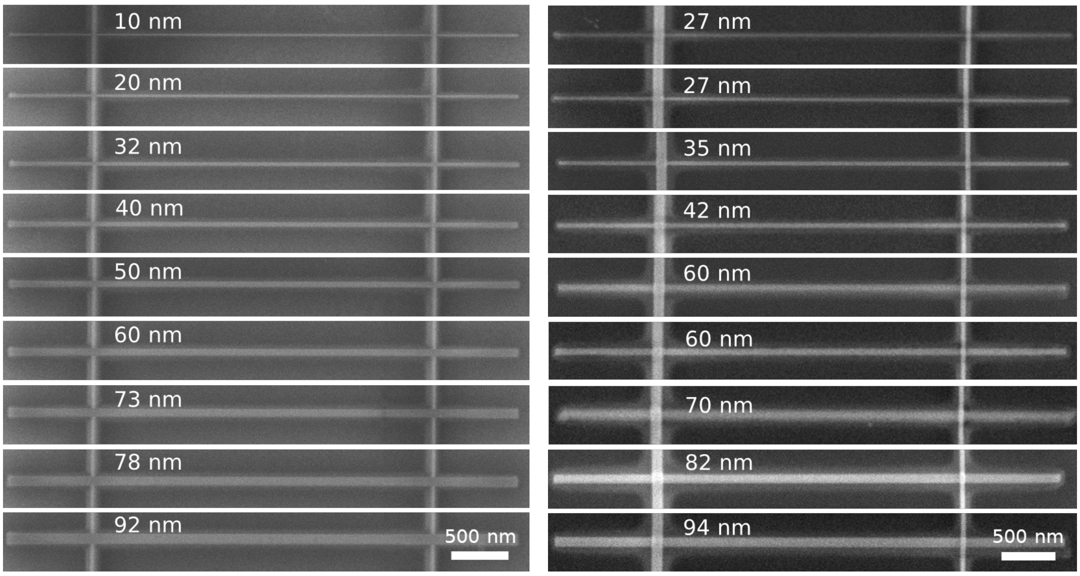

(A) 0.7 nC/μm^2.

(B) 2.0 nC/μm^2.

FIGURE 5.2: SEM images of W-C nanowires grown by He$^+$ FIBID to assess the shape fidelity study of line width. Each column depicts nanowires grown with increasing nominal width, starting from 10 nm up to 90 nm in steps of 10 nm. The real width (± 2 nm is indicated in each nanowire.

5.2.3 Composition

The ion beam current and dose both play paramount roles in the decomposition of the precursor material, thus determining the W/C ratio and, in turn, impacting on the superconducting properties of the deposits. To assess the effects of these two parameters, arrays of square-shaped deposits (Figure 5.3a) were grown at two fixed doses of 0.7 and 2.0 nC/μm^2, varying the ion beam current between 1 and 40 pA for each.

The chemical composition of each of these squares was then determined by SEM-based EDS. As evidenced by CASINO electron trajectory simulations, 3 kV electrons penetrate the material no further than roughly 200 nm, ensuring none of them goes through the whole 300 nm-thick SiO_2 layer, and thus ensuring that the oxygen signal coming from the substrate can be stoichiometrically separated from that coming from the sample.

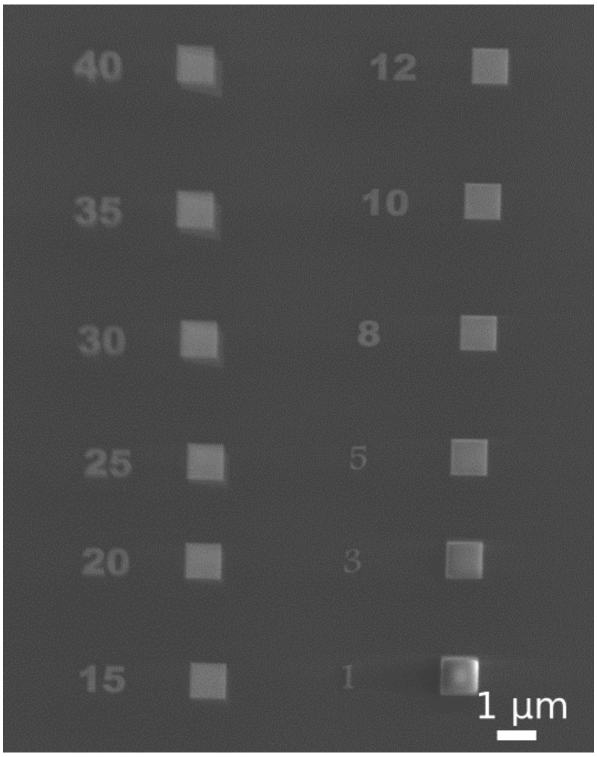

(A) 1×1 μm W-C squares grown with a dose of 2.0 nCμm^2 to assess the effect of the ion beam current on composition. The number patterned next to each square indicates the used current in pA.

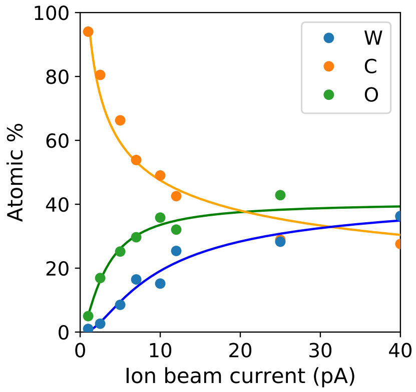

(B) Dose of 0.7 nC/μm^2.

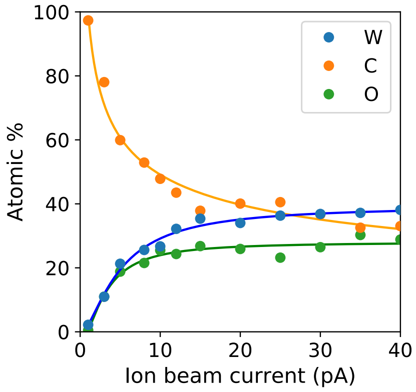

(C) Dose of 2.0 nC/μm^2.

FIGURE 5.3: EDS-based compositional study of He$^+$ FIBID W-C samples grown with doses of 0.7 and 2.0 nC/μm^2. Solid lines in plots 5.3b and 5.3c are a guide to the eye.

In both cases, the metallic content of the deposits increases with increasing ion beam current, following a saturation-like trend towards an atomic content of 40%, reasonably close to that of Ga$^+$ FIBID W-C, although lower than the maximum values reported for He$^+$ FIBID 3D nanostructures (Figures 5.3b and 5.3c). The increase in W atomic content is compensated by a sharp decrease in C content, which makes up close to 100% of the composition of the deposit at very low currents. A remarkable difference between the two assessed doses is that the amount of oxygen is significantly larger when the lower dose is used, it being more abundant than W within the whole assessed range. On the other hand, using a dose of 2.0 nC/μm^2 yields roughly the same amount of W than O below 7 pA, and always more metal than oxygen above.

The composition and microstructure of the nanowires were further evaluated by TEM-based studies, in a similar way as those performed in Ga$^+$ FIBID nanostructures (Figure 5.4). HRTEM images were taken to finely determine the thickness and width of the nanowires (the latter significantly differing from its "nominal" value extracted by SEM inspection, as usual), and the existence of two compositionally distinct regions or layers is evidenced by the sharp contrast present in STEM-HAADF images. The local composition on each of these areas was quantified by means of STEM-EDS.

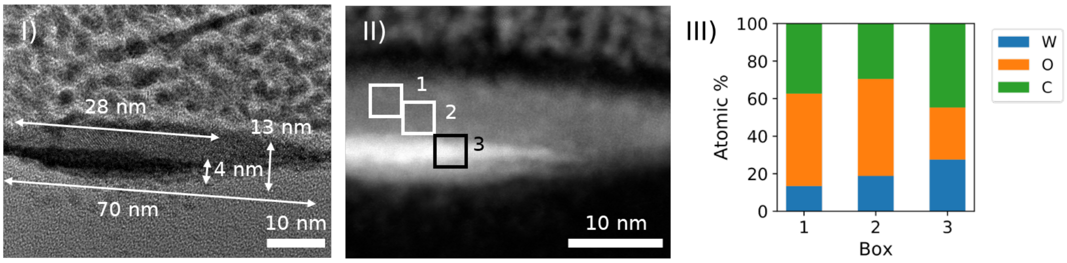

(A) 20 nm-wide nanowire grown with a dose of 0.7 nC/μm^2.

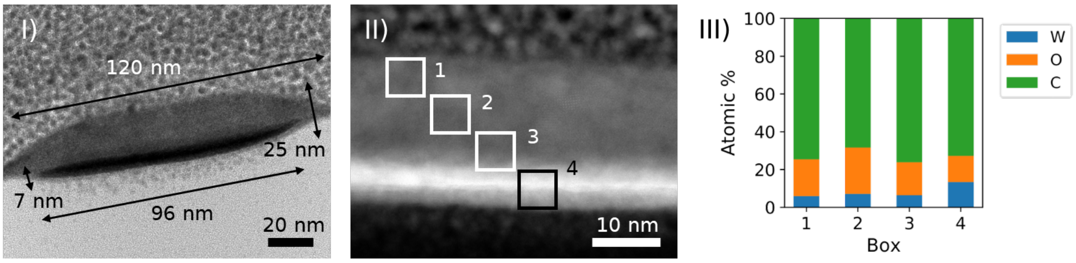

(B) 90 nm-wide nanowire grown with a dose of 0.7 nC/μm^2..

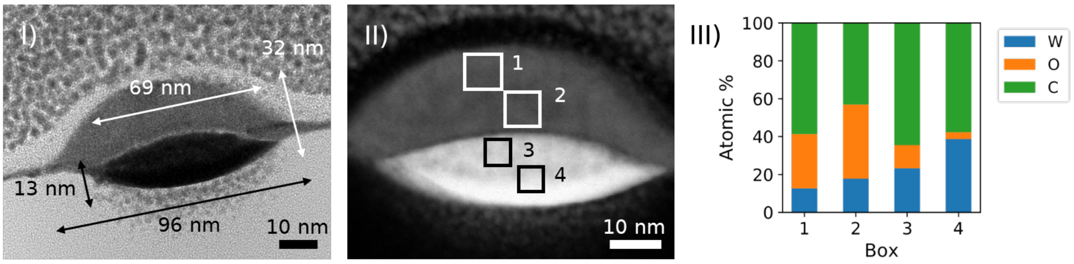

(C) 42 nm-wide nanowire grown with a dose of 2.0 nC/μm^2.

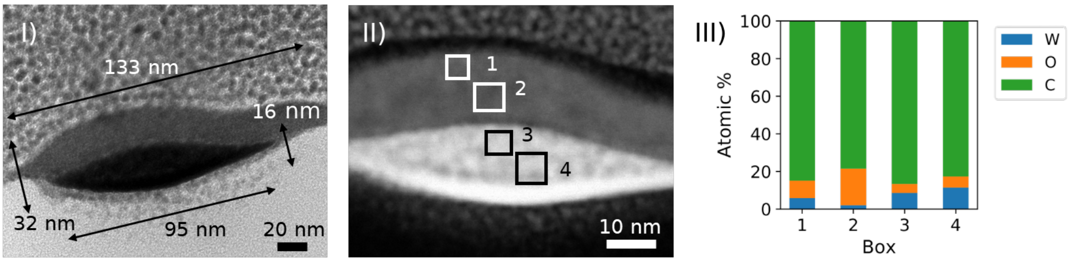

(D) 60 nm-wide nanowire grown with a dose of 2.0 nC/μm^2.

FIGURE 5.4: TEM compositional study of several He$^+$ FIBID nanowires. Each figure depicts: I) HRTEM image of the cross-sectional area; II) HAADF image of the same region; III) EDS quantification of the boxes labeled on the HAADF image.

The upper layer, lighter in contrast in the HAADF images, is an oxygen-rich region that most likely arises as a consequence of sample exposure to air. Although for this thesis, samples were always kept in vacuum conditions and their exposure to air was as (realistically) minimized as possible, in the specific case of He^+ FIBID, all of them did undergo a several hour-long trip from Dresden back to Zaragoza exposed to air. In future iterations of He^+ FIBID fabrication outside the local laboratory, extra protection measurements should be taken to minimize the impact of this oxidation[3].

The metallic layer, which is most likely the responsible for the electrical conduction, has a thickness within the 5-15 nm range. The ion dose is found to play a determinant role on its value, with the nanowires grown with 2.0 $nC/\mu m^2$ showing at least twice the thickness than their 0.7 $nC/\mu m^2$. The line width does not appear to influence thickness as much as the ion dose. In the localized STEM-EDS study, the metallic content does not follow a trend as clear as that evidenced in the "global" EDS SEM-based study, performed over the whole of 1×1 μm square deposits. In any case, the W atomic content falls within the 15-40% range in the metallic part, and below 10% in the oxidized layer.

Concerning crystallinity, HRTEM images depict the existence of short-range order in the form of nanocrystallites in the oxydized layer (Figure 5.5). The metallic layer is too dense to properly distinguish the existence (or lack thereof) of crystalline order. No clear crystallographic phases are detected.

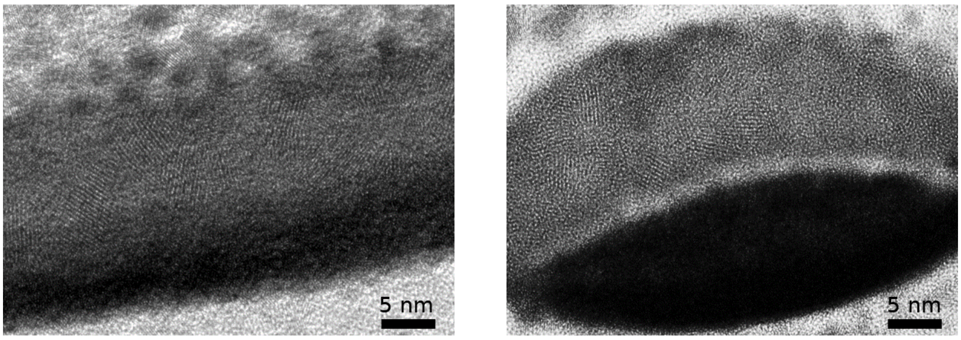

(A) 90 nm-wide nanowire grown with a dose of 0.7 $nC/\mu m^2$.

(B) 42 nm-wide nanowire grown with a dose of 2.0 $nC/\mu m^2$.

FIGURE 5.5: High-magnification HRTEM images of He^+ FIBID nanowires. Oriented atomic planes can be observed in the upper layer.

5.2.4 Local electrical characterization

The local voltage measurements were performed following the conventional procedure (Figure 2.11a, and referring to Figure 5.1, the driving current was injected

---

[3] All samples were exposed to air in this manner, including the squares utilized for assessing the impact of the current in the composition. Although they were not analyzed by TEM, it is possible that they underwent a similar oxidation process, and if that were the case, then the "real" oxygen content of non-oxidized samples would be lower.

from contact point A to contact point C, and voltage was measured between contact points B and D) in nanowires grown with an ion beam current of 15 pA, and with ion doses of 0.7 and 2.0 nC/μm^2.

At room temperature, the nanowires exhibited ohmic behavior with variable values of room-temperature resistivity, ρ_{300K}. The value of ρ_{300K} was estimated using a length value of 3 μm (*i.e.*, the distance between the voltage contacts only), and approximating the cross-sectional area of the nanowire to that of half an ellipse, using the information retrieved by TEM to define each semi-axis[4]. Samples grown with an ion dose of 0.7 nC/μm^2 exhibited values of ρ_{300K} within the 120-200 $\mu\Omega$·cm range, whilst those grown with a dose of 2.0 nC/μm^2 exhibited higher values, between 175-250 $\mu\Omega$·cm. In both cases, the resistivity increased with decreasing temperature up to a ratio ρ_{10K}/ρ_{300K} of around 1.1.

All measured nanowires with a nominal width of 20 nm or above exhibit a transition to the superconducting state induced by temperature, the value of which also depends on the ion dose used to grow the nanowires: within the 2.5-3.5 K range for those grown with 0.7 nC/μm^2; and between 3.7 and 4 K for those grown with 2.0 nC/μm^2 (Figure 5.6). The 10 nm-wide nanowire does not show superconducting behavior within the measured range, down to 0.5 K.

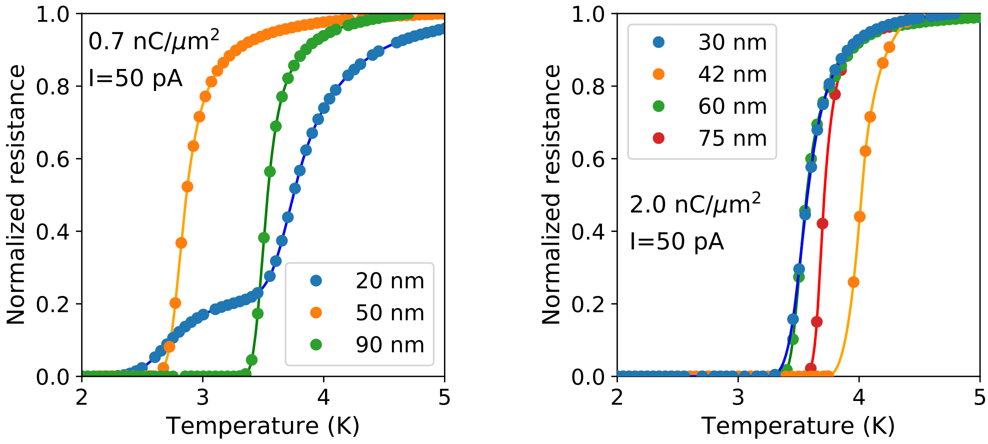

(A) Ion dose of 0.7 nC/μm^2.

(B) Ion dose of 2.0 nC/μm^2.

FIGURE 5.6: Temperature dependence of the normalized resistance for He$^+$ FIBID nanowires.

The value of the upper magnetic field, B_{c2}, was extrapolated by comparing the transition-inducing value of the field at different driving currents and temperatures, with data from the 60 nm-wide nanowire grown with an ion dose of 2.0 nC/μm^2

---

[4] As a note of caution, the local measurement performed on those samples is not strictly "four probe" since the opposite ends of the same leads are simultaneously used for the current and the voltage. While their contribution should not distort the results to a significant extent, at least a slight overestimation of the resistance in the normal state should be assumed.

(Figure 5.9 in next section) indicating an approximated, extrapolated value of B_{c2} between 8 and 9 T.

The relevant superconducting parameters, *i.e.*, the superconducting gap, coherence length, and penetration depth, can be deducted from the experimentally measured critical parameters following the equations presented in section 1.3, and are summarized in Table 5.1 in section 5.4, along with the retrieved values in comparable works performed by others.

Notably enough, in the narrow nanowire (20 nm-wide, dose of 0.7 nC/μm^2), the superconducting transition induced by temperature is constituted by two contributions, as the overlap of two independent transitions (Figure 5.6a). Examining the magneto-resistance dependence of that nanowire reveals a similar behavior when the transition is field-induced (Figure 5.7).

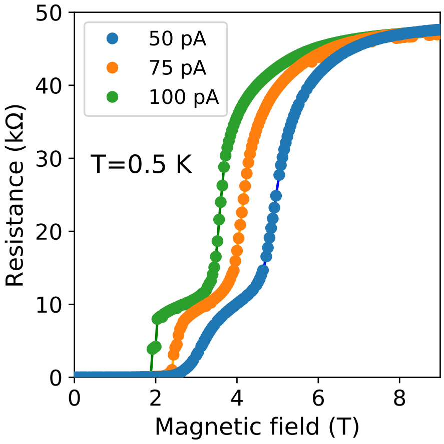

FIGURE 5.7: Local magneto-resistance on the resistance of the 20 nm-wide nanowire at different driving currents.

The occurrence of these two-step transitions can be related to the width of the nanowire not being perfectly homogeneous along the whole channel, with small constrictions that locally modify the critical temperature of the material. Since it is also experimentally found that 10 nm-wide nanowires do not exhibit superconductivity, it is not unreasonable to observe this effect in the narrowest nanowires only, which are nearing the width limit for superconductivity to occur, and as such are more sensible to geometrical inhomogeneities.

5.3 Long-range non-local vortex transport

5.3.1 Vortex motion driven by the Lorentz force

Most remarkably, He$^+$ FIBID W-C nanowires are found (for the first time) to be capable of sustaining long-range non-local vortex transport, similarly to their Ga$^+$ FIBID counterparts. Specifically, such a non-local signal was detected in the 90 nm-wide nanowire grown with a dose of 0.7 nC/μm^2 (Figure 5.8) and in the 60 nm-wide nanowire grown with a dose of 2.0 nC/μm^2 (Figure 5.9).

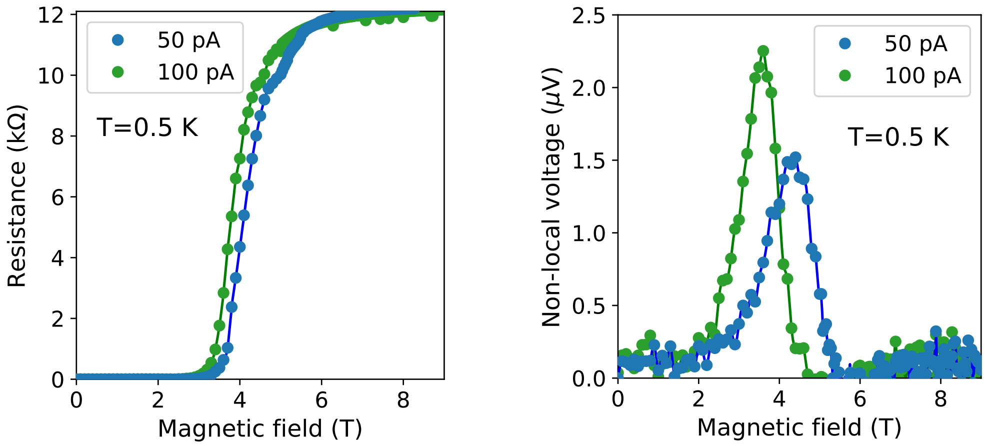

(A) Local magneto-resistance.

(B) Non-local magneto-resistance.

FIGURE 5.8: Magneto-resistance curves of the 90 nm-wide He$^+$ FIBID nanowire grown with a dose of 0.7 nC/μm^2. The observed non-local features are compatible with non-local vortex transport across the 3 μm-long channel.

The occurrence of this phenomenon is investigated following the same procedure previously described and already used for Ga$^+$ FIBID nanowires, making use of the geometry of the deposits to perpendicularly inject the driving current through one end, and measure the non-local voltage drop at the other, 3 μm away (Figure 2.11b, and once more referring to Figure 5.1, in non-local mode the driving current is injected from contact point A to contact point B, and voltage is measured between contact points C and D[5]).

When measuring in AC mode, the non-local magneto-resistance curves are in agreement with the expected Lorentz force-driven non-local vortex motion behavior (figures 5.8a and 5.8b. At a given temperature, T, as the magnetic field is increased, a transition to the normal state is detected in local mode at the corresponding value of $B_{c2}(T)$. In the vicinity of that point, a finite voltage signal is detected in the non-local configuration, in an area of the nanowire depleted of current. The magnitude of that signal increases with increasing magnetic field up to a maximum, at which it monotonically decreases and returns to zero. No other nonzero signals are detected within the explored range (0-9 T). Increasing T brings the nanowire closer to the normal state, which in turn reduces the corresponding value of $B_{c2}(T)$. As a consequence, both the field-induced transition and the position of the non-local voltage

---

[5] Contrary to the previously described local measurement, the geometry of the deposit now does qualify this experiment as "true" non-local configuration.

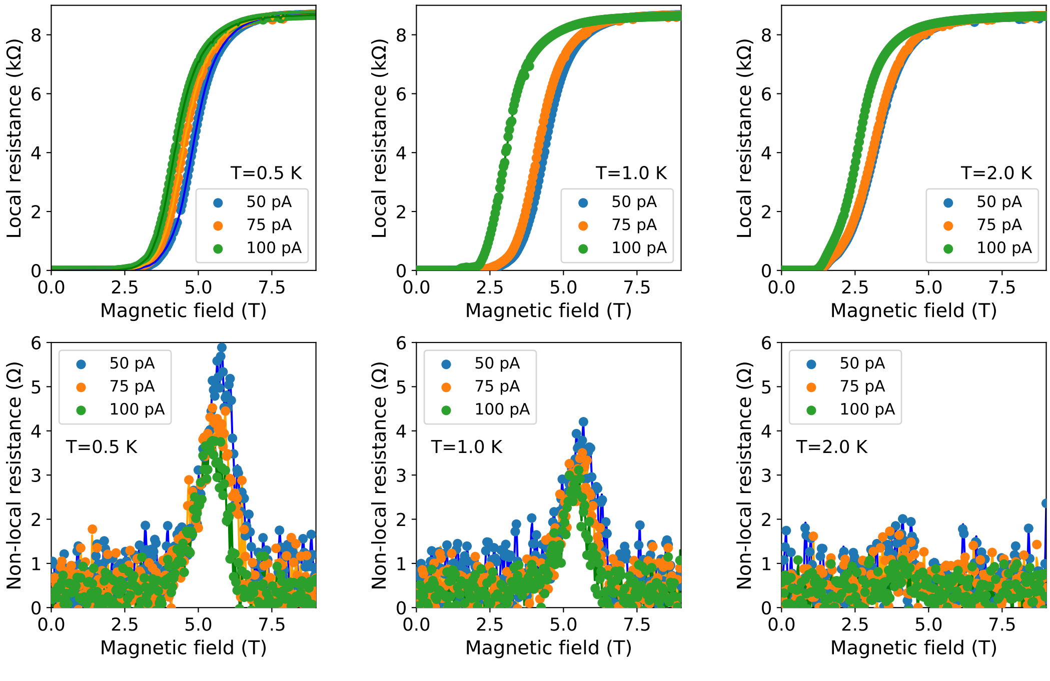

(A) $T = 0.5$ K. (B) $T = 1.0$ K. (C) $T = 2.0$ K.

FIGURE 5.9: Local (up) and non-local (down) magneto-resistance curves of the 60 nm-wide He$^+$ FIBID nanowire grown with a dose of 2.0 nC/μm^2 at different temperatures. The observed non-local features are compatible with non-local vortex transport across the 3 μm-long channel.

peak are shifted towards lower values of magnetic field. In addition, since the vortex density at which the transport phenomenon occurs is effectively reduced as the temperature is increased, the absolute value of the non-local peak also gets reduced as the temperature increases, down to zero at higher temperatures close to T_c (no measurable transport). Overall, these features are compatible with a Lorentz force exerted by the driving current on the current lead pushing or pulling the vortices along the 3 μm-long channel, therefore confirming the capability of He$^+$ FIBID W-C nanowires to sustain long-range non-local vortex transport for the first time.

The previously presented discussions on Lorentz force-driven non-local vortex motion, both generically (section 1.3.5) and applied to the experimentally detected vortex transport in Ga$^+$ FIBID W-C nanowires (section 3.3) fully hold for the case of He$^+$ FIBID, and will not be repeated here.

It is worth remarking, however, that not all geometries studied are capable of hosting vortices. Recalling the approximation to the vortex-entrance field [107], some of the nanowires presented here are simply to narrow to host any vortices below their upper critical field. The 20 nm-wide nanowire presents an entrance value of $B_m \sim 5$ T, above its corresponding critical field at the measured temperature - the nanowire is already normal when it reaches the field at which vortices would enter. 60 nm and 90 nm-wide nanowires present much lower values of B_m, around 0.6 and 0.2 T, respectively, on which the nanowire is still superconducting, and as such, vortices do indeed enter the material.

5.3.2 Vortex motion at high currents

In addition to the presented results, an intriguing non-local phenomenon is only observed when measuring in DC mode. Using high values of driving current (above its critical value I_c), a finite non-local voltage peak appears in the vicinity of 5 T (Figure 5.10). Significantly greater in magnitude that the previously described peak, associated to Lorentz force-driven vortex transport, the absolute value of this feature increases with increasing current, and it is slightly asymmetrical with respect to the field, enhanced for negative values of this parameter.

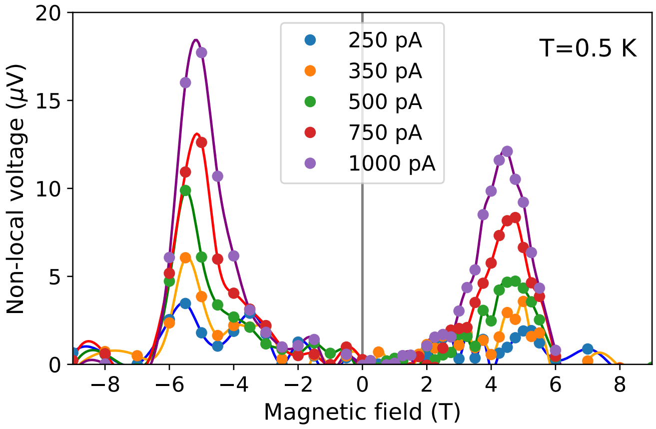

(A) Positive excitation.

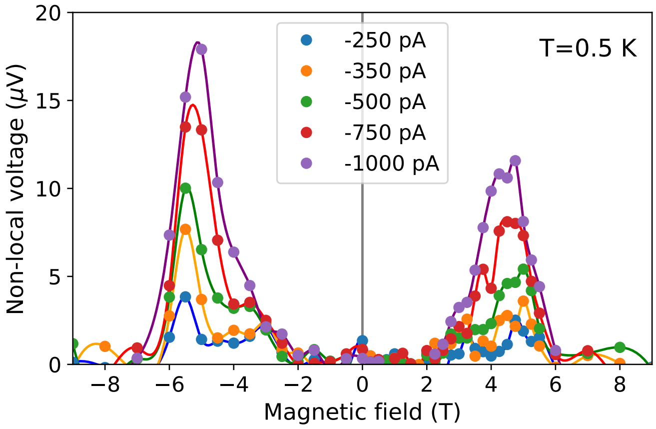

(B) Negative excitation.

FIGURE 5.10: High-current, non-local magneto-resistance curves measured in DC mode for the 90 nm-wide nanowire (dose of 0.7 nC/μm^2. The observed features are not compatible with the Lorentz interpretation for vortex motion.

To properly assess the significance of these data, it is worth revising how the sign of non-local voltage translates to vortex motion. A fundamental feature of Faraday's law (equation 1.9) is the following: associating a sign of non-local voltage with a direction of motion for the vortices *also depends on the sign of the magnetic field*. In the PPMS configuration, the magnetic field is taken to be positive when its directed towards the substrate *from above*, *i.e.*, directed towards the sample from the reader's view in Figure 5.1. In this configuration, and with the driving current flowing from A to B in that figure, non-local voltages signify vortex motion as follows:

- For positive values of the magnetic field, a *positive* non-local voltage indicates vortex motion *towards* the current lead.
- For positive values of the magnetic field, a *negative* non-local voltage indicates vortex motion *away* from the current lead.

As per Faraday's law, these relationships are reversed if the sign of the magnetic field is reversed as well, *i.e.*, for negative values of the magnetic field, positive/negative voltages indicate motion away from/towards the current lead, respectively.

On that basis, and assuming that the signal presented in Figure 5.10 is due to vortex motion, the observed phenomenon consists in vortex motion towards the current lead for positive fields, and away from it for negative fields. The direction of motion is notably independent of the sign of the current.

The key factor that puts the Lorentz hypothesis in check is precisely this independence of the sign of the current. While for the positive cycle of the excitation current the signs of the non-local voltage match the expected direction of motion for the vortices (section 1.3.5), they certainly do not for the negative cycle, since changing the sign of the current would imply also changing the direction of motion (equation 1.10)[6].

These features appear for values of magnetic field *higher* than its observed critical value, B_{c2}. It must be kept in mind that, contrary to the local measurement, in the non-local configuration the driving current is applied to one of the leads *only*. As such, the current-depleted regions of the nanostructure (including the long axis of the nanowire) undergo the transition to the normal state "later", *i.e.* when the corresponding experiment parameter is further increased (in this case, the magnetic field), since the transition in these current-free areas is induced by that parameter only and is not being aided by the driving current (as it happens in the local measurement and in the current lead).

---

[6] This independence on the sign is also the reason these features are effectively undetectable in AC mode: the PPMS instrument used to measure magneto-resistance presents output in the form of ohmic resistance, as described in section 2.3. In AC mode, data points are pre-processed by averaging readings on which the sign of the current is switched. If the sign (and value) of the voltage remains independent of the current, these readings will have roughly equal values and opposite sign, and the averaging will yield results close to zero. As a consequence, this feature is "invisible" in AC mode.

The asymmetry in the maximum values by the peaks suggests the presence of two contributions to the signal, symmetric and antisymmetric in nature with respect to B. The full signal can be separated into these two constituents as per

$$V_{\pm}(B) = \frac{V(B) \pm V(-B)}{2} \tag{5.1}$$

where $+$ and $-$ denote the symmetric and antisymmetric parts of the signal, respectively (Figure 5.11).

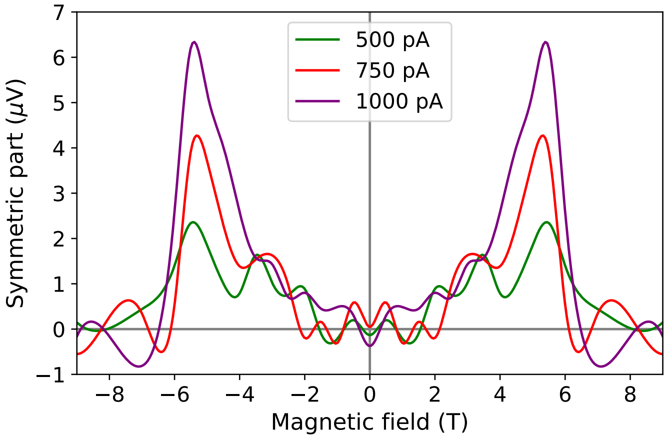

(A) Symmetric part.

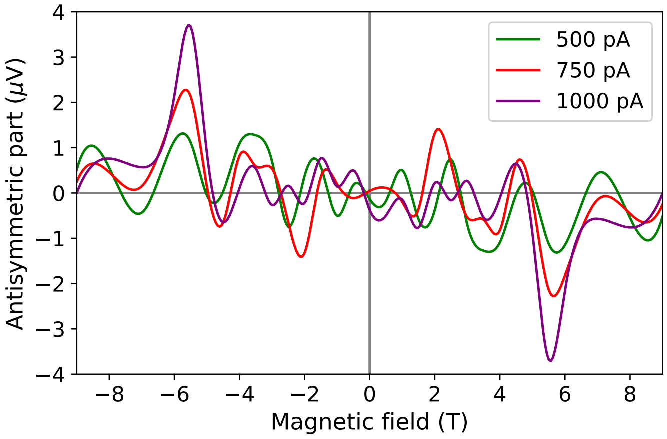

(B) Antisymmetric part.

FIGURE 5.11: Separation into symmetric and antisymmetric constituents of the non-local magneto-resistance voltage signal retrieved at high values of positive driving current. For clarity, only the highest values of I are shown. The decomposition for $I < 0$ is similar.

The signal can thus be interpreted as the sum of two independent effects that regulate vortex motion. Both are independent of the sign of the current, and peak in magnitude near the extrapolated critical value of the magnetic field at zero current.

The antisymmetric contribution indicates motion of the vortices always *away* from the current lead, independently of the sign of the current or of the field. This trend is compatible with a thermal phenomenon related to the *Nernst effect*, which has been experimentally shown to be able to move vortices in a similar fashion as a driving current does in working temperatures away from T_c [41, 108, 109]. Local heating induced by the injected (high) driving current results in the appearance of a thermal gradient within the superconducting channel, whose effect is modelled in terms of a thermal force that pushes vortices *down* the temperature gradient, towards colder regions. This phenomenology is compatible with the antisymmetric part of the signal, on which it is observed that motion always occurs away from the (hot) current lead, independently of the signs of the current and the field.

Concerning the symmetric part, a justification for its behavior is still pending at the time of writing. Geometrically, the non-local features are compatible with a magnetization buildup phenomenon occurring in the vicinity of T_c [108, 109], but its origin, a shrinkage of the vortex core, is not compatible with the driving force for the just-described Nernst effect, which occurs precisely due to vortex core expansion at low temperatures. This description, however, provides insight on how magnetic-field dependent forces other than the Lorentz force can induce vortex motion compatible with the observed data, and it should be kept in mind for following studies. Further investigation on the matter is planned in a near future.

5.4 Conclusions

The relevant superconducting parameters extracted from this study are presented and compared to previous work in Table 5.1. The retrieved results are reasonably close to those retrieved by Basset *et. al* in long in-plane He^+ FIBID W-C nanowires, with the present study finding a somewhat more "fragile" superconduтivity, with the critical values of temperature and critical current slightly below those reported by Basset. On the other hand, the differences are definitely pronounced when comparing them to those from Córdoba *et al.* in 3D He^+ FIBID nanowires. The critical temperature, metallic content, and upper critical magnetic field are certainly lower in the present in-plane nanowires than in their 3D counterparts.

As anticipated, these disagreements in parameter values are not unreasonable, taking into account the significant differences that do exist between the two growth mechanisms. While in-plane FIBID is mostly driven by first order SEs, in 3D growth these SEs are used to drive vertical growth, while second-order SEs (induced by scattered ions, rather than by the primary beam) which control lateral growth, are also "exploited" [110, 111]. Out-of-plane growth is achieved by accurately finding a fine balance between material milling and deposition above the previously deposited material. This requirement is simplified in in-plane growth, where, within reasonable values of the operating parameters, growth is mostly guaranteed in the

	Present work	2D He$^+$ FIBID[106]	3D He$^+$ FIBID[74, 105]
W atomic content	20-30%	-	Up to 70%
ρ_{300K} ($\mu\Omega\cdot$cm)	110-240	80-260	398-464
T_c (K)	2.5-4	4-6	6.2-7.1
B_{c2} (T)	8	>5	12.1-15.3
J_c (MA/cm^2)	0.12-0.46	0.25-0.86	0.09-0.23
ξ (nm)	6.4	6.7-7.6	4.64-5.22
λ (nm)	616-812	400- 674	603 – 902

TABLE 5.1: Comparison between the relevant parameters of He$^+$ FIBID W-C retrieved in the present work and those previously reported by others.

electron-limited regime. In the present case, in-plane He$^+$ FIBID of W-C is found to yield a volume per dose of around $3\cdot 10^{-3}$ μm^3/nC, one order of magnitude below that of 3D He$^+$ FIBID and Ga$^+$ FIBID.

The presented results provide with meaningful insight concerning the potential and applicability of HIM for the fabrication of W-C based superconducting devices. First, a detailed growth and characterization report is presented, which can be used as a reproducible protocol for future fabrication of similar nanostructures.

Second, it has been experimentally confirmed that in-plane material yielded by the He$^+$ FIB induced deposition of W(CO)$_6$ is indeed superconducting, and presents properties that are reasonably close to those of Ga$^+$ FIBID W-C despite the complete lack of implanted Ga, and the reduced substrate amorphization. While it may result naive to directly rule out the presence of Ga as the origin for the superconductivity in Ga$^+$ FIBID, the present study show that it is, at least, not the *sole* reason of the occurrence of the phenomenon.

Third, the enhanced patterning capabilities of HIM open the door towards patterning more complex and delicate structures than those achievable using Ga$^+$ FIBID. For instance, it has been experimentally found that superconductivity in these He$^+$ FIBID W-C nanowires starts to crumble between 10 and 20 nm, in agreement with the projected values of ξ around 6-7 nm. Since it has also been shown that 10 nm-resolution is achievable with reduced ion doses, patterning of complex nanostructures with variable width is readily foreseeable. For instance, Dayem bridge-based devices could be fabricated by patterning a constriction with width around 10 nm, which would remain normal while the surrounding bulk maintains the superconducting state, enabling for Josephson junction transport behavior that can be practically exploited (*e.g.* for designing nanoSQUIDs).

Fourth, He$^+$ FIBID nanowires have been shown to be capable of hosting long-range non-local vortex transport as adequately as their Ga$^+$ FIBID W-C counterparts do. The same outlook already presented for the applicability of vortex-based Ga$^+$ FIBID nanodevices holds for those fabricated with He^+ ions, with the evident added value of enhanced patterning capabilities that HIM provides.

Lastly, a previously overlooked non-local phenomenon has been observed. Hypothesis concerning thermal and magnetization effects occurring at high values of driving current have been presented. Its occurrence is left indicated as both an open question and a note of caution for future similar measurements.

Chapter 6

Summary, conclusions and outlook

In this chapter, a summary of the work performed on each of the three research lines presented in this thesis, as well as a round-up of the conclusions and potential prospective research interested are presented.

6.1 Ga^+ FIBID of superconducting W-C nanostructures

As already discussed in Chapter 3, the growth of the superconducting W-C material via (conventional) Ga^+ FIBID is a mature, well-explored field of study at the present time. The three lines of work presented in this thesis represent a series of steps taken near the boundaries of the present-day knowledge, providing with insight on the possible advanced functionality of FIB-patterned superconducting nanostructures.

6.1.1 Non-local vortex transport

Building mostly on the initial ideas seeded by Irina Grigorieva *et al.* [44] and further expanding the previous research on non-local vortex transport on Ga^+ FIBID W-C carried out by Rosa Córdoba *et al.* [42, 76], the non-local vortex transport of superconducting vortices in narrow W-C nanowires has been investigated. By perpendicularly injecting a driving current through one end of the nanostructure and measuring the voltage drop at the other, it is possible to detect finite non-local resistances in areas of the nanostructure depleted of current, solely caused by the motion of passing superconducting vortices.

Yielding non-local equivalent resistances up to 8 Ω, these results represent, at the time of writing, the furthest reported value of Lorentz-driven vortex motion in this manner in a 50 nm-wide, 10 μm long W-C nanowire. They strengthen the hypothesis of vortex confinement in narrow superconducting channels as a powerful enhancer for the efficiency of pressure transfer, confidently establishing Ga^+ FIBID as a suitable technique for the deposition of more complex, vortex transport-based superconducting nanodevices.

Local control of vortex motion already finds application in functional superconducting nanodevices as logic gates [112], quantum switches [113], and single-photon detectors [114]. Considering non-local transport, vortices are appealing candidates to act as quantized information bits in the design of memory cells, exploiting their quantized nature and treating each enclosed magnetic flux quantum as the basic unit of information in a superconducting nanocircuit [115–118]. With the flexibility and ease of access that Ga^+ FIBID, the presented results lay another sturdy paving stone in what already strikes as a promising path.

6.1.2 STM study

In collaboration with the Amelia Domínguez and David Serrate, from the University of Zaragoza, preliminary work on the investigation via STM of superconducting W-C films grown by Ga^+ FIBID has been performed. An accessible procedure for the preparation of both the substrate and sample itself has been developed.

By means of STS, images of the lattice of superconducting vortices in a W-C film have been retrieved, in a similar fashion as those already reported by Isabel Guillamón *et al.* [58, 59, 73, 75, 81]. The retrieved results are in good agreement with the reported values in the literature and with other experiments on Ga^+ FIBID W-C concerning superconductivity presented here[1].

With the (superconducting) board now set, pieces can start moving. Following similar arguments to those presented in the discussion presented on the "perturbing" and "unwanted" nature of superconducting vortices, whose motion taints the otherwise pristine superconducting state, intriguing physical phenomena can be investigated if disorder is locally introduced in the superconducting state via magnetic impurities. Such is the case of the *Yu-Shiba-Rusinov states* - localized bound states that appear within the superconducting gap as a consequence of coupling between an external magnetic spin[2] with a superconductor [83]. These have been successfully detected using different spin-superconductor combinations [119, 120], and could also potentially emerge when using Ga^+ FIBID W-C as the framework.

In a similar vein, the investigation of molecular-scale *Bitter effect* (also named *magnetic decoration*, akin to that performed to obtain the first direct images of the vortex lattice [36]) also represents an exciting research prospective: while the conventional technique uses ferromagnetic powder or the like to image the magnetic field distribution of a material [82, 121], controlled deposition of magnetic spins over the superconducting surface could also lead to interesting results. Experiments in search

---

[1] They also provide with an actual "picture" of the almost-omnipresent vortices that act as one fundamental pillar on this thesis, somewhat making them less obscure to those unfamiliar with them.

[2] That is, a molecule or an atom with net magnetic moment, such as Cr or Co atoms.

for the detection of these states and phenomena, using Co atoms as magnetic spins, over whose control David Serrate *et al.* have achieved notorious skill [122], can be considered.

6.1.3 Field effect

The recently published work by Federico Paolucci *et al.* provides with extremely valuable insight on a previously overlooked phenomenon - the possibility of fabricating field-effect transistor-like devices based on superconducting materials, on which a modulation of the critical current is achieved via the application of an external gate voltage. Namely, their results indicate successful detection of such an effect in different superconducting materials [84], including titanium [49, 51, 52], aluminium [89], vanadium [90], and niobium [91].

In this work, the fabrication and experimentation on such S-FET devices based on the W-C material grown via Ga^+ FIBID has been explored for the first time, making use of gating electrodes patterned by electron beam lithography. The results indicate the occurrence of field effect within a voltage range of 0 to 3 V, on which the critical current of the nanowire is progressively suppressed. The experimental results are in good agreement with the expected trends, and the absolute values of the figures of merit and characteristic parameters fall within the range of other reported materials, with a reasonably high value of T_c (expected for Ga^+ FIBID W-C, but above of other superconductors used for this purpose), and with complete I_c suppression achieved at relatively low values of V_g.

Uniquely, the growth procedure used here provides with ample flexibility in the design and growth of the patterns, enabling for the growth of more complex and targeted nanostructures. The viability and occurrence of this kind of field effect in the Ga^+ FIBID W-C material thus places it on the forefront towards its implementation in the fabrication of advanced functional S-FET nanodevices.

6.2 Cryo-FIBID of W-C metallic nanostructures

FIBID in cryogenic conditions, or Cryo-FIBID, is a nanopatterning technique developed and patented by José María De Teresa, Rosa Córdoba, Stefan Strohauer, and Teobaldo Enrique Torres in 2018 [100]. By cooling down the substrate below the condensation temperature of the precursor, a thick layer of condensed precursor forms on top of the substrate, allowing for much faster deposition of the material than that achieved with the single molecular monolayer that is achieved at room temperature.

The work presented in chapter 4 is the experimental follow-up on the development of the Ga^+ Cryo FIBID - with the initial conditions having already been laid out and optimized by previous work, here further research on the capabilities and applicability of the technique is presented, including: studies on the composition and microstructure of the deposits, investigation of the electrical properties, dependence of the growth procedure on the ion dose and precursor temperature, and fabrication of proof-of-concept targeted nanostructures.

With single-nanowire deposition times ranging in the order of ms, Cryo FIBID increases the growth speed up to three orders of magnitude in comparison to room-temperature FIBID, achieving comparable resolution, although with the occurrence of finite-size effects in the form of a wing-like halo that surrounds the deposit. Remarkably, the deposits are not superconducting like their counterparts grown at room-temperature, although they do exhibit ohmic-like behavior and thus can be used as supporting contacts for electrical measurements of other samples.

Coupled with the flexibility and single-step, resist-free nature of FIBID, the enormous increase of processing speed that Cryo FIBID provides makes it a highly attractive technique for material growth, putting it in a competitive position near comparable deposition techniques (Figure 6.1), for the low dose it requires makes it one of the fastest.

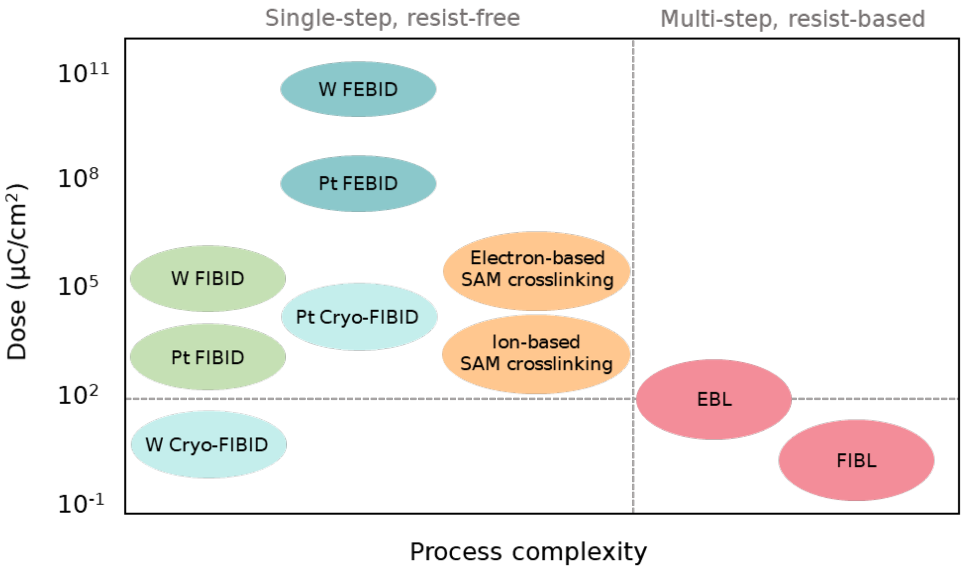

FIGURE 6.1: Charged-particle based lithography techniques arranged by dose required and process complexity (SAM: Self-Assembled Monolayer, EBL: Electron Beam Lithography, FIBL: Focused Ion Beam Lithography) [101].

As such, Cryo FIBID is bound to see further developments in the near future, either in the form of expanding its applicability to tasks similar to those performed by conventional FIBID, such as circuit edit or mask repair, or undergoing further experimentation on the nature of the technique itself, assessing its performance using different substrates, precursor materials, and ionic species to carry out the growth.

6.3 He$^+$ FIBID of W-C superconducting nanostructures

The results and discussion presented in Chapter 5 refer to the deposition of in-plane W-C nanowires by He$^+$ FIBID. While Ga$^+$ FIBID of this material is exhaustively reported, a systematic study on the growth of in-plane nanostructures via He$^+$ FIBID was notably lacking from the literature at the time of writing.

While Ga$^+$ FIBID is arguably more accessible and studied than He$^+$ FIBID, the latter provides with very significant advantages over the former - namely, enhanced lateral resolution, reduced substrate amorphization, and absence of metal implantation. The first is of particular importance in the design of nanodevices, even more so when exploring finite size effects such as vortex transport in narrow channels.

In this thesis, deposition of W-C nanowires with lateral size down to 10 nm has been achieved. They have been shown to exhibit superconducting behavior when patterned with widths above 20 nm, with size-dependent values of T_c in the 2.5-4 K range. The characteristic superconducting parameters are comparable to those of comparable nanodevices [106] and 3D nanostructures [74, 105], more so to the former. In addition, the capability of the nanostructures to sustain vortex transport (similarly to the study carried out in Ga$^+$ FIBID nanowires) has been successfully shown in 3 μm-long nanowires for the first time.

The labor performed on this matter provides with valuable insight on the capabilities and applicability of this technique for purposes comparable to those Ga$^+$ FIBID is dedicated, with the added values that using a HIM provides. Particularly in the field of vortex transport and finite-size effects, the fact that the material maintains its superconducting properties favors its applicability for the fabrication of devices that so require it.

6.4 Publications

The following works have been published during this thesis:

- Rosa Córdoba, Pablo Orús, Željko L. Jelić, Javier Sesé, Manuel R. Ibarra, Isabel Guillamón, Sebastián Vieira, Juan José Palacios, Hermann Suderow, Milorad V. Milosević and José María De Teresa. "Long-range vortex transfer in superconducting nanowires". In: *Scientific reports* 9.12386 (2019). DOI: 10.1038/s41598-019-48887-7.
- Rosa Córdoba, Pablo Orús, Stefan Strohauer, Teobaldo E. Torres and José María De Teresa. "Ultra-fast direct growth of metallic micro- and nano-structures by focused ion beam irradiation". In: *Scientific reports* 9.14076 (2019). DOI: 10.1038/s41598-019-50411-w.
- José María De Teresa, Pablo Orús, Rosa Córdoba and Patrick Philipp. "Comparison between Focused Electron/Ion Beam-Induced Deposition of Room

Temperature and under Cryogenic Conditions". In: *Micromachines* 10.12 (2019), p. 799. DOI: 10.3390/mi10120799.

- Pablo Orús, Rosa Córdoba, Gregor Hlawacek and José María De Teresa. "Superconducting properties of in-plane W-C nanowires grown by He^+ Focused Ion Beam Induced Deposition". In: *Nanotechnology* 32.8 (2020). DOI: 10.1088/1361-6528/abc91c.
- Pablo Orús, Rosa Córdoba and José María De Teresa. "Focused Ion Beam Induced Processing", in *Nanolithography techniques and their applications*, ed. José María De Teresa. Bristol: Institute of Physics (IOP), 2020. ISBN: 978-0-7503-2606-3. DOI:10.1088/978-0-7503-2608-7.

In addition, the publication of two additional works is to be expected in the near future: one relating to the field effect observed in superconducting W-C nanostructures for the first time, and other concerning the proximity effect and lateral patterning resolution in the growth of W-C nanostructures via Cryo-FIBID.

6.5 Concluding remarks

Leaving aside the (at this point overlooked) fact that having the capability to surgically draw with a nanometer-sized pen-like entity is sort of a mind-blowing achievement just by itself, the field of nanomanufacturing represents one of the most inciting research fields that science has to offer at the present day. Providing ample playground to both perform fundamental research and applied fabrication of functional nanodevices, it is undoubtedly bound to see even more exciting discoveries in the near future.

FIBID of W-C in the various conditions described here can serve as a solid cornerstone in the fabrication of targeted nanostructures that exploit the superconducting properties of Ga^+ and He^+ FIBID W-C, or the lightning speed provided by Cryo FIBID, among others. In addition, the achieved non-local vortex motion of superconducting vortices does also exhibit the potential to play a role in information transfer and storage. The research and insight presented in this thesis will further fill the sails of these research efforts, whose full realization should hopefully loom in the near future.

Appendix A

Resumen y conclusiones

This appendix contains a summary of the work performed in this thesis in the Spanish language.

A.1 Introducción

A.1.1 Crecimiento inducido por haz iónico focalizado

Un método particularmente versátil y conveniente para la nanofabricación de nanoestructuras funcionales es el *crecimiento inducido por haz iónico focalizado* (FIBID). Este proceso se lleva a cabo en la cámara de vacío de un instrumento dedicado, típicamente un haz iónico focalizado (FIB) o un microscopio de doble haz, fundamentalmente consituido por un FIB y una columna de electrones similar a la de un microscopio electrónico de barrido (SEM).

La técnica se basa en la descomposición local de un material precursor a partir de la energía proveída por el haz, en la mayor parte de casos constituido por iones de galio (Ga^+) o de helio (He^+). En un proceso convencional, este material se introduce en la cámara de proceso en fase gaseosa mediante un sistema de inyección de gases, consistente en una aguja situada cerca del sustrato. En equilibrio dinámico con el vacío de la cámara, una inyección constante de material precursor gaseoso resulta en la formación de una monocapa de moléculas de precursor adsorbidas sobre la superficie del sustrato.

Al escanear el FIB por encima de la superficie del sustrato, trazando el patrón correspondiente al depósito que se requiere, éste induce reacciones de descomposición en las moléculas de precursor allí adsorbidas. Concretamente, la disociación se produce mediante la transferencia de energía de electrones secundarios a las moléculas de precursor, siendo éstos emitidos por el sustrato como consecuencia de la irradación del FIB. Las moléculas de precursor se disocian en constituyentes volátiles y no volátiles: los primeros son expulsados de la cámara por el sistema de vacío, y los segundos se quedan permanentemente depositados encima del sustrato, constituyendo el depósito.

El crecimiento de nanoestructuras basadas en tungsteno (W) mediante la descomposición del precursor hexacarbonilo de tungsteno ($W(CO)_6$) por Ga^+ FIBID es de particular interés, ya que el material resultante presenta superconductividad de tipo II cuando se encuentra a temperaturas inferiores a 4.5 K. En esta tesis, se exploran distintas variaciones y aplicaciones de la técnica de crecimiento por FIBID, así como distintos fenómenos relacionados con la superconductividad de los depósitos que se obtienen con ella.

A.1.2 Superconductividad

La superconductividad es un estado electrónico de la materia, propio de diversos materiales (típicamente metálicos), caracterizado por una conductividad perfecta: por debajo de una temperatura crítica, el material presenta resistencia nula al paso de la corriente eléctrica, sin dispación de ningún tipo. Esta fase se encuentra limitada por los valores de temperatura, campo magnético, y corriente eléctrica a los que se ve sometido el material: incrementar alguno de ellos por encima de un valor crítico, que depende del material y del valor de los otros dos parámetros, devuelve al material al estado normal.

La conductividad perfecta se traduce también en la expulsión de las líneas de flujo magnético del interior del material, ya que, en ausencia de disipación, se generan supercorrientes en la superficie del material que apantallan su interior de campos magnéticos externos. Esta expulsión de líneas de flujo del interior del material se conoce como *efecto Meissner*. No obstante, algunos materiales superconductores, denominados *de tipo II* (en contraste con los descritos hasta ahora, considerados *de tipo I*) permiten una penetración ordenada y cuantizada de las líneas de flujo magnético en su interior bajo ciertas condiciones de temperatura, corriente, y campo magnético.

Esta penetración ordenada se corresponde con una fase dentro del estado superconductor, llamada *estado mixto*. Una solución de las ecuaciones de Ginzburg-Landau, que describen la superconductividad desde el punto de vista macroscópico, propuesta por Abrikosov, indica que el estado de mínima energía del sistema se corresponde con una red periódica, normalmente triangular, de pequeñas regiones normales a través de las cuales el flujo magnético atraviesa el material. Estas entidades, llamadas *vórtices superconductores*, son esencialmente una región tubular no superconductora, apantallada del resto del volumen superconductor por una supercorriente circular, a través de la cual el campo magnético atraviesa el material. La cantidad de flujo que atraviesa cada vórtice está cuantizada y depende únicamente de constantes físicas (*cuanto de flujo*).

Cuando se inyecta una corriente en un material superconductor en el estado mixto, la interacción entre los portadores de carga de éstas y las supercorrientes que rodean a los vórtices resulta en la aparición de una fuerza de Lorentz entre la corriente y éstos. Como consecuencia, los vórtices se mueven en respuesta a la inyección de una corriente siguiendo una dirección perpendicular tanto a la corriente como al campo magnético que los genera. El movimiento de los núcleos normales de los vórtices se traduce en la aparición de disipación en el estado superconductor, y como tal, típicamente se prefiere o se intenta que éstos se muevan lo mínimo posible para mantener el estado de resistencia nula. No obstante, su naturaleza cuantizada los hace atractivos como posibles portadores de información, pudiendo transportar ésta si su movimiento se lleva a cabo de forma controlada.

Este movimiento controlado se puede estudiar haciendo uso de la llamada *geometría no local*. En esta configuración, siendo un dispositivo superconductor en el estado mixto la muestra a estudio, se inyecta una corriente en una región determinada del mismo para inducir el movimiento de los vórtices, y se mide el voltaje generado por éstos cuando se mueven en otra región distinta (donde la corriente no fluye). Cualquier resistencia que se mida será por tanto únicamente causada por el movimiento de vórtices y no por la corriente inyectada.

En paralelo, recientemente se han publicado trabajos sobre la detección experimental de *efecto de campo* en nanoestructuras superconductoras, consistente en una modulación de la corriente crítica de un nanohilo superconductor mediante la aplicación de un campo eléctrico intenso o *voltaje de puerta*. La alta densidad de portadores de carga de los materiales metálicos hace que este efecto carezca de relevancia, ya que éstos apantallan rápidamente el campo eléctrico externo, pero su aplicación a materiales superconductores, donde se altera localmente el estado de mínima energía, es actualmente un campo poco explorado y sin una justificación teórica completa.

En esta tesis se estudian tanto las posibilidades y variaciones de la técnica de crecimiento por FIBID, como los distintos fenómenos relacionados con la naturaleza superconductora de los materiales que se obtienen.

A.2 Nanoestructuras superconductoras de W-C crecidas por Ga$^+$ FIBID

A.2.1 Transporte no local de vórtices

En relación a la línea de transporte no local y continuando con las ideas inicialmente propuestas por Grigorieva *et al.* [44] y posteriormente investigadas por Córdoba *et al.* [42, 68, 76], se han realizado experimentos y análisis en nanohilos estrechos (50 nm) y largos (10 μm). Mediante medidas de magneto-resistencia en modo no local, se han detectado resistencias equivalentes de hasta 8 Ω, causadas únicamente por el movimiento de vórtices a lo largo del canal superconductor. La distancia total recorrida, de 10 μm, es la mayor reportada hasta la fecha para el transporte de vórtices en esta configuración.

Los resultados refuerzan la hipótesis de que en nanoestructuras estrechas, la aparición de barreras de potencial en los bordes del nanohilo confina los vórtices en su interior, impidiendo desplazamientos laterales y haciendo por tanto la transferencia de presión más efectiva. Además, se han realizado simulaciones numéricas basadas en la teoría de Ginzburg-Landau que muestran adicionalmente el movimiento de una única fila de vórtices a lo largo del canal.

Estos resultados indican la posible aplicabilidad de los vórtices superconductores y las nanoestructuras en geometría no local a la transmisión de información cuantizada en nanocircuitos superconductores.

A.2.2 Imagen de la red de vórtices por microscopía de efecto túnel

Se han realizado, en colaboración con A. Domínguez y D. Serrate, del grupo de Nanofabricación y Microscopías Avanzadas de la Universidad de Zaragoza, varios experimentos preliminares para el estudio de películas delgadas de W-C crecidas por Ga^+ FIBID haciendo uso de técnicas de microscopía de efecto túnel.

Para ello, se ha diseñado y realizado un protocolo para la fabricación de sustratos apropiados para el microscopio STM, y se han optimizado los parámetros de crecimiento para la obtención de láminas delgadas de tamaño apropiado. Utilizando *espectroscopía de túnel de barrido* (STS), se han conseguido extraer imágenes de la red de vórtices, comparables a las ya publicadas por Guillamón *et al.* [58, 59, 73, 75, 81]. Asimismo, se han tomado medidas sobre su densidad de estados, mostrando la banda prohibida superconductora. Los resultados son comparables a los anteriormente mencionados y ponen de manifiesto la aplicabilidad y conveniencia de aunar estas dos técnicas, pudiendo realizar estudios avanzados sobre el material en el futuro.

En particular, posibles perspectivas de trabajo incluyen el estudio de perturbaciones locales encima de las láminas superconductoras mediante el posicionamiento por STM de espines magnéticos (átomos de Cr o Co [122]). La interacción entre dichos espines con el condensado superconductor da lugar a la aparición de fenómenos físicos de interés, como los estados ligados de *Yu-Shiba-Rusinov* [83], o el *efecto Bitter* [82, 121] a escala molecular.

A.2.3 Efecto de campo

La reciente publicación de los trabajos de Paolucci *et al.* [84] acerca del *efecto de campo* en nanoestructuras superconductoras es un punto de partida muy prometedor para el estudio de la nanofabricación de transistores basados en materiales superconductores. Estos trabajos muestran que es posible inducir una modulación de la corriente crítica mediante la aplicación de un voltaje de puerta, teniendo evidencias experimentales en ello para nanodispositivos de titanio [49, 51, 52], aluminio [89], vanadio [90], y niobio [91].

En este trabajo se ha abordado la fabricación y estudio de dispositivos superconductores de efecto de campo (S-FET) basados en W-C crecido por FIBID por primera vez, usando electrodos de puerta previamente depositados mediante litografía electrónica. Los resultados experimentales indican la existencia de un efecto de campo dentro de un rango de voltaje de hasta 3 V, dentro del cual el valor de la corriente crítica disminuye progresivamente con valores crecientes de voltaje de puerta. Estos resultados son comparables a los reportados para otros materiales, con un valor de temperatura crítica relativamente alto (el del W-C crecido por FIBID), y consiguiéndose una supresión total de la corriente crítica para un valor de voltaje de puerta relativamente bajo.

El rendimiento del dispositivo es comparable al de otros diseños similares propuestos en la literatura con otros materiales, siendo su método de crecimiento notablemente diferente. La flexibilidad que presenta la técnica de crecimiento por FIBID hace de estos experimentos un punto de partida sólido para la realización de estudios avanzados y el diseño de nuevos dispositivos S-FET basados en este material.

A.3 Nanoestructuras de W-C crecidas por Ga$^+$ Cryo-FIBID

La técnica de crecimiento por *Cryo-FIBID* es una variación del proceso inducido por FIB convencional, cuya principal diferencia reside en la temperatura de trabajo. Mientras que en el FIBID convencional el crecimiento tiene lugar a temperatura ambiente, el pilar fundamental de la Cryo-FIBID es la utilización de una temperatura de trabajo por debajo de la temperatura de condensación del material precursor que vaya a utilizarse.

La motivación para trabajar a esta (baja) temperatura es que si el sustrato se encuentra por debajo de dicho valor de condensación, en lugar de formarse una monocapa molecular de material precursor cuando éste llega a la superficie del sustrato, las moléculas de precursor pasan a la fase condensada al alcanzar el sustrato frío y constituyen una capa de espesor mucho mayor. Esto se traduce en una cantidad muy superior de precursor disponible para el FIB, lo cual resulta en el requerimiento de dosis iónicas muy inferiores para depositar la misma cantidad de precursor. A efectos prácticos, ello implica una velocidad de crecimiento enormemente superior a la del FIBID a temperatura ambiente, con hasta tres órdenes de magnitud de diferencia.

Esta técnica fue desarrollada y patentada por De Teresa *et al.* en 2018 [100]. El trabajo aquí presentado consiste en estudios posteriores acerca de la influencia de determinados parámetros del crecimiento en el crecimiento de nanoestructuras de W-C, así como en el estudio de sus propiedades eléctricas a baja temperatura, y en su aplicabilidad como contactos eléctricos para la caracterización de otras nanoestructuras. Se han observado efectos de redepósito lateral inducido por distribuciones de la dosis que no ocurren a temperatura ambiente, así como modulaciones del espesor de los depósitos dependiendo de la temperatura del reservorio de material precursor.

Los depósitos de W-C crecidos por Ga^+ Cryo-FIBID presentan comportamiento metálico a temperatura ambiente, aunque una resistividad mucho mayor que los crecidos por Ga^+ FIBID. Además, a diferencia de éstos, no presentan superconductividad en el rango estudiado, hasta 0.5 K. En cualquier caso, su respuesta óhmica los capacita para ser utilizados como contactos auxiliares en la caracterización de otras muestras, lo cual ha sido experimentalmente demostrado en la caracterización de un nanohilo de platino.

Este importante incremento en la velocidad de procesado hace de la Cryo-FIBID una técnica especialmente atractiva, lo cual, junto con su reciente desarrollo, harán de la misma un foco de interés en las investigaciones futuras.

A.4 Nanoestructuras superconductoras de W-C crecidas por He^+ FIBID

Aunque el crecimiento mediante Ga^+ FIBID es sin duda la variante más extendida y utilizada de esta técnica, es posible obtener mayor resolución lateral y reducir la magnitud del daño colateral inducido por el FIB de Ga^+ (tal como amorfización del sustrato e implantación iónica) si, en lugar de utilizar estos iones, se utiliza un FIB basado en iones de helio.

En el momento de escritura de esta tesis, existen artículos científicos publicados que referencian el crecimiento de estructuras tridimensionales de W-C mediante He^+ FIBID, pero apenas existen referencias que muestren su utilización para el crecimiento de estructuras en el plano. Se ha realizado un estudio sistemático del crecimiento en colaboración con G. Hlawacek, del centro de investigación Helmholtz-Zentrum Dresden-Rossendorf, en Dresden (Alemania).

Se han obtenido nanohilos con anchos de línea de hasta 10 nm (virtualmente imposibles de alcanzar usando Ga^+ FIBID). A partir de 20 nm de ancho, los nanohilos presentan comportamiento superconductor por debajo de 2.5-4 K, siendo éste y el resto de parámetros superconductores comparables a los obtenidos en nanoestructuras obtenidas por Ga^+ FIBID. Asimismo, se ha llevado a cabo un estudio de la composición y microestructura de las muestras, que indica un contenido metálico inferior a las obtenidas por Ga^+ FIBID.

También se ha estudiado el movimiento no local de vórtices en este material por primera vez, detectando transporte en distancias de hastas 3 μm. Todo ello asienta el crecimiento de W-C por He^+ FIBID como una herramienta más para la nanofabricación de este material, particularmente útil cuando se requieran dimensiones críticas que el crecimiento por Ga^+ no puede proveer.

A.5 Publicaciones

Los siguientes trabajos se han publicado durante el desarrollo de esta tesis:

- Rosa Córdoba, Pablo Orús, Željko L. Jelić, Javier Sesé, Manuel R. Ibarra, Isabel Guillamón, Sebastián Vieira, Juan José Palacios, Hermann Suderow, Milorad V. Milosević y José María De Teresa. "Long-range vortex transfer in superconducting nanowires". *Scientific reports* 9.12386 (2019). DOI: `10.1038/s41598-019-48887-7`.
- Rosa Córdoba, Pablo Orús, Stefan Strohauer, Teobaldo E. Torres y José María De Teresa. "Ultra-fast direct growth of metallic micro- and nano-structures by focused ion beam irradiation". *Scientific reports* 9.14076 (2019). DOI: `10.1038/s41598-019-50411-w`.
- José María De Teresa, Pablo Orús, Rosa Córdoba y Patrick Philipp. "Comparison between Focused Electron/Ion Beam-Induced Deposition of Room Temperature and under Cryogenic Conditions". *Micromachines* 10.12 (2019), p. 799. DOI: `10.3390/mi10120799`.
- Pablo Orús, Rosa Córdoba, Gregor Hlawacek y José María De Teresa. "Superconducting properties of in-plane W-C nanowires grown by He^+ Focused Ion Beam Induced Deposition". *Nanotechnology* 32.8 (2020). DOI: `10.1088/1361-6528/abc91c`.
- Pablo Orús, Rosa Córdoba y José María De Teresa. "Focused Ion Beam Induced Processing", en *Nanolithography techniques and their applications*, ed. José María De Teresa. Bristol: Institute of Physics (IOP), 2020. ISBN: 978-0-7503-2606-3. DOI:`10.1088/978-0-7503-2608-7`.

Se prevé, en un futuro próximo, abordar la publicación de otros dos trabajos, centrados respectivamente en el efecto de campo detectado en el estado superconductor de nanohilos de W-C depositados por Ga^+ FIBID, y en el efecto de proximidad y la resolución lateral observados en estructuras de W-C crecidas mediante Cryo-FIBID.

Bibliography

[1] Michael F. Crommie, Christopher P. Lutz, and Donald M. Eigler. "Confinement of electrons to quantum corrals on a metal surface". In: *Science* 262.5131 (1993), pp. 218–220. DOI: `10.1126/science.262.5131.218`.

[2] John Melngailis. "Focused ion beam technology and applications". In: *Journal of Vacuum Science & Technology B: Microelectronics Processing and Phenomena* 5.2 (1987), pp. 469–495. DOI: `10.1116/1.583937`.

[3] Steve Reyntjens and Robert Puers. "A review of focused ion beam applications in microsystem technology". In: *Journal of micromechanics and microengineering* 11.4 (2001), p. 287. DOI: `10.1088/0960-1317/11/4/301`.

[4] Lucille A. Giannuzzi et al. *Introduction to focused ion beams: instrumentation, theory, techniques and practice*. Springer Science & Business Media, 2004. DOI: `10.1007/b101190`.

[5] Cynthia A. Volkert and Andrew M. Minor. "Focused ion beam microscopy and micromachining". In: *MRS bulletin* 32.5 (2007), pp. 389–399. DOI: `10.1557/mrs2007.62`.

[6] Ivo Utke, Patrick Hoffmann, and John Melngailis. "Gas-assisted focused electron beam and ion beam processing and fabrication". In: *Journal of Vacuum Science & Technology B: Microelectronics and Nanometer Structures Processing, Measurement, and Phenomena* 26.4 (2008), pp. 1197–1276. DOI: `10.1116/1.2955728`.

[7] Jacques Gierak. "Focused ion beam technology and ultimate applications". In: *Semiconductor science and technology* 24.4 (2009), p. 043001. DOI: `10.1088/0268-1242/24/4/043001`.

[8] Ivo Utke, Stanislav Moshkalev, and Phillip Russell. *Nanofabrication using focused ion and electron beams: principles and applications*. Oxford University Press, 2012. ISBN: 9780199734214 0199734216.

[9] Zhiming M. Wang. *FIB nanostructures*. Springer, 2013. ISBN: 978-3-319-02874-3.

[10] Charlie Kong, Soshan Cheong, and Richard D. Tilley. “Recent Development in Focused Ion Beam Nanofabrication”. In: *Reference Module in Materials Science and Materials Engineering* (2019). DOI: 10.1016/B978-0-12-803581-8.10432-1.

[11] William Gilbert. *De magnete, magneticisque corporibus, et de magno magnete tellure*. Petrvs Short, 1956.

[12] Geoffrey I. Taylor. “Disintegration of water drops in an electric field”. In: *Proceedings of the Royal Society of London. Series A. Mathematical and Physical Sciences* 280.1382 (1964), pp. 383–397. DOI: 10.1098/rspa.1964.0151.

[13] Robert L. Seliger and Wayne P. Fleming. “Focused ion beams in microfabrication”. In: *Journal of Applied Physics* 45.3 (1974), pp. 1416–1422. DOI: 10.1063/1.1663422.

[14] Jonathan H. Orloff and Lynwood W. Swanson. “Study of a field-ionization source for microprobe applications”. In: *Journal of vacuum science and technology* 12.6 (1975), pp. 1209–1213. DOI: 10.1116/1.568497.

[15] Jonathan H. Orloff and Lynwood W. Swanson. “Fine-focus ion beams with field ionization”. In: *Journal of Vacuum Science and Technology* 15.3 (1978), pp. 845–848. DOI: doi.org/10.1116/1.569610.

[16] Victor E. Krohn and George R. Ringo. “Ion source of high brightness using liquid metal”. In: *Applied Physics Letters* 27.9 (1975), pp. 479–481. DOI: 10.1063/1.88540.

[17] Robert L. Seliger et al. “A high-intensity scanning ion probe with submicrometer spot size”. In: *Applied Physics Letters* 34.5 (1979), pp. 310–312. DOI: 10.1063/1.90786.

[18] Erwin W. Müller. “Das feldionenmikroskop”. In: *Zeitschrift für Physik* 131.1 (1951), pp. 136–142. DOI: 10.1007/BF01329651.

[19] Bill W. Ward, John A. Notte, and Nicholas P. Economou. “Helium ion microscope: A new tool for nanoscale microscopy and metrology”. In: *Journal of Vacuum Science & Technology B: Microelectronics and Nanometer Structures Processing, Measurement, and Phenomena* 24.6 (2006), pp. 2871–2874. DOI: 10.1116/1.2357967.

[20] Jacques Gierak. “Focused Ion Beam nano-patterning from traditional applications to single ion implantation perspectives”. In: *Nanofabrication* 1 (2014). DOI: 10.2478/nanofab-2014-0004.

[21] Nicholas P. Economou, John A. Notte, and William B. Thompson. “The history and development of the helium ion microscope”. In: *Scanning* 34.2 (2012), pp. 83–89. DOI: 10.1002/sca.20239.

[22] Gregor Hlawacek and Armin Gölzhäuser. *Helium Ion Microscopy*. Springer, 2016. DOI: 10.1007/978-3-319-41990-9.

[23] James F. Ziegler and Jochen P. Biersack. “The stopping and range of ions in matter”. In: *Treatise on heavy-ion science*. Springer, 1985, pp. 93–129. DOI: 10.1007/978-1-4615-8103-1_3.

[24] Steven A. Schwarz. “Secondary Ion Mass Spectroscopy”. In: *Encyclopedia of Materials: Science and Technology*. Oxford: Elsevier, 2001, pp. 8263–8290. DOI: `10.1016/B0-08-043152-6/01482-0`.

[25] Michael Tinkham. *Introduction to superconductivity*. Courier Corporation, 2004. ISBN: 0486134725, 9780486134727.

[26] Heike Kamerlingh Onnes. “The resistance of pure mercury at helium temperatures”. In: *Commun. Phys. Lab. Univ. Leiden, b* 120 (1911). DOI: `10.1007/978-94-009-2079-8_15`.

[27] Andreas Schilling et al. “Superconductivity above 130 K in the Hg–Ba–Ca–Cu–O system”. In: *Nature* 363.6424 (1993), pp. 56–58. DOI: `10.1038/363056a0`.

[28] Elliot Snider et al. “Room-temperature superconductivity in a carbonaceous sulfur hydride”. In: *Nature* 586.7829 (2020), pp. 373–377. DOI: `10.1038/s41586-020-2801-z`.

[29] Walter Meissner and Robert Ochsenfeld. “Ein neuer effekt bei eintritt der supraleitfähigkeit”. In: *Naturwissenschaften* 21.44 (1933), pp. 787–788. DOI: `10.1007/BF01504252`.

[30] Fritz London and Heinz London. “The electromagnetic equations of the supraconductor”. In: *Proceedings of the Royal Society of London. Series A-Mathematical and Physical Sciences* 149.866 (1935), pp. 71–88. DOI: `10.1098/rspa.1935.0048`.

[31] John Bardeen, Leon N. Cooper, and John R. Schrieffer. “Theory of superconductivity”. In: *Physical review* 108.5 (1957), p. 1175. DOI: `10.1103/PhysRev.108.1175`.

[32] Vitaly L. Ginzburg and Lev D. Landau. “On the theory of superconductivity”. In: *On Superconductivity and Superfluidity*. Springer, 2009, pp. 113–137. DOI: `10.1007/978-3-540-68008-6_4`.

[33] Jury N. Rjabinin and Lev W. Shubnikow. “Magnetic properties and critical currents of supra-conducting alloys”. In: *Nature* 135.3415 (1935), pp. 581–582. DOI: `10.1038/135581a0`.

[34] Alexei A. Abrikosov. “On the magnetic properties of superconductors of the second group”. In: *Sov. Phys. JETP* 5 (1957), pp. 1174–1182.

[35] Alexei A. Abrikosov. “Nobel Lecture: Type-II superconductors and the vortex lattice”. In: *Reviews of modern physics* 76.3 (2004), p. 975. DOI: `10.1103/RevModPhys.76.975`.

[36] Daniel Cribier et al. “Mise en evidence par diffraction de neutrons d’une structure periodique du champ magnetique dans le niobium supraconducteur”. In: *PhL* 9.2 (1964), pp. 106–107. DOI: `10.1016/0031-9163(64)90096-4`.

[37] Uwe Essmann and Hermann Träuble. “The direct observation of individual flux lines in type II superconductors”. In: *Physics letters A* 24.10 (1967), pp. 526–527. DOI: `10.1016/0375-9601(67)90819-5`.

[38] Rudolf P. Huebener. "The Abrikosov Vortex Lattice: Its Discovery and Impact". In: *Journal of Superconductivity and Novel Magnetism* 32.3 (2019), pp. 475–481. DOI: 10.1007/s10948-018-4916-0.

[39] Peter H. Kes and Chang C. Tsuei. "Two-dimensional collective flux pinning, defects, and structural relaxation in amorphous superconducting films". In: *Physical Review B* 28.9 (1983), p. 5126. DOI: 10.1103/PhysRevB.28.5126.

[40] Rudolf P. Huebener. *Magnetic flux structures in superconductors: extended reprint of a classic text*. Vol. 6. Springer Science & Business Media, 2001. DOI: 10.1007/978-3-662-08446-5.

[41] Florian Otto. "Nonlinear vortex transport in mesoscopic channels of amorphous NbGe". PhD thesis. Universität Regensburg, 2008.

[42] Rosa Córdoba. *Functional Nanostructures fabricated by focused electron/ion beam induced deposition*. Springer Science & Business Media, 2013. DOI: 10.1007/978-3-319-02081-5.

[43] Ivar Giaever. "Magnetic coupling between two adjacent type-II superconductors". In: *Physical Review Letters* 15.21 (1965), p. 825. DOI: 10.1103/PhysRevLett.15.825.

[44] Irina V. Grigorieva et al. "Long-range nonlocal flow of vortices in narrow superconducting channels". In: *Physical review letters* 92.23 (2004), p. 237001. DOI: 10.1103/PhysRevLett.92.237001.

[45] Andreas Helzel et al. "Nonlocal vortex motion in mesoscopic amorphous $Nb_{0.7}Ge_{0.3}$ structures". In: *Physical Review B* 74.22 (2006), p. 220510. DOI: 10.1103/PhysRevB.74.220510.

[46] Cheol H. Ahn, Jean Marc Triscone, and Jochen Mannhart. "Electric field effect in correlated oxide systems". In: *Nature* 424.6952 (2003), pp. 1015–1018. DOI: 10.1038/nature01878.

[47] Jun-Ichi Nishizawa. "Junction field-effect devices". In: *Semiconductor Devices for Power Conditioning*. Springer, 1982, pp. 241–272. DOI: 10.1007/978-1-4684-7263-9_11.

[48] Giovanni A. Ummarino et al. "Proximity Eliashberg theory of electrostatic field-effect doping in superconducting films". In: *Physical Review B* 96.6 (2017), p. 064509. DOI: 10.1103/PhysRevB.96.064509.

[49] Federico Paolucci et al. "Ultra-efficient superconducting Dayem bridge field-effect transistor". In: *Nano Letters* 18.7 (2018), pp. 4195–4199. DOI: 10.1021/acs.nanolett.8b01010.

[50] Pauli Virtanen, Alessandro Braggio, and Francesco Giazotto. "Superconducting size effect in thin films under electric field: Mean-field self-consistent model". In: *Physical Review B* 100.22 (2019), p. 224506. DOI: 10.1103/PhysRevB.100.224506.

[51] Federico Paolucci et al. "Magnetotransport Experiments on Fully Metallic Superconducting Dayem-Bridge Field-Effect Transistors". In: *Physical Review Applied* 11.2 (2019), p. 024061. DOI: 10.1103/PhysRevApplied.11.024061.

[52] Federico Paolucci et al. “Field-Effect Controllable Metallic Josephson Interferometer”. In: *Nano Letters* 19.9 (2019), pp. 6263–6269. DOI: 10.1021/acs.nanolett.9b02369.

[53] Pablo Orús, Rosa Córdoba, and José María De Teresa. “Focused Ion Beam Induced Processing”. In: *Nanolithography techniques and their applications*. Ed. by José María De Teresa. Bristol, U.K.: Institute of Physics (IOP), 2020. ISBN: 978-0-7503-2606-3. DOI: 10.1088/978-0-7503-2608-7.

[54] Nabil Bassim, Keana Scott, and Lucille A. Giannuzzi. “Recent advances in focused ion beam technology and applications”. In: *Mrs Bulletin* 39.4 (2014), pp. 317–325. DOI: 10.1557/mrs.2014.52.

[55] Gregor Hlawacek et al. “Helium ion microscopy”. In: *Journal of Vacuum Science & Technology B, Nanotechnology and Microelectronics: Materials, Processing, Measurement, and Phenomena* 32.2 (2014), p. 020801. DOI: 10.1116/1.4863676.

[56] Rosa Córdoba et al. “Ultra-fast direct growth of metallic micro- and nano-structures by focused ion beam irradiation”. In: *Scientific reports* 9.14076 (2019). DOI: 10.1038/s41598-019-50411-w.

[57] Jochen P. Biersack and Leroy G. Haggmark. “A Monte Carlo computer program for the transport of energetic ions in amorphous targets”. In: *Nuclear instruments and methods* 174.1-2 (1980), pp. 257–269. DOI: 10.1016/0029-554X(80)90440-1.

[58] Isabel Guillamón et al. “Direct observation of melting in a two-dimensional superconducting vortex lattice”. In: *Nature Physics* 5.9 (2009), pp. 651–655. DOI: 10.1038/nphys1368.

[59] Isabel Guillamón et al. “Direct observation of stress accumulation and relaxation in small bundles of superconducting vortices in tungsten thin films”. In: *Physical review letters* 106.7 (2011), p. 077001. DOI: 10.1103/PhysRevLett.106.077001.

[60] Hermann Suderow et al. “Imaging superconducting vortex cores and lattices with a scanning tunneling microscope”. In: *Superconductor Science and Technology* 27.6 (2014), p. 063001. DOI: 10.1088/0953-2048/27/6/063001.

[61] Langlong Zhang et al. “A compact sub-Kelvin ultrahigh vacuum scanning tunneling microscope with high energy resolution and high stability”. In: *Review of Scientific Instruments* 82.10 (2011), p. 103702. DOI: 10.1063/1.3646468.

[62] El Hadi S. Sadki, Shuuichi Ooi, and Kazuto Hirata. “Focused-ion-beam-induced deposition of superconducting nanowires”. In: *Applied Physics Letters* 85.25 (2004), pp. 6206–6208. DOI: 10.1063/1.1842367.

[63] El Hadi S. Sadki, Shuuichi Ooi, and Kazuto Hirata. “Focused ion beam induced deposition of superconducting thin films”. In: *Physica C: Superconductivity and its applications* 426 (2005), pp. 1547–1551. DOI: 10.1016/j.physc.2005.02.151.

[64] Isaac J. Luxmoore et al. “Low temperature electrical characterisation of tungsten nano-wires fabricated by electron and ion beam induced chemical

vapour deposition". In: *Thin Solid Films* 515.17 (2007), pp. 6791–6797. DOI: 10.1016/j.tsf.2007.02.029.

[65] Detlef Spoddig et al. "Transport properties and growth parameters of PdC and WC nanowires prepared in a dual-beam microscope". In: *Nanotechnology* 18.49 (2007), p. 495202. DOI: 10.1088/0957-4484/18/49/495202.

[66] Wuxia Li, Jon C. Fenton, and Paul A. Warburton. "Focused-ion-beam direct-writing of ultra-thin superconducting tungsten composite films". In: *IEEE transactions on applied superconductivity* 19.3 (2009), pp. 2819–2822. DOI: 10.1109/TASC.2009.2019251.

[67] Wuxia Li et al. "Superconductivity of ultra-fine tungsten nanowires grown by focused-ion-beam direct-writing". In: *Microelectronic engineering* 88.8 (2011), pp. 2636–2638. DOI: 10.1016/j.mee.2010.12.116.

[68] Rosa Córdoba et al. "Magnetic field-induced dissipation-free state in superconducting nanostructures". In: *Nature communications* 4.1437 (2013). DOI: 10.1038/ncomms2437.

[69] Rosa Córdoba et al. "Suspended tungsten-based nanowires with enhanced mechanical properties grown by focused ion beam induced deposition". In: *Nanotechnology* 28.44 (2017), p. 445301. DOI: 10.1088/1361-6528/aa873c.

[70] Wuxia Li et al. "Tunability of the superconductivity of tungsten films grown by focused-ion-beam direct writing". In: *Journal of Applied Physics* 104.9 (2008), p. 093913. DOI: 10.1063/1.3013444.

[71] Jun Dai et al. "Superconductivity in tungsten-carbide nanowires deposited from the mixtures of $W(CO)_6$ and $C_{14}H_{10}$". In: *Japanese Journal of Applied Physics* 52.7R (2013), p. 075001. DOI: 10.7567/JJAP.52.075001.

[72] Yi Sun et al. "Voltage-current properties of superconducting amorphous tungsten nanostrips". In: *Scientific reports* 3 (2013), p. 2307. DOI: 10.1038/srep02307.

[73] Isabel Guillamón et al. "Nanoscale superconducting properties of amorphous W-based deposits grown with a focused-ion-beam". In: *New Journal of Physics* 10.9 (2008), p. 093005. DOI: 10.1088/1367-2630/10/9/093005.

[74] Rosa Córdoba et al. "Vertical growth of superconducting crystalline hollow nanowires by He+ focused ion beam induced deposition". In: *Nano Letters* 18.2 (2018), pp. 1379–1386. DOI: 10.1021/acs.nanolett.7b05103.

[75] Isabel Guillamón et al. "Nanostructuring superconducting vortex matter with focused ion beams". In: *Physica C: Superconductivity and its Applications* 503 (2014), pp. 70–74. DOI: 10.1016/j.physc.2014.04.031.

[76] Rosa Córdoba et al. "Long-range vortex transfer in superconducting nanowires". In: *Scientific reports* 9.12386 (2019). DOI: 10.1038/s41598-019-48887-7.

[77] Goran Karapetrov et al. "Evidence of vortex jamming in Abrikosov vortex flux flow regime". In: *Physical Review B* 86.5 (2012), p. 054524. DOI: 10.1103/PhysRevB.86.054524.

[78] Tyler Morgan-Wall et al. “Measurement of critical currents of superconducting aluminum nanowires in external magnetic fields: evidence for a Weber blockade”. In: *Physical Review Letters* 114.7 (2015), p. 077002. DOI: 10.1103/PhysRevLett.114.077002.

[79] Lorenz Kramer and Richard J. Watts-Tobin. “Theory of dissipative current-carrying states in superconducting filaments”. In: *Physical Review Letters* 40.15 (1978), p. 1041. DOI: 10.1103/PhysRevLett.40.1041.

[80] Richard J. Watts-Tobin, Yves Krähenbühl, and Lorenz Kramer. “Nonequilibrium theory of dirty, current-carrying superconductors: Phase-slip oscillators in narrow filaments near T_c”. In: *Journal of Low Temperature Physics* 42.5 (1981), pp. 459–501. DOI: 10.1007/BF00117427.

[81] Isabel Guillamón et al. “Enhancement of long-range correlations in a 2D vortex lattice by an incommensurate 1D disorder potential”. In: *Nature Physics* 10.11 (2014), pp. 851–856. DOI: 10.1038/nphys3132.

[82] Simon J. Bending. “Local magnetic probes of superconductors”. In: *Advances in Physics* 48.4 (1999), pp. 449–535. DOI: 10.1080/000187399243437.

[83] Alexander V. Balatsky, Ilya Vekhter, and Jian-Xin Zhu. “Impurity-induced states in conventional and unconventional superconductors”. In: *Reviews of Modern Physics* 78.2 (2006), p. 373. DOI: 10.1103/RevModPhys.78.373.

[84] Federico Paolucci et al. “Field-effect control of metallic superconducting systems”. In: *AVS Quantum Science* 1.1 (2019), p. 016501. DOI: 10.1116/1.5129364.

[85] Giorgio De Simoni et al. “Metallic supercurrent field-effect transistor”. In: *Nature nanotechnology* 13.9 (2018), pp. 802–805. DOI: 10.1038/s41565-018-0190-3.

[86] Yong-Joo Doh et al. “Tunable supercurrent through semiconductor nanowires”. In: *Science* 309.5732 (2005), pp. 272–275. DOI: 10.1126/science.1113523.

[87] Francesco Giazotto et al. “Ultrasensitive proximity Josephson sensor with kinetic inductance readout”. In: *Applied Physics Letters* 92.16 (2008), p. 162507. DOI: 10.1063/1.2908922.

[88] Anthony J. Annunziata et al. “Tunable superconducting nanoinductors”. In: *Nanotechnology* 21.44 (2010), p. 445202. DOI: 10.1088/0957-4484/21/44/445202.

[89] Lennart Bours et al. “Unveiling mechanisms of electric field effects on superconductors by a magnetic field response”. In: *Phys. Rev. Research* 2 (3 2020), p. 033353. DOI: 10.1103/PhysRevResearch.2.033353.

[90] Claudio Puglia et al. “Vanadium gate-controlled Josephson half-wave nanorectifier”. In: *Applied Physics Letters* 116.25 (2020), p. 252601. DOI: 10.1063/5.0013512.

[91] Giorgio De Simoni, Claudio Puglia, and Francesco Giazotto. “Niobium Dayem nano-bridge Josephson gate-controlled transistors”. In: *Applied Physics Letters* 116.24 (2020), p. 242601. DOI: 10.1063/5.0011304.

[92] Guillaume Desbois et al. "Cryogenic vitrification and 3D serial sectioning using high resolution cryo-FIB SEM technology for brine-filled grain boundaries in halite: first results". In: *Geofluids* 8.1 (2008), pp. 60–72. DOI: `10.1111/j.1468-8123.2007.00205.x`.

[93] Christopher D.J. Parmenter et al. "Making the practically impossible "Merely difficult"—Cryogenic FIB lift-out for "Damage free" soft matter imaging". In: *Microscopy research and technique* 79.4 (2016), pp. 298–303. DOI: `10.1002/jemt.22630`.

[94] William Tiddi et al. "Organic ice resists". In: *Nano letters* 17.12 (2017), pp. 7886–7891. DOI: `10.1021/acs.nanolett.7b04190`.

[95] Aiden A. Martin and Milos Toth. "Cryogenic electron beam induced chemical etching". In: *ACS applied materials & interfaces* 6.21 (2014), pp. 18457–18460. DOI: `10.1021/am506163w`.

[96] Herbert O. Funsten et al. "Low-temperature beam-induced deposition of thin tin films". In: *Journal of applied physics* 71.3 (1992), pp. 1475–1484. DOI: `10.1063/1.351241`.

[97] David A. Bell et al. "Electron beam-induced deposition of tungsten". In: *Journal of Vacuum Science & Technology B: Microelectronics and Nanometer Structures Processing, Measurement, and Phenomena* 12.5 (1994), pp. 2976–2979. DOI: `10.1116/1.587545`.

[98] Matthew Bresin et al. "Focused electron beam-induced deposition at cryogenic temperatures". In: *Journal of Materials Research* 26.3 (2011), p. 357. DOI: `10.1557/jmr.2010.59`.

[99] Matthew Bresin, Milos Toth, and Kathleen A. Dunn. "Direct-write 3D nanolithography at cryogenic temperatures". In: *Nanotechnology* 24.3 (2012), p. 035301. DOI: `10.1088/0957-4484/24/3/035301`.

[100] José María De Teresa et al. *Procedimiento para depositar elementos sobre un sustrato de interés y dispositivo*. Registration code P20183075; international extension code PCT/ES2019/070526, publication code WO2020021149. Priority date 25/07/2018, Spain. Reference: `ES1641.1387`.

[101] José María De Teresa et al. "Comparison between Focused Electron/Ion Beam-Induced Deposition at Room Temperature and under Cryogenic Conditions". In: *Micromachines* 10.12 (2019), p. 799. DOI: `10.3390/mi10120799`.

[102] Alba Salvador-Porroche et al. "Optimization of Pt-C Deposits by Cryo-FIBID: Substantial Growth Rate Increase and Quasi-Metallic Behaviour". In: *Nanomaterials* 10.10 (2020), p. 1906. DOI: `10.3390/nano10101906`.

[103] Daniel Berkoh and Sarang Kulkarni. "Challenges in Lift-Off Process Using CAMP Negative Photoresist in III–V IC Fabrication". In: *IEEE Transactions on Semiconductor Manufacturing* 32.4 (2019), pp. 513–517. DOI: `10.1109/TSM.2019.2944133`.

[104] Amalio Fernández-Pacheco et al. “Metal-insulator transition in Pt-C nanowires grown by focused-ion-beam-induced deposition”. In: *Physical Review B* 79.17 (2009), p. 174204. DOI: 10.1103/PhysRevB.79.174204.

[105] Rosa Córdoba et al. “Three-dimensional superconducting nanohelices grown by He+-focused-ion-beam direct writing”. In: *Nano letters* 19.12 (2019), pp. 8597–8604. DOI: 10.1021/acs.nanolett.9b03153.

[106] Julien Basset et al. “High kinetic inductance microwave resonators made by He-Beam assisted deposition of tungsten nanowires”. In: *Applied Physics Letters* 114.10 (2019), p. 102601. DOI: 10.1063/1.5080925.

[107] Gheorghe Stan, Stuart B. Field, and John M. Martinis. “Critical field for complete vortex expulsion from narrow superconducting strips”. In: *Physical review letters* 92.9 (2004), p. 097003. DOI: 10.1103/PhysRevLett.92.097003.

[108] Florian Otto et al. “Reversal of nonlocal vortex motion in the regime of strong nonequilibrium”. In: *Physical review letters* 104.2 (2010), p. 027005. DOI: 10.1103/PhysRevLett.104.027005.

[109] Florian Otto et al. “Nonlocal versus local vortex dynamics in the transversal flux transformer effect”. In: *Physical Review B* 81.17 (2010), p. 174521. DOI: 10.1103/PhysRevB.81.174521.

[110] Kazuyuki Kohama et al. “Tungsten-based pillar deposition by helium ion microscope and beam-induced substrate damage”. In: *Journal of Vacuum Science & Technology B, Nanotechnology and Microelectronics: Materials, Processing, Measurement, and Phenomena* 31.3 (2013), p. 031802. DOI: 10.1116/1.4800983.

[111] Ping Chen et al. “Nanopillar growth by focused helium ion-beam-induced deposition”. In: *Nanotechnology* 21.45 (2010), p. 455302. DOI: 10.1088/0957-4484/21/45/455302.

[112] Teresa Puig et al. “Stable vortex configurations in superconducting 2× 2 antidot clusters”. In: *Applied physics letters* 70.23 (1997), pp. 3155–3157. DOI: 10.1063/1.119118.

[113] Irinel Chiorescu et al. “Coherent quantum dynamics of a superconducting flux qubit”. In: *Science* 299.5614 (2003), pp. 1869–1871. DOI: 10.1126/science.1081045.

[114] Chandra M. Natarajan, Michael G. Tanner, and Robert H. Hadfield. “Superconducting nanowire single-photon detectors: physics and applications”. In: *Superconductor science and technology* 25.6 (2012), p. 063001. DOI: 10.1088/0953-2048/25/6/063001.

[115] Werner Bachtold. “The vortex file: a proposal for a new application of type-II superconductivity”. In: *IEEE Transactions on Magnetics* 15.1 (1979), pp. 558–561. DOI: 10.1109/TMAG.1979.1060127.

[116] Jürgen Parisi and Rudolf P. Huebener. “A superconducting vortex-memory system”. In: *IEEE Transactions on Electron Devices* 31.3 (1984), pp. 310–314. DOI: 10.1109/T-ED.1984.21521.

[117] Taras Golod, Adrian Iovan, and Vladimir M. Krasnov. “Single Abrikosov vortices as quantized information bits”. In: *Nature communications* 6.8628 (2015). DOI: `10.1038/ncomms9628`.

[118] Sergey Mironov et al. “Anomalous Josephson effect controlled by an Abrikosov vortex”. In: *Physical Review B* 96.21 (2017), p. 214515. DOI: `10.1103/PhysRevB.96.214515`.

[119] Deung-Jang Choi et al. “Mapping the orbital structure of impurity bound states in a superconductor”. In: *Nature communications* 8.15175 (2017). DOI: `10.1038/ncomms15175`.

[120] Deung-Jang Choi et al. “Influence of Magnetic Ordering between Cr Adatoms on the Yu-Shiba-Rusinov States of the β-Bi$_2$Pd Superconductor”. In: *Physical review letters* 120.16 (2018), p. 167001. DOI: `10.1103/PhysRevLett.120.167001`.

[121] Irina V. Grigorieva. “Magnetic flux decoration of type-II superconductors”. In: *Superconductor Science and Technology* 7.4 (1994), p. 161. DOI: `10.1088/0953-2048/7/4/001`.

[122] David Serrate et al. “Imaging and manipulating the spin direction of individual atoms”. In: *Nature Nanotechnology* 5.5 (2010), pp. 350–353. DOI: `10.1038/nnano.2010.64`.

List of Abbreviations

BCS	**B**ardeen-**C**ooper-**S**chrieffer
BSE	**B**ack**s**cattered **E**lectron
CASINO	Monte **Ca**rlo **Si**mulation of Electro**n** Trajectory in S**o**lids
CDEM	**C**hannel **D**etection **E**lectron **M**ultiplier
CPD	**C**ooper **P**air **D**ensity
EDS	**E**nergy **D**ispersive X-Ray **S**pectroscopy
ETD	**E**verhart-**T**hornley **D**etector
FEB	**F**ocused **E**lectron **B**eam
FIB	**F**ocused **I**on **B**eam
FIBID	**F**ocused **I**on **B**eam **I**nduced **D**eposition
GFIS	**G**as **F**ield **I**on **S**ource
GIS	**G**as **I**njection **S**ystem
HAADF	**H**igh **A**ngle **A**nnular **D**ark **F**ield
HIM	**H**elium **I**on **M**icroscopy
HRTEM	**H**igh **R**esolution **T**ransmission **E**lectron **M**icroscopy
LMIS	**L**iquid **M**etal **I**on **S**ource
PPMS	**P**hysical **P**roperty **M**easurement **S**ystem
SE	**S**econdary **E**lectron
SEM	**S**canning **E**lectron **M**icroscopy
SI	**S**econdary **I**on
SIMS	**S**econdary **I**on **M**ass **S**pectrometry
SRIM	**S**topping and **R**ange of **I**ons in **M**atter
STEM	**S**canning **T**ransmission **E**lectron **M**icroscopy
STM	**S**canning **T**unneling **M**icroscopy
STS	**S**canning **T**unneling **S**pectroscopy
S-FET	**S**uperconducting **F**ield **E**ffect **T**ransistor
SQUID	**S**uperconducting **Q**uantum **I**nterference **D**evice
TDGL	**T**ime-**D**ependent **G**inzburg **L**andau framework
TEM	**T**ransmission **E**lectron **M**icroscopy
TLD	**T**hrough-the-**L**ens **D**etector

List of Symbols

A	Deposit area
$a_\triangle$	Inter-vortex separation
B	Magnetic field
B_c	Critical magnetic field
B_{c1}	Lower critical magnetic field
B_{c2}	Upper critical magnetic field
b	Transverse lead width
D	Ion dose
D_0	Minimal dose for deposition
D_{max}	Maximum delivered dose
Δ	Superconducting energy gap
ΔT	Transition amplitude
Δx	Deposit lateral size
E	Electric field
e	Electron charge
ε_L	Vortex energy
F_L	Lorentz force
F_P	Pinning force
Φ	Flux quantum
φ	Superconducting phase
G	Conductance
g_m	Transconductance
h	Planck constant
$\hbar$	Reduced Planck constant
η	Vortex viscosity
I	Driving current
I_c	Critical current
I_c^0	Zero-temperature crit. curr.
I_t	Tunneling current
J	Current density
J_c	Critical current density
k_B	Boltzmann constant
κ	Ginzburg-Landau parameter
L	Deposit length
L_k	Kinetic inductance
λ	Penetration depth
λ_L	London penetration length
μ_0	Magnetic permeability
n_s	Density of sc. charge carriers
n_Φ	Vortex density
ξ	Coherence length
ψ	Order parameter
R	Resistance
R_N	Normal-state resistance
r	Position
ρ	Resistivity
T	Temperature
T_c	Critical temperature
T_p	Precursor temperature
t	Deposition time
V	Voltage
V_b	Bias voltage
V_g	Gate voltage
V_g^c	Critical gate voltage
v_D	Volume per dose
v_Φ	Vortex velocity
w	Deposit width
z	Deposit thickness